

**NANOELECTRONICS AND SPINTRONICS WITH DIRAC
MATERIALS: SPIN PROPERTIES OF GRAPHENE,
TOPOLOGICAL INSULATORS, AND WEYL SEMIMETALS**

by
ALI ASGHARPOUR

Submitted to the Graduate School of Engineering and Natural Sciences
in partial fulfillment of
the requirements for the degree of Doctor of Philosophy

Sabanci University
December 2020

**NANOELECTRONICS AND SPINTRONICS WITH DIRAC
MATERIALS: SPIN PROPERTIES OF GRAPHENE,
TOPOLOGICAL INSULATORS, AND WEYL SEMIMETALS**

Approved by:

[Redacted signature]

[Redacted signature]

[Redacted signature]

[Redacted signature]

[Redacted signature]

Date of Approval: December 22, 2020

ALI ASGHARPOUR 2020 ©

All Rights Reserved

ABSTRACT

NANOELECTRONICS AND SPINTRONICS WITH DIRAC MATERIALS: SPIN PROPERTIES OF GRAPHENE, TOPOLOGICAL INSULATORS, AND WEYL SEMIMETALS

ALI ASGHARPOUR

Physics Ph.D Dissertation, December 2020

Dissertation Supervisor: Prof. Dr. İnanç Adagideli

Keywords: Mesoscopic and nanoscale systems, Dirac materials, Graphene, Topological insulators, Weyl semimetals, Spintronics, Valleytronics, Spin-orbit coupling

Dirac materials are a class of condensed matter systems in which the relativistic Dirac equation describes the dynamics of charge carriers. In this thesis, we investigate various quantum transport phenomena in these exotic materials, particularly graphene, topological insulators, and Weyl semimetals, as well as propose spintronics and valleytronics applications. We also focus on spin-orbit coupling induced by adatoms on graphene, and we explore how valley and spin degrees of freedom interact with each other in the presence of deposited adatoms. We hence investigate methods to convert valley currents into extractable and measurable spin currents, which is pivotal in designing spin- and valleytronics devices. Furthermore, we study current-induced spin accumulation effect at the surfaces of three-dimensional topological insulators (3DTIs), and we show how to extract these spins into topologically trivial materials commonly used in electronic devices. We find that, unlike the corresponding conventional effect in two-dimensional electron gases, the mixing of the electron and hole degrees of freedom at the TI surface allows for additional methods of spin manipulation. In particular, we expose a way to use electrical gate potentials to locally manipulate spins in regions smaller than the spin precession length, the conventional length over which the spins can be manipulated. We devise a new scheme for spin manipulation based on the admixture of the electron and hole degrees of freedom at TI surfaces. Next, we study hyperfine interactions between nuclear spins and itinerant electrons at 3DTIs surfaces. We find that hyperfine inter-

actions induce elastic backscattering processes through spin-flip transitions between the surface states at each plane of a 3DTI in addition to forward scattering through intra-transitions within the surface states. Moreover, we find additional forward scattering processes for the edges of crystals that are not in the growth direction. Finally, we study Weyl heterostructures between opposing chiralities which can be obtained by shifting the nodes with specific chirality in opposing directions in momentum space. We find a new magnetoelectric effect in Weyl semimetal junctions, similar to the giant magnetoresistance effect in ferromagnets. We thus introduce a new chirality-valve device and investigate the robustness of this effect against the presence of nonmagnetic and magnetic impurities in junctions based on Weyl semimetals.

ÖZET

DIRAC MALZEMELERİ İLE NANOELEKTRONİK VE SPİNTRONİK: GRAFEN, TOPOLOJİK YALITKAN VE WEYL YARI METALLERİNİN ÖZELLİKLERİ

ALI ASGHARPOUR

Fizik Doktora Tezi, Aralık 2020

Tez Danışmanı: Prof. Dr. İnanç Adagideli

Anahtar Kelimeler: Mezoskopik ve nano ölçekli sistemler, Dirac malzemeleri, Grafen, Topolojik Yalıtkanlar, Weyl yarı metalleri, Spintronik, Vadiatronik, Spin-yörünge etkileşimi

Dirac malzemeleri, yük taşıyıcılarının dinamiklerinin göreceli Dirac denklemi tarafından tanımlandığı sistemlerden oluşan bir yoğun madde sınıfıdır. Bu tezde bu egzotik malzemelerde, özellikle grafen, topolojik yalıtkanlar ve Weyl yarı metallerinde görülen çeşitli kuantum taşınım olaylarını araştırıyor ve bu malzemeler için bazı spintronik ve vadiatronik uygulamaları öneriyoruz. Ayrıca grafen üzerinde adatomların neden olduğu spin-yörünge etkileşimine odaklanıyor ve vadi ve spin serbestlik derecelerinin birikmiş adatomlar varlığında birbirleriyle nasıl etkileştiğini araştırıyoruz. Bu nedenle, spin ve vadiatronik cihazlarının tasarımında çok önemli olan vadi akımlarını malzeme dışına çıkarılabilir ve ölçülebilir spin akımlarına dönüştürmek için yöntemler araştırıyoruz. Ayrıca, üç boyutlu topolojik yalıtkanların yüzeylerinde akım ile indüklenmiş spin akümüülasyonunu inceliyoruz ve bu spinleri elektronik cihazlarda yaygın olarak kullanılan sıradan (topolojik olmayan) malzemelere nasıl çıkaracağımızı gösteriyoruz. İki boyutlu elektron gazlarındaki geleneksel etkiden farklı olarak, elektron ve deşik serbestlik derecelerinin topolojik yalıtkan yüzeyinde karışmasının yeni spin kontrol etme yöntemlerine izin verdiğini buluyoruz. Özellikle, spinlerin kontrol edilebileceği konvansiyonel uzunluk olan spin-presesyon uzunluğundan daha küçük bölgelerde, spinleri yerel olarak elektronik kapı potansiyellerini ile kontrol etmenin bir yöntemini gösteriyoruz. Böylece, topolojik yalıtkan yüzeylerindeki elektron ve deşik serbestlik derecelerinin karışımına dayanan spin kontrolü için yeni bir şema tasarlıyoruz. Daha sonra nükleer spinler ve üç boyutlu topolojik

yalıtkan yüzeylerinde bulunan serbest elektronların arasındaki aşırı ince (hyperfine) etkileşimleri inceliyoruz. Aşırı ince etkileşimlerin, yüzey durumları içindeki geçişler boyunca ileri saçılmaya ek olarak, üç boyutlu topolojik yalıtkan yüzeyinin her bir yüzünün kuantum durumları arasında spin çevirme geçişleri yoluyla elastik geri saçılma sürecini indüklediğini buluyoruz. Ayrıca, kristallerin büyüme yönünde olmayan yüzlerinde bulunan kuantum durumları için ek bir ileri saçılma mekanizması buluyoruz. Son olarak, momentum uzayında Weyl noktalarının ters yönlerde kaydırılması suretiyle kiralite işareti değiştirilen melez Weyl yapılarını inceliyoruz. Weyl yarı metal bağlantı noktalarında, ferromıknatıslardaki dev manyetodirenç etkisine benzer şekilde yeni bir manyeto-elektrik etkisi buluyoruz. Böylelikle, yeni bir kiralite-valf aygıtı tasarlıyoruz ve Weyl yarı metallerine dayalı bu aygıtlarda manyetik ve manyetik olmayan safsızlıkların varlığına karşı bu etkinin sağlamlığını araştırıyoruz.

ACKNOWLEDGEMENTS

Foremost, I would like to convey my heartfelt gratitude to my advisor Prof. İnanç Adagideli for the continuous support of my Ph.D. study and related research, for his patience, motivation, and immense knowledge. It was a great privilege and honor for me to work and study under his supervision.

I sincerely appreciate Prof. Klaus Richter for being in my thesis committee and for his constructive and precious comments on my work. I am thankful to him and his group, particularly Dr. Cosimo Gorini, with whom I had fruitful collaboration.

My sincere gratitude to the thesis committee members, Prof. Zafer Gedik, Prof. Burç Mısırlıoğlu, and Prof. Seyed Akbar Jafari for their positive attitude and insightful comments which incited me to widen my research from various perspectives.

I owe many thanks to the "Science of Nature" team for giving me the opportunity to experience tremendous personal and professional growth regarding teaching skills. In particular, my most profound appreciation to Dr. Yuki Kaneko for her support, guidance, and mentoring. I am also grateful to Dr. Emine Süphan Bakkal with whom I had an excellent collaboration as instructors of the "Science of Nature" course.

Special thanks to my friend Dr. Vahid Sazgari with whom I had insightful discussions and collaborations. My thanks also go out to the support I received from my colleagues and collaborators, Dr. Barış Pekerten, Dr. Saber Rostamzadeh, and Ahmet Mert Bozkurt. Moreover, I have enjoyed the company of my friends in Sabancı University, far too numerous to be listed individually. They have shown me a life outside of physics and taught me ways to enjoy life.

I would like to declare my deep love for and indebtedness to my family, who have been supportive throughout my life, particularly during my graduate studies. My special thanks to Tina Nikazar for her support, patience, and understanding, as well as to my love Mocha.

I gratefully acknowledge financial support from Scientific and Technological Research Council of Turkey (TUBITAK) under Project Grant No. 114F163 and from Lockheed Martin Corporation Research Grant.

To my mother

TABLE OF CONTENTS

LIST OF FIGURES	xiii
LIST OF ABBREVIATIONS	xix
1. INTRODUCTION	1
2. OVERVIEW	5
2.1. Dirac Materials	6
2.1.1. Graphene.....	7
2.1.2. Topological insulators	8
2.1.3. Weyl semimetals	9
2.2. Applications of Dirac Materials.....	11
2.2.1. Graphene.....	12
2.2.2. Topological insulators	13
2.2.3. Weyl semimetals	14
3. ADATOMS IN GRAPHENE	16
3.1. Introduction	16
3.2. Quantum Spin Hall Effect	17
3.3. Adatoms Induced Spin-valley Coupling.....	21
3.3.1. Adatoms on different sublattices	26
3.4. Conclusion	29
4. GATE-CONTROLLED SPIN EXTRACTION FROM TOPOLOGICAL INSULATOR SURFACES	31
4.1. Introduction	31
4.2. A Spin-galvanic Paradox and its Solution	33
4.2.1. Setting the stage	33
4.2.2. Spin galvanic basics	35

4.2.3. Spin galvanic effect on the surface of a 3D topological insulator	35
4.3. Spin Extraction from 3D topological insulator Surfaces	36
4.3.1. Model and method	37
4.3.2. Spin dynamics and accumulation at the surface	39
4.3.3. Spin extraction	41
4.4. Conclusion	43
5. HYPERFINE INTERACTION FOR THREE-DIMENSIONAL TOPOLOGICAL INSULATORS IN THE BISMUTH-SELENIDE FAMILY	46
5.1. Introduction	46
5.2. Hyperfine Interactions	48
5.3. The Band Model of Bi-based Topological Insulators	49
5.4. Hyperfine Interactions within Bismuth-based Topological Insulator Band Model	50
5.4.1. The hyperfine interaction for p -like states	51
5.4.2. Taking into account s -like states' contributions to the band model	52
5.5. Hyperfine Interactions for Surface States	53
5.5.1. \hat{z} surface states	54
5.5.2. \hat{y} surface states	56
5.5.3. \hat{x} surface states	57
5.6. Conclusion	58
6. GIANT MAGNETORELECTRIC EFFECT IN WEYL SEMIMETALS	59
6.1. Introduction	59
6.2. Method and Model	60
6.3. Weyl Semimetal Junction, GMR Effect	63
6.3.1. Junctions with broken time-reversal symmetry	64
6.3.2. Junctions with broken inversion symmetry	68
6.3.3. Disordered systems	69
6.4. Conclusion	71
7. CONCLUSION	72
BIBLIOGRAPHY	74
APPENDIX A: Edelstein Effect in Two-dimensional Quantum Wires	93
A.1. Extraction of Current-induced Spins	94
A.2. Voltage Probe	94

APPENDIX B: Effective Surface Hamiltonians and Spin Operators	98
APPENDIX C: Mean Free Time Estimation	100
APPENDIX D: $\eta = 0$ case	102
APPENDIX E: Spin-charge Coupled Dynamics for Topological Insulator \hat{z} Surface	103
APPENDIX F: Crystal Structure and Atomic Orbitals	108
APPENDIX G: Further Details about Hyperfine Interactions Calculations	111
G.1. Linear Combination of Atomic Orbitals Method for Bi_2Se_3 Family Materials	111
G.2. Hyperfine Interaction Calculations via Linear Combination of Atomic Orbitals Method	112
APPENDIX H: Details on Hyperfine Interaction Coefficients	116

LIST OF FIGURES

Figure 3.1. Illustration of the graphene lattice (left) and the band structure (right). A and B denote different sublattices. \mathbf{a} and \mathbf{b} are two primitive vectors of the Bravais lattice.....	18
Figure 3.2. (a) Schematic of a zigzag nanoribbon graphene with $L = 40a$ and $W = 67\sqrt{3}a/6$, where a is the magnitude of the primitive vector along $\hat{\mathbf{x}}$ direction ($\mathbf{a} = a\hat{\mathbf{x}}$). (b) Band structure of a the system shown in panel (a) in quantum spin Hall phase. Parameters used are $\lambda_{SO} = 0.06t$ and $\lambda_R = \lambda_\nu = 0$	20
Figure 3.3. Energy bands for a zigzag strip shown in Fig. 3.2(b) in (a) the quantum spin Hall phase $\lambda_\nu = 0.15t$ and (b) the insulating phase $\lambda_\nu = 0.5t$. Parameters used are $\lambda_{SO} = 0.08t$, and $\lambda_R = 0.06t$. The edge states on a given edge cross at $ka = \pi$	20
Figure 3.4. (a) $\langle S_z \rangle$ denotes spin polarization in a zigzag nanoribbon graphene. (b) Charge current density and (c) z -component of the spin current density in a zigzag nanoribbon graphene. Parameters used are $L = 20a$, $W = 67\sqrt{3}a/6$, $\lambda_{SO} = 0.06t$, and $\lambda_R = \lambda_\nu = 0$	22
Figure 3.5. Spin and valley conductances in a clean zigzag nanoribbon graphene with $L = 20a$ and $W = 67\sqrt{3}a/6$	24
Figure 3.6. (a) Zigzag strip with an adatom impurity (green circle). (b) Spin conductance and (c) valley polarization of the system shown in panel (a). (d) The z -component of the spin conductance in addition to valley polarization for zigzag nanoribbon graphene with a Rashba impurity due to the presence of an adatom. Parameters used are $L = 20a$, $W = 11\sqrt{3}a$, $t = 1$, $\lambda_R = 0.1$, and $\lambda_{SO} = \lambda_\nu = 0$	25

Figure 3.7. (a) Zigzag strip with an adatom impurity in the center of a hexagon in the middle of the scattering region. (b) Spin conductance and (c) valley polarization of the system shown in panel (a). Parameters used are $L = 20a$, $W = 67\sqrt{3}a/6$, $t = 1$, $\lambda_R = 0.1$, and $\lambda_{SO} = \lambda_\nu = 0$	26
Figure 3.8. (a) Zigzag strip with an adatom impurity on the carbon atom located on sublattice A. (b) Spin conductance and (c) valley polarization of the system shown in panel (a). Parameters used are $L = 20a$, $W = 67\sqrt{3}a/6$, $t = 1$, $\lambda_R = 0.1$, and $\lambda_{SO} = \lambda_\nu = 0$	26
Figure 3.9. (a) Zigzag strip with an adatom impurity on the carbon atom located on the sublattice B. (b) Spin conductance and (c) valley polarization of the system shown in panel (a). Parameters used are $L = 20a$, $W = 67\sqrt{3}a/6$, $t = 1$, $\lambda_R = 0.1$, and $\lambda_{SO} = \lambda_\nu = 0$	27
Figure 3.10. (a) Zigzag strip with two adatom impurities on the carbon atoms located on the sublattices A. (b) Spin conductance and (c) valley polarization of system shown in panel (a). Parameters used are $L = 20a$, $W = 67\sqrt{3}a/6$, $t = 1$, $\lambda_R = 0.1$, and $\lambda_{SO} = \lambda_\nu = 0$	27
Figure 3.11. (a) Zigzag strip with two adatom impurities on the carbon atoms located on the sublattices B. (b) Spin conductance and (c) valley polarization of the system shown in panel (a). Parameters used are $L = 20a$, $W = 67\sqrt{3}a/6$, $t = 1$, $\lambda_R = 0.1$, and $\lambda_{SO} = \lambda_\nu = 0$	28
Figure 3.12. (a) Zigzag strip with two adatom impurities on the carbon atoms located on the sublattices B and A. (b) Spin conductance and (c) valley polarization of the system shown in panel (a). Parameters used are $L = 20a$, $W = 67\sqrt{3}a/6$, $t = 1$, $\lambda_R = 0.1$, and $\lambda_{SO} = \lambda_\nu = 0$	28
Figure 3.13. Spin conductance and valley conductance for a zigzag strip with $L = 100a$ and $W \simeq 48.16\sqrt{3}a$ averaged over 1000 configurations with particular adatom densities: (a) 0.1, b) 0.2, and c) 0.3. Spin conductance and valley polarization fluctuations for the same systems with the same order of mentioned adatom densities: (d) 0.1, (e) 0.2, and (f) 0.3. Parameters used are $t = 1$, $\lambda_R = 0.1$, and $\lambda_{SO} = \lambda_\nu = 0$	29
Figure 4.1. (Color online) Slab of a topological insulator (green), current biased with I_{bias} . The induced spin accumulation at the boundaries can be injected into a side contact (blue). A gate potential V_{gate} can be tuned to control the spin polarization of the spin injected current.	33

- Figure 4.2. Surface spin polarization of a 3D topological insulator nanowire. (a) Sketch of a 3D topological insulator nanowire attached to two semi-infinite leads. (b) $\langle S_y \rangle$ and (c) $\langle S_z \rangle$ denote the spatial profile of the averaged spin polarization (averaged over 1000 disorder configurations) along cross sections, oriented in the $\hat{\mathbf{x}}$ direction and marked as the blue rectangle in panel (a). Parameters used are $L = 30a$, $W = 30a$, $H = 20a$, $H_{SP} = 10a$, $U_0 = 0.5\text{eV}$, and $E_F = 0.15\text{eV}$, which is in the bulk gap. 40
- Figure 4.3. Average ratios (a) $(\langle S_z \rangle / d\langle n \rangle / dx)_{-\hat{\mathbf{y}}}$ and (b) $(\langle S_y \rangle / d\langle n \rangle / dx)_{+\hat{\mathbf{z}}}$ as a function of disorder strength U_0 . The blue curves show the analytical and the red symbols the numerical results. Parameters in our simulations are $L = 30a$, $W = 30a$, $H = 20a$, and $E_F = 0.15\text{eV}$ which is in the bulk gap. 41
- Figure 4.4. Current-induced spin polarization into a side pocket at the top surface. (a-c) Spatial profile of the averaged spin polarization $\langle S_y(y, z) \rangle$ (averaged over 1000 disorder configurations) along cross sections in the $\hat{\mathbf{x}}$ direction shown as a dashed blue rectangle in panel (a). In panels (b) and (c) the side pockets are doped to hole bands ($V_{\text{gate}} = -0.8\text{eV}$) and electron bands ($V_{\text{gate}} = 0.9\text{eV}$), respectively. Common parameters are $L = 30a$, $W = 30a$, $H = 20a$, $H_{SP} = 10a$, $U_0 = 0.5\text{eV}$ and $E_F = 0.15\text{eV}$ which is in the bulk gap. 42
- Figure 4.5. Current-induced spin polarization into a side pocket at the side surface. (a) Sketch of a side pocket attached to the side surface of the system shown in Fig. 4.2(a). (b), (c) Spatial profile of the averaged spin polarization $\langle S_z(y, z) \rangle$ (averaged over 1000 disorder configurations) along cross sections in the $\hat{\mathbf{x}}$ direction shown as a dashed blue rectangle in panel (a). In panels (b) and (c) the side pockets are doped to hole bands ($V_{\text{gate}} = -0.8\text{eV}$) and electron bands ($V_{\text{gate}} = 0.9\text{eV}$), respectively. Common parameters are $L = 30a$, $W = 30a$, $H = 20a$, $W_{SP} = 10a$, $U_0 = 0.5\text{eV}$, and $E_F = 0.15\text{eV}$, which is in the bulk gap. 44
- Figure 4.6. Gate dependence of side pocket spin polarization. $\langle S_z \rangle$ averaged over 1000 disordered configurations and doped side pocket sites is plotted vs gate potential. We consider the following parameters: $L = 30a$, $W = 30a$, $H = 20a$, $W_{SP} = 10a$, $U_0 = 0.5\text{eV}$, and $E_F = 0.15\text{eV}$, which is in the bulk gap. The blue line is the best fitted line. 45

Figure 4.7. Spatial profile of the averaged spin polarization $\langle S_z(y, z) \rangle$ (averaged over 1000 disorder configurations) along cross sections in the \hat{x} direction for the system shown in Fig. 4.5(a). The side pocket is alternatively doped to electron bands ($V_{\text{gate}} = 1.3 \text{ eV}$) and hole bands ($V_{\text{gate}} = -1.1 \text{ eV}$). The side pocket is divided into four parts in the \hat{z} direction and the spatial profile is averaged over \hat{x} planes. Spin precession length in the \hat{z} direction, $\ell_{sp} \simeq 32a$ (considering $B_1 = B_2$). Other parameters used are $W_{SP} = 10a$, $L = 30a$, $W = 30a$, $H = 20a$, $U_0 = 0.7 \text{ eV}$, and $E_F = 0.15 \text{ eV}$, which is in the bulk gap. 45

Figure 6.1. The multilayer structure includes topological insulator layers and trivial insulator spacers (shown as blue layers). The induced magnetization direction due to introducing magnetic impurities (shown as red circles) is shown by the arrow in each topological insulator layer. . 62

Figure 6.2. The band structure of the Weyl semimetal lattice model. (a) Doubly degenerate 3D Dirac point when $H_1 = 0$. (b) Momentum-shifted Weyl point for $b_z = 1.0$ and $b_0 = 0$. In both panels, $\epsilon = 6t$, $\lambda = \lambda_z = 1.0$, and $t = 0.5$ 63

Figure 6.3. Junction of Weyl semimetals slabs with a pair of Weyl cone shifted in the \hat{z} direction in momentum space with (a) the identical chiralities and (b) reversed chiralities at the location of Weyl points. Weyl cones of different colors represent opposite chiralities. 64

Figure 6.4. (a) Schematic representation of a Weyl semimetal nanowire with a pair of Weyl cone shifted in the \hat{z} direction in momentum space. (b) Schematic representation of a Weyl semimetal junction with a pair of Weyl cone shifted in the \hat{z} direction in momentum space and have opposite chirality at the location of Dirac points as shown in Fig. 6.3(b). 66

Figure 6.5. Conductance of the systems shown in Fig. 6.4. The blue line shows the conductance of a Weyl semimetal nanowire the cones of which are separated in the \hat{z} direction, see Fig. 6.4(a). The red line illustrates the conductance of a Weyl junction where the sign of b_z terms are opposite in different regions, see Fig. 6.4(b). Parameters used are $\epsilon = 6t$, $\lambda = \lambda_z = 1.0$, $t = 0.5$, $b_z = |1.0|$, and $b_0 = b_x = b_y = 0$. . 67

Figure 6.6. Conductance of the systems the Weyl cones of which are separated in the (a) k_x direction, where $b_x = |1.0|$ and $b_y = 0.0$; and (b) k_y direction, where $b_x = 0.0$ and $b_y = |1.0|$. In both figures, the blue (red) lines show the conductance of a Weyl semimetal nanowire junction where the chiralities of Weyl points in region II are identical (opposite) with respect to the chiralities of Weyl points in region I. Common parameters are $\epsilon = 6t$, $\lambda = \lambda_z = 1.0$, $t = 0.5$, and $b_0 = b_z = 0$. 68

Figure 6.7. (a) The band structure of the broken inversion symmetry Weyl semimetal lattice model. (b) Conductance of the Weyl junction systems with broken inversion symmetry. The blue (red) line shows the conductance of a Weyl semimetal nanowire junction where the sign of b_0 term in region II is same (opposite) the b_0 term in region I. Common parameters are $\epsilon = 6t$, $\mathbf{b} = 0.0$, $|b_0| = 0.5$, $\lambda = \lambda_z = 1.0$, and $t = 0.5$. 69

Figure 6.8. Conductance of the Weyl junction systems in the presence of nonmagnetic impurities at the fixed energy, $E_F = 0.2$. (a) The blue (red) line shows the conductance of a Weyl semimetal nanowire junction where the sign of b_z terms are same (opposite) in Hamiltonian of regions I and II, see Fig. 6.4(b). We set $|b_z| = 1.0$ and $b_0 = 0$. (b) The blue (red) lines show the conductance of a Weyl semimetal nanowire junction where the sign of b_0 terms are same (opposite) in the Hamiltonian of regions I and II. We set $|b_0| = 0.5$ and $b_z = 0$. Common parameters are $\epsilon = 6t$, $b_x = b_y = 0.0$, $\lambda = \lambda_z = 1.0$, $t = 0.5$, and U_0 is the on-site disorder strength. 70

Figure 6.9. Conductance of the Weyl junction systems in the presence of magnetic impurities at the fixed energy, $E_F = 0.2$. (a) The blue (red) line shows the conductance of a Weyl semimetal nanowire junction where the sign of b_z terms are same (opposite) in Hamiltonian of regions I and II, see Fig. 6.4(b). We set $|b_z| = 1.0$ and $b_0 = 0$. (b) The blue (red) line shows the conductance of a Weyl semimetal nanowire junction where the sign of b_0 terms are same (opposite) in the Hamiltonian of regions I and II. We set $|b_0| = 0.5$ and $b_z = 0$. Common parameters are $\epsilon = 6t$, $b_x = b_y = 0.0$, $\lambda = \lambda_z = 1.0$, $t = 0.5$, and $M_z = 1.0$. 71

Figure A.1. The spin accumulation components (a) $\langle S_x \rangle$, (b) $\langle S_y \rangle$, and (c) $\langle S_z \rangle$ ($eV^{-1}a^{-2}$) averaged over 100 disorder configurations for a quantum wire. Parameters used are $\alpha = 0.2$, $W = 94a$, $L = 150a$, $U_d = 2$, and $E_F = 0.5$. $a = 1$ is the considered lattice constant. 93

Figure A.2. A 2D quantum wire with Rashba spin-orbit interaction (yellow) with an attached normal side pocket.	94
Figure A.3. Spin accumulation $\langle S_y \rangle$ ($eV^{-1}a^{-2}$) averaged over 1000 disorder configurations shown in Fig. A.2 with different length of contact between the scattering region and the side-pocket, (a) $L_H = 240a$, (b) $L_H = 180a$, and (c) $L_H = 50a$. Parameters used are a quantum wire with width $W = 112a$ and $L = 240a$ where an abrupt drop of the spin-orbit interaction strength is considered from $\alpha = 0.25$ for $y < 112a$, to zero for $y \geq 112a$, at the interface of the Rashba quantum wire and the normal side pocket; $L_{SP} = L$, $W_{SP} = 44a$, $U_d = 2$, and $E_F = 0.4eV$, see Fig. A.2. $a = 1$ is the considered lattice constant.	95
Figure A.4. A three-terminal junction where terminal three is a voltage probe and spin probe.....	96
Figure A.5. (a) Scattering region of a three-terminal junction, where the third terminal is a scanning tunneling microscopy tip that hovers over the system. Spin density and spin accumulation over Voltage for specified sites corresponding to (b) Red cut, (c) Green cut, (d) Blue cut, and (e) Purple cut shown in panel (a).	97
Figure D.1. Current-induced spin polarization into a side pocket at the side surface when $\eta = 0$. Spatial profile of the averaged spin polarization $\langle S_z(y, z) \rangle$ (averaged over 1000 disorder configurations) along cross sections in the \hat{x} direction. (a) $\langle S_z(y, z) \rangle$ corresponds to the system shown in Fig. 4.2(a). (b), (c) $\langle S_z(y, z) \rangle$ corresponds to the system shown in Fig. 4.5(a). In panels (b) and (c) the side pockets, $W_{SP} = 10a$, are doped to hole bands ($V_{\text{gate}} = -0.7eV$) and electron bands ($V_{\text{gate}} = 0.7eV$), respectively. Common parameters are $L = 30a$, $W = 30a$, $H = 20a$, $U_0 = 0.5eV$, and $E_F = 0.15eV$, which is in the bulk gap. We set $D_2 = 0$ in all parts of the system.	102
Figure F.1. The quintuple layer structure of the Bi_2Se_3 . The red rectangle denotes the stacking order of Se and Bi atomic layers along the \hat{z} direction where the Se2 atoms are considered inversion centers. Adopted form [155] with permission from the Springer Nature.	108
Figure F.2. Schematic of the band structure of Bi_2Se_3 . Originating from the atomic orbitals of Bi and Se, and the following four stages: (I) the hybridization of Bi and Se orbitals, (II) the chemical bonding, (III) the crystal field splitting, and (IV) the effect of the spin-orbit coupling. Adopted form [171] with permission from the American Physical Society.	109

LIST OF ABBREVIATIONS

3D Three-dimensional	1
SHE Spin Hall Effect	1
2DEG Two-dimensional Electron Gas	2
GMR Giant Magnetoresistance	2
2D Two-dimensional	7
1D One-dimensional	9
QSHE Quantum Spin Hall Effect	12
SGE Spin Galvanic Effect	32
ISGE Inverse Spin Galvanic Effect	32
LCAO Linear Combination of Atomic Orbitals	50
BC Boundary Condition	53
MR Magnetoresistance	59

1. INTRODUCTION

The scope of this thesis is the charge, spin, and valley transport in materials where the Dirac equation describes charge carriers dynamics. Specifically, we focus on graphene, three-dimensional (3D) topological insulators, and Weyl semimetals. We extend the existing transport theories for each material to include coherent spin and valley dynamics in confined or bulk structures. We use numerical methods for systems under consideration and study new transport phenomena and their possible applications.

Purpose of this Thesis

The main objective of this thesis is to investigate the quantal dynamics and interactions of internal quantum degrees of freedom such as charge, spin, and valley in Dirac materials. Since the Dirac equation describes the charge carriers dynamics, these materials feature richer transport phenomena than conventional semiconductors where the quantal dynamics is well-described by an effective Schrödinger-like equation. Our goal is to search for these new transport phenomena and study them. In particular, we follow on (1) Converting valley currents to spin currents and vice versa by introducing adatoms on graphene. Spin-polarized currents interact with the spin-orbit or exchange field, and they can be measured or read with phenomena such as inverse spin Hall effect (SHE) or with ferromagnetic probes. Although there are various theoretical proposals to induce valley currents, practical proposals to measure them have not been put forward, to best of our knowledge. The valley degree of freedom interact mainly with potentials that are concentrated in a very narrow space (comparable to the lattice spacing) as well as the armchair edges. Adatoms adhering to the graphene provide such potential. Adatoms deposited on graphene also induce spin-orbit interactions, hence showing potential to interact with both the valley and the spin currents. We focus on how valley currents and spin currents interact with adatoms and how valley currents can be converted into readable or measurable spin currents, bypassing an important milestone to design spin and valley-dynamics based devices. To achieve this, the development of a quantum transport theory that includes spin-valley interaction in graphene and the

utilization of quantum transport simulations, including adatom and spin-orbit effects, are studied. (2) Gate-controlled spin extraction from 3D topological insulator surfaces. An applied charge current induces spin accumulation on the surface of a 3D topological insulator. Manipulation of such spin accumulation typically require magnetic fields and lengthscales larger than the spin precession length. In this thesis, we find a mechanism in topological insulators that allows for local and all-electrical control of current generated spins with applied gates. The mechanism is based on the fact that the surface (edge) of three-dimensional (two-dimensional) topological insulators feature both electron- and hole degrees of freedom as well as spin-orbit coupling. We study the current-induced spins at the surfaces of 3D topological insulators and show how to extract these spins into topologically trivial materials commonly used in electronic and spintronics devices. We find that unlike the corresponding effect in two-dimensional electron gases (2DEGs) with Rashba spin-orbit interaction, the mixing of the electron and hole degrees of freedom at the topological insulator surface allows for additional spin manipulation methods. (3) Studying hyperfine interaction in Bi-based 3D topological insulators. The interaction between electron and nuclear spins, namely the hyperfine interaction, plays an essential role for ensemble spin dephasing and single spin decoherence of localized electrons. Furthermore, the hyperfine interaction enables us to study how to couple electron and nuclear spins controllably in spintronics devices. Expressions for different kinds of hyperfine interactions for surface states of 3D topological insulators are derived for the most common Bi-based 3D topological insulator models in this thesis. We extend our model to include the mixing of *s*-like orbital states with *p*-like orbitals such contributions can be important since *s*-like orbital states' contribution to hyperfine interaction is much stronger than *p*-like orbitals. Our calculations are general in the sense that they can be applied to any material within the Bi₂Se₃ family. (4) Magnetoelectric effect in Weyl semimetal nanowires. The three-dimensional version of graphene is a gapless system called Weyl semimetal. These systems typically require that either time-reversal symmetry or inversion symmetry is broken. The Dirac nodes can be split in the momentum space leading to (at least) two Weyl nodes of opposite chirality. These nodes (valleys), which can be shifted in the momentum space through different perturbations, can be annihilated in pairs if two nodes of opposite chirality overlap and gap out. Each Weyl node can be viewed as a magnetic monopole in momentum space. One can envision to use these properties to introduce different applications in the spintronics field. In this thesis, we study transport in various Weyl semimetal heterostructures in which the nodes with specific chirality are modulated. We find a new magnetoelectric effect in our systems that introduces a new giant magnetoresistance (GMR) type device, where manipulating chiralities can manipulate the charge transport. We also investigate

the robustness of this effect in the presence of magnetic and nonmagnetic disorder.

Contents of this Thesis

The thesis is organized in the following way:

In chapter 2, we briefly overview the Hamiltonians we focus on and review concepts that we will use in this thesis particularly required symmetries for protecting Dirac points and perturbations generating a finite gap for specific Dirac materials: graphene, topological insulators, and Weyl semimetals. We also overview some spintronics and valleytronics applications of these materials.

In chapter 3, we study the effect of adatom induced spin-orbit coupling on the band structure of graphene. We use numerical simulations to present current-induced spin accumulation at the edges of graphene nanowires with enhanced spin-orbit coupling. We also study the effect of a single adatom located at different sublattices on the spin and valley conductance. Then we focus on our main result, namely how valley currents transform into spin currents and vice versa by introducing adatoms in graphene. We also study how we can use these to design spin-valley converter devices for spintronics and valleytronics fields.

In chapter 4, we investigate the extraction of electrically-induced spins from the surface of topological insulators into adjoining topologically trivial materials conventionally used in electronics devices. We adopt an effective Hamiltonian applicable to a family of bismuth-based 3D topological insulator materials and consider a device geometry in which a topologically trivial side pocket is attached to various faces of a 3D topological insulator quantum wire. We show that it is possible to extract current-induced spin accumulation into these topologically trivial side pockets. We further study how this spin extraction depends on the geometry and material parameters and find that electron-hole degrees of freedom can be utilized to control the polarization of the extracted spins by an applied gate voltage.

In chapter 5, we study the hyperfine interactions between the electron and nuclear spin in materials belonging to the Bi_2Se_3 family. We utilize the effective Hamiltonian presented for such materials with the basis states including p -like symmetry states predominantly; hence, the dipole-dipole-like coupling and the electron-orbital to nuclear-spin coupling are significant hyperfine interactions. We also consider the possibility of s -orbital-mixing with less contribution to the states close to the Fermi energy, leading to the Fermi contact interaction which is the strongest one among all hyperfine interactions. We find effective expressions for hyperfine interactions for surface states of different planes of any 3D topological insulator materials in

the Bi_2Se_3 family. We investigate coupling of nuclear spin and inter-transition or intra-transition of surface states regarding surfaces of a 3D topological insulator crystal.

In chapter 6, we focus on Weyl semimetals for which either inversion symmetry or time-reversal symmetry is intact. We numerically and analytically study layered Weyl semimetal structures and expose an GMR-like effect. In particular we show that manipulating chiralities of Weyl points leads to blocking or unblocking the charge current. We also check this effect in dirty systems by introducing nonmagnetic and magnetic impurities. This magnetoelectric effect provides us to design a new chirality-valve device for electronics and valleytronics applications.

Lastly, in Chapter 7, we briefly outline our results in this thesis and discuss possible future directions.

2. OVERVIEW

Paul Dirac introduced the Dirac equation in the 1920s [1] to combine Einstein's special theory of relativity and quantum mechanics. In high energy physics, the quantal dynamics of relativistic fermions conform to the Dirac equation. For a free particle, the Dirac equation can be written as [2]

$$i\hbar\frac{\partial\psi}{\partial t} = (c\boldsymbol{\alpha}\cdot\mathbf{p} + \beta mc^2)\psi, \quad (2.1)$$

where $\mathbf{p} = -i\hbar\nabla$ is the momentum operator, m is the particle mass, c is the light speed, and ψ is a four-component spinor. Here $\boldsymbol{\alpha}$ and β form an algebra of anti-commuting 4×4 matrices and are given by

$$\alpha_i = \begin{pmatrix} \mathbf{0} & \sigma_i \\ -\sigma_i & \mathbf{0} \end{pmatrix}, \quad \beta = \begin{pmatrix} \sigma_0 & \mathbf{0} \\ \mathbf{0} & -\sigma_0 \end{pmatrix}, \quad (2.2)$$

where σ_i for $i = x, y, z$ are the Pauli matrices, σ_0 denotes a 2×2 identity matrix, and $\mathbf{0}$ denotes a 2×2 null matrix. This equation, which was originally intended to describe the relativistic behavior of the electron, predicted the antimatter for electron, named positron, as well as confirming electron spin. When kinetic energy dominates over rest mass ($cp \gg mc^2$), the particle behaves ultrarelativistically and the energy spectrum becomes linear. In this limit, two components of the upper and the lower parts of ψ decouple, and become an eigenstate of the chirality operator,

$$\Lambda = \frac{\boldsymbol{\sigma}\cdot\mathbf{p}}{p}, \quad (2.3)$$

where $\boldsymbol{\sigma}$ is the vector of Pauli matrices, with eigenvalues $\Lambda = \pm 1$. The eigenstates of the chirality operator are called the right-handed and the left-handed particles in which (pseudo)spin and momentum are parallel and antiparallel, respectively. At low energies, the right- and left-handed particles are also decoupled, provided that the particles are massless, $m = 0$. Although the electrons have a nonzero mass, the effective mass of carriers is sometimes negligible due to the complex environment of solids where charge carriers interact with each other and nuclei. Then the dynamics of the charge carriers of certain materials can also satisfy an effective Dirac equation.

In some cases, electronic band structure of solids host two linear band crossings at a single point, called Dirac point, around which we can apply Dirac Hamiltonian for the massless quasiparticles with an (emergent) chirality,

$$H = \pm v_F(\boldsymbol{\sigma} \cdot \mathbf{p}), \quad (2.4)$$

where we have Fermi velocity, v_F , instead of the speed of light. This is called a Dirac semimetal. It is also possible to separate the Dirac cones in momentum space using strain or magnetization. Then the resulting material is called a Weyl semimetal. In this chapter, we briefly survey Dirac/Weyl material properties and review some recent work related to these materials, particularly on the fundamental concepts in section 2.1 as well as the spintronics and valleytronics applications in section 2.2.

2.1 Dirac Materials

There has been a recent increase of experimental and theoretical interest in Dirac materials owing to their novel properties and their potential for applications. Examples of these materials in two-dimensions include graphene [3–6], topological insulator materials (such as HgTe and Bi₂Se₃) [7–10], MoS₂ [11], silicene [12], etc. In 3D we have 3D Dirac semimetal materials (like Cd₃As₂) [13–16], Weyl semimetal materials such as TaAs [16–18], etc. The list of these materials is increasing every day. The search for new Dirac and Weyl materials and studying their quantum properties are subjects at the frontier of condensed matter physics research. In conventional semiconductor materials, electrons obey the Schrödinger equation with (approximately) quadratic energy-momentum dependence. In contrast, the charge carriers dynamics in these new materials is determined with Dirac equation albeit with a different light-velocity constant. Hence, it becomes possible to observe analogs of relativistic, high energy effects in condensed matter systems at low energies. Apart from being interesting from a basic physics perspective, investigating these effects can pave the way for developing new devices with possible commercial applications.

In the rest of this section, we review some basic concepts such as effective Hamiltonian, symmetries needed to protect Dirac points, the effect of perturbations, etc., for specific Dirac materials, namely graphene, topological insulator materials, and Weyl semimetal materials.

2.1.1 Graphene

Graphene, a single layer of carbon atoms with a honeycomb structure, is perhaps the most well-known two-dimensional (2D) Dirac material [3]. There are two carbon atoms which represents different sublattices in each unit cell. In the vicinity of the Fermi level, the two linearly touching bands are mainly from carbon p_z orbitals that form π bands with adjacent atoms. Dirac points are present in momentum space at two distinct points: valleys K and K' . The effective Hamiltonian around the Dirac points conforms to the following equation [3, 16],

$$H_{\text{graphene}} = v_F(\tau_z\sigma_x p_x + \sigma_y p_y)s_0, \quad (2.5)$$

where $\mathbf{p} = (p_x, p_y)$ is the momentum of the particle in two dimensions, τ_i are the Pauli matrix in the valley space, s_0 is the unit matrix in the spin space, and σ_i are the Pauli matrices in the pseudo-spin (sublattice) space. Here s_0 indicates that there are two copies of Dirac cones at each valley.

The fundamental symmetries in graphene are inversion symmetry, $\mathcal{P} = \sigma_x\tau_x$, sublattice symmetry, $\mathcal{C} = \sigma_z$, time-reversal symmetry, $\mathcal{T} = \tau_x K_c$ (for spinless system) with K_c the complex conjugate operator. Inversion symmetry means $k \rightarrow -k$ and exchanges sublattices in the real space: $H(-k) = \mathcal{P}H(k)\mathcal{P}^{-1}$; sublattice (chiral) symmetry just interchanges sublattices A and B: $-H(k) = \mathcal{C}H(k)\mathcal{C}^{-1}$; and without considering the spin degree of freedom, the time-reversal symmetry operator in real space is just a complex conjugation operator: $H^*(-k) = \mathcal{T}H(k)\mathcal{T}^{-1}$. In both time-reversal and inversion symmetries, τ_x is the real operator that maps one valley to the other one. By breaking either sublattice symmetry or time-reversal symmetry in graphene, we can generate a gap, which manifests as a mass term in the Dirac equation. For example, a σ_z term preserves time-reversal symmetry but breaks sublattice symmetry as well as inversion symmetry, leading to a gap and drives the system to a quantum valley Hall insulator [19]. The source of this term can theoretically be an interaction of graphene with a specific substrate, which can be modeled as a different staggered potential. Intrinsic spin-orbit coupling, which is proportional to $\tau_z\sigma_zs_z$ term, can also open a gap. It only breaks sublattice symmetry and couples real spin to the pseudospin, and drives the system to the quantum spin Hall phase where the spin is locked to the momentum. However, spin-orbit strength is very weak for carbon atoms and consequently for graphene. On the other hand, there are some other 2D graphene-like materials such as silicene, germanene, stanene, and phosphorene [20–22] which all have higher spin-orbit strength since they are heavier elements and have buckled lattice structures. A substrate, adatoms, or an external electric field can break the inversion symmetry and generate

Rashba spin-orbit coupling, having the form $(\sigma_x \tau_z s_y - \sigma_y s_x)$. This interaction splits spin bands but does not cause any gap in the system. The other source of topological gaps can be the next-nearest neighbor hopping introduced by Haldane, which leads to a quantum anomalous Hall insulator [23]. Finite-size confinement is another example of generating a finite energy gap due to breaking translational symmetry causing momentum quantization. Any other term corresponding to the coupling between valleys results in translational symmetry breaking and can produce a gap, e.g., Kekule dimerization. For further discussions of these different gapped phases of graphene-like materials, we refer the reader to the literature [24].

2.1.2 Topological insulators

Topological insulators, another example of Dirac materials, have recently attracted considerable interest [10]. Topological insulators are band insulators that contain topologically protected extended states at the edges. Since these modes are topologically protected, they are not expected to be affected by weak disorder. The effective Hamiltonian of topological insulator materials with keeping only the four bands closest to the Fermi level is expressed as follows:

$$H_{\text{TI}} = v_F(\boldsymbol{\epsilon}(\mathbf{k}) \cdot \boldsymbol{\sigma})\tau_z + m_k\tau_x, \quad (2.6)$$

where σ_i are the Pauli matrices in the spin space and τ_i denote the Pauli matrices in the orbital space. We note that with the association of $\alpha_i = \sigma_i\tau_z$, $\beta = \tau_x$; and if $\epsilon_i(k) = t\sin(k_i a)$ and $m_k = m_0 + \sum_j t'(3 - \cos(k_j a))$, we recover the Dirac equation (2.1) as $\mathbf{k} \rightarrow 0$. In this approximation, v_F and m_0 take the place of the speed of light and the rest energy of the particle, respectively. The Hamiltonian of many different systems such as Bi_2Se_3 can be brought to this form. When the Fermi level is zero and $m_0 > 0$, a bandgap is present in the system and the system is in a trivial insulator phase, which is similar to the vacuum. When the mass parameter is negative, $m_0 < 0$, the system passes through a quantum phase transition from the normal dielectric or insulator vacuum to the topological insulator phase. In this phase, there is a bandgap in the bulk of the system and topologically conserved quantum states on the surface of the system.

Surface states of a topological insulator, which are effective in two dimensions, are depicted by a 2D Dirac equation similar to graphene. The effective surface Hamiltonian for surface states is,

$$H_{\text{surface}} = v_F(\mathbf{p} \cdot \boldsymbol{\sigma}) = v_F(p_x\sigma_x + p_y\sigma_y), \quad (2.7)$$

where $\mathbf{p} = (p_x, p_y)$ is the particle momentum (in two dimensions) which is parallel to the surface, and σ_i are the Pauli matrices in the spin space. Similarly, 2D topological insulators (some of which are also referred to as quantum spin Hall insulators) have edge states the Hamiltonian of which is governed by the one-dimensional (1D) Dirac equation. Surface (edge) states of the 3D (2D) topological insulators, where the number of Dirac cones on the topological insulators boundaries are odd, are robust to weak nonmagnetic impurity disorder [25,26]. Note that Kramer's theorem implies two counterpart edge or surface states with opposite spin and momentum at the same energy unless the time-reversal symmetry is broken. Hence, backscattering is suppressed because there is no available state for counter-propagating mode with the same spin. While spin-orbit coupling in topological insulators preserves the time-reversal symmetry, several types of perturbations like an out-of-plane magnetic field, proximity to magnetic materials, and magnetic impurities can be introduced to break the time-reversal symmetry and open a gap in the surface states of the topological insulators. The confinement effect can also generate a gap analogous to graphene.

2.1.3 Weyl semimetals

Stable band crossings have been known to occur in three dimensions, and if one can tune chemical potential near the vicinity of crossing points (namely 3D Dirac points) without the presence of other bands, the result is a 3D Dirac material with a linear Dirac spectrum. In this case the mass parameter in Eq. (2.6) is zero, $m_0 = 0$, and the particles are described by massless Dirac equation, which is a 3D generalization of graphene. However, in this case the valleys are located at the same point, not at two different momentum points as they are in the graphene. The valleys can be separated from each other through either breaking inversion symmetry by strain or time-reversal symmetry by the Zeeman field or magnetic exchange interaction. Hamiltonian with broken time-reversal symmetry and inversion exchange symmetry can be written in this form:

$$H = v_F(\boldsymbol{\epsilon}(\mathbf{k}) \cdot \boldsymbol{\sigma})\tau_z + m_k\tau_x + \lambda\tau_z + \boldsymbol{\beta} \cdot \boldsymbol{\sigma}, \quad (2.8)$$

where nonzero λ breaks inversion symmetry and nonzero β_i breaks time-reversal symmetry. If the valleys are separated in this way, increasing the mass parameter m_0 has a value different from zero, or adding any other perturbation can not create a bandgap in the system, as long as its strength is less than a critical value. This phase of the system consists of massless particles of opposite chirality, known as Weyl fermions. The phase is called "Weyl semimetal". The effective Hamiltonian

around each valley is

$$H_{\text{Weyl}}^{\pm} = \pm v_F(\mathbf{p} \cdot \boldsymbol{\sigma}) = v_F(p_x \sigma_x + p_y \sigma_y + p_z \sigma_z), \quad (2.9)$$

where \pm denotes the chirality of crossing points (Weyl points). The most important difference of this equation from graphene is the momentum of the particle which has components in three-dimensions, $\mathbf{p} = (p_x, p_y, p_z)$. We can easily open the band gap in graphene by applying a perturbation (e.g., staggered potential). On the contrary, this type of perturbation can only shift the position of the two Weyl points in momentum space and can not open a bandgap in Weyl semimetals, unless the Weyl points annihilate each other.

Wan et al. proposed the first "Weyl semimetal" candidate based on their first-principle calculations for the material $\text{Y}_2\text{Ir}_2\text{O}_7$. They identified 24 Weyl points and topological Fermi arcs on the surface in the semimetal phase [27]. Since then, there has been extensive experimental research on finding Weyl fermions in different materials [28–30] which had succeeded recently [18, 31–33]. As mentioned above, Weyl semimetal requires nondegenerate bands that can be obtained by breaking either time-reversal symmetry or inversion symmetry. These symmetries also put a constraint on the number of Weyl points. Breaking time-reversal symmetries lead to at least two Weyl points (minimum number based on fermion doubling theorem), and lack of inversion symmetry results in at least four Weyl points. When both symmetries coexist, the system is in a 3D Dirac semimetal phase where there are at least a pair of crossing points in the momentum space, two Weyl points with opposite chiralities. Also, Weyl materials occur in basic layered structures, including topological and trivial insulators [28] other than the adjustment of the crystal parameters. Moreover, at the transition point of topological and trivial insulators, we may either have 3D Dirac semimetals [34] or Weyl semimetals. Weyl points can only be annihilated in pairs of opposite chirality: once formed, one can only destroy a Weyl point by annihilating it (gapping it out) together with its partner having opposite chirality. This can be achieved by either breaking translational symmetry to allow scattering among Weyl cones or merging two Weyl points with opposite chirality in the momentum space.

The topological structure of the Weyl cones can be described mathematically as follows: The Berry curvature is defined as $\boldsymbol{\Omega}_n(\mathbf{k}) = \nabla_{\mathbf{k}} \times \mathbf{A}_n$, where \mathbf{A}_n is a k -space gauge potential, called Berry connection, for the band indexed n . Berry curvature can be viewed as a magnetic field in the momentum space. It becomes singular for a Weyl point, $\boldsymbol{\Omega}(\mathbf{k}) = \pm \mathbf{k}/2k^3$, therefore, Weyl points behave as monopoles. Hence,

we can define Chern number as a topological invariant for a 3D Weyl point,

$$N_S = \frac{1}{2\pi} \oint_S \boldsymbol{\Omega}(\mathbf{k}) \cdot d\boldsymbol{\sigma}, \quad (2.10)$$

where S is a closed surface in momentum space enclosing the Weyl point. The Chern number $N_S = \pm 1$ for a Weyl point, where $+1(-1)$ corresponds to the Weyl points chirality, that behaves as a source (sink) in the momentum space. Since the total flux must vanish for a crystal, the number of Weyl points are always even, also known as the fermion doubling theorem. In other words, periodicity guarantees that the intersection of any two bands occurs at an even number of points.

Fermi arc is one of the exotic physical consequences that arises from the Weyl semimetals' topological bandstructure. Unexpectedly at the surface of a Weyl semimetal, the Fermi surface does not form a closed loop. Instead, separate Fermi arcs located at opposing surfaces are present, and the reason is described briefly as follows: Consider a Weyl semimetal with a single pair of Weyl points. At the Fermi level, we have surface states in addition to the states associated with the bulk Weyl points. Unlike well-defined surface states for momenta away from the Weyl points because of no other bulk excitations available, surface states terminate at Weyl points and form an arc between two Weyl points at the surface. The Fermi arc surface states can also be described by noting that the Weyl points are Berry flux monopoles: Consider a 2D momentum space surface located between Weyl points and another located outside. There will be a non-zero net flux through these planes. Therefore, the Chern numbers corresponding to each 2D momentum space plane differ by one. Hence, (at least) one surface has a non-zero Chern number. Planes with non-zero Chern number can be described as 2D quantum Hall states in which chiral edge states cross the Fermi level. We arrive at a Fermi arc linking the two Weyl points by adding together the edge states of all potential 2D momentum space surfaces.

2.2 Applications of Dirac Materials

Dirac and Weyl materials have attracted great interest not only for rich underlying physics but also for their high potential for nanoelectronics applications. Spin and valley degrees of freedom, as well as their interactions in Dirac materials, have unveiled new avenues towards spintronics and valleytronics applications [12, 16, 35–46]. The creation, detection, and manipulation cycle of spins and valleys are fundamental necessities for spintronics and valleytronics, respectively. Having these possibilities open the gate to a future electronics with high speed data transfer, low energy con-

sumption and low power dissipation, etc. In this section, we briefly overview the utilization of graphene, topological insulators, and Weyl semimetals in spintronics and valleytronics fields.

2.2.1 Graphene

Graphene is one of the promising materials for spintronics and valleytronics applications where spin, pseudospin, and valley are alternatives to charge degrees of freedom used for electronic transport. Research on graphene spintronics applications was started when spin injection and detection in a single graphene layer system were demonstrated in 2007 [47]. Long spin coherence time is expected because of weak spin-orbit coupling of electrons and insignificant interaction between electrons spin and nuclear spins (hyperfine interaction) in graphene. Moreover, high mobility in graphene leads to a long spin-diffusion length. Thus, very high-efficiency spin transport and diffusion distances exceeding 100 microns have been obtained [48]. Therefore, graphene with weak spin-orbit interaction and long spin-relaxation time is ideal for spin-conserver, spin transistor, and memory applications in the spintronics field. Unlike these promising developments, experimental results for the spin lifetime were much shorter than expected: the expected spin lifetime at the microsecond level was found to be in the order of tens of nano-seconds [49, 50]. Recent theoretical research has shown that the adatoms on graphene can locally strengthen the spin-orbit interactions [51], and this mechanism explains the reduction of a spin lifetime. Adatoms [52, 53] similar to interaction with substrate [54], or applying an electric field [55–57] can enhance spin-orbit interaction, critical for the emergence of the SHE [58]. Graphene with enhanced spin-orbit coupling exhibits quantum SHE (QSHE), spin-polarized dissipationless states at the edges. Thus, graphene can be utilized for spin-polarized currents detection at elevated temperatures (even room temperature) because of its high mobility [59]. Graphene can also be utilized in complex spintronics devices such as reconfigurable logic gate [60].

In analogy with spintronics, it is possible to manipulate the valley leading to an alternative quantum transport field, valleytronics. In graphene, the definite chirality of valleys interacts differently with external perturbations and enables polarizing valleys at the same energy level by breaking the inversion symmetry [19, 61–63]. Similar to the SHE, we can have the valley Hall effect where valley current and polarization can be induced and controlled in graphene by an in-plane electric field [19]. Circularly polarized light [64] and valley-dependent Zeeman field [65] also induce and control valley polarization. The use of zigzag edge nanoribbons has provided promising theoretical recommendations for injecting valley polarized currents. How-

ever, manipulation and measurement of these currents are still challenging, although there has been experimental progress towards valley manipulation recently [45]. After creating valley polarization, one needs to manipulate them to be utilized for information storage and processing. Devices that allow transmitting of only one valley species, named valley filter devices, can be introduced for valley manipulation, and it is first proposed in graphene [66]. The other approaches have also been used to filter valleys in graphene, such as irradiation [67], line defects [68] strain engineering [69, 70], or the proposed valley polarized quantum anomalous Hall phase [71, 72]. In proposed valley filters, both valleys coexist and inter-valley scattering caused by disorder is one of the most critical obstacles for controlling polarization [73]. This issue is recently resolved by proposing a perfect valley filter at the boundary between two topological domains, quantum valley Hall with inversion symmetry broken and quantum anomalous Hall with time-reversal symmetry broken. Specific realizations of this perfect filter in a single layer and bilayer graphene are suggested [74]. Moreover, spin and valley can be mixed in graphene via inducing spin-orbit coupling by ripples, the substrate, or adatoms. This paves the way for utilizing spins to manipulate valley-spins and vice versa.

2.2.2 Topological insulators

Strong spin-orbit coupling and dissipationless spin-polarized counter-propagating edge states in two dimensions and topologically protected surface states in three dimensions make topological insulators promising candidates as spin-generators for spintronics applications [35, 42]. Graphene has also shown the QSHE effect, although this effect is weak for applications due to low spin-orbit interaction strength in graphene. A significant development in this area was achieved in 2006 by demonstrating the QSHE effect in HgCdTe quantum wells, which exhibited strong spin-orbit interaction [75]. Moreover, the current-induced spin accumulation effect can be found in topological insulator surface states due to the spin-momentum locking. Hence, topological insulators can also be used as a spin generator or charge-to-spin converter. The current-induced spin accumulation effect can also be utilized in heterostructures consisting of a topological insulator and a magnet in the way that spin accumulation on surfaces or edges of topological insulators can exert a spin-transfer torque onto the adjacent magnet to control magnetization [76]. Amazingly, spin accumulation in topological insulators has a much larger magnitude compared to those produced in trivial materials. Spin-to-charge conversion is also possible through spin pumping, spin-polarized tunneling [77], etc., on the topological insulators surfaces. In a 2D magnetic topological insulator, spin polarized chiral edge states can be utilized to generate and filter spin polarized currents [78]. Besides, introducing strain

to the bulk of Weyl, Dirac materials, or thin films also enables transition between the trivial and quantum spin Hall phases, proposing a piezo-topological transistor device [79]. An all-electric spin polarization rotator device is also introduced based on topological spin-helical edge states in 2D topological insulators and ferromagnetic contacts [80].

In short, topological insulators are efficient spin-current generator, accumulator, and filter. Utilizing topological insulators also enables us to efficiently manipulate spins and magnets of adjacent materials. Accordingly, various potential spintronics devices utilizing topological insulators have been proposed based on recent experimental results such as nonvolatile spintronic memory, [76, 81, 82] spin current/accumulation source [83–88], efficient spin detectors/spin-to-charge converters [89–93] and rechargeable spin battery [94]. Fast speed, low power consumption, and low heat dissipation are features of these devices.

2.2.3 Weyl semimetals

Weyl semimetals have recently attracted great attention and offer a new perspective for the next generation of spintronics and valleytronics devices [16, 61, 95–97]. While unintentional bulk doping is an obstacle in topological insulators for generating spin currents, there is no such concern in Weyl semimetals. Moreover, Weyl semimetals manifest a large Berry curvature and spin-orbit coupling [17], which results in a large intrinsic SHE that can be tailored to generate and detect spin currents. Although charge conductivity is low in these materials, the spin Hall angle, describing the conversion efficiency between charge currents and pure spin currents, is larger than other typical spin Hall systems. The presence of a Fermi arc is another distinct feature of Weyl semimetals with spintronics potential: Due to the spin-orbit coupling in Weyl semimetals, Fermi arcs can be nearly fully spin-polarized (up to 80% [98]).

Weyl semimetals host valleys making them also good candidates for valleytronics applications. The chiral anomaly effect in Weyl semimetals gives a charge imbalance, or valley polarization, between Weyl points, resulting in negative magnetoresistance [99, 100] that induces nonlocal transport and optical features [101, 102]. As mentioned above, Weyl points behave as magnetic monopoles in momentum space; therefore, the electron orbit is deflected according to the Weyl point chirality under a longitudinal force field. This phenomenon is called the chirality Hall effect which has no counterpart in 2D materials because it needs the third direction, normal to the motion plane, for transverse shifts [103]. Splitting carriers based on their chirality in addition to breaking inversion symmetry also induces an imbalance in carriers with different chiralities.

3D Dirac thin films, due to simple node configurations, can also be used for device applications. These materials can be in a trivial phase or quantum spin Hall phase through altering thickness, confinement along one direction, or transverse gating. This results in a topological field-effect transistor where we can control helical edge states for conducting spin currents [104].

Magnetic Weyl semimetals have great potential to be utilized in various spintronics applications such as data storage and information processing [105, 106]. Quantum anomalous Hall effect is observed at room temperature in these materials which leads to a new generation of low energy consuming spintronics devices [107]. Spin-polarized surface states in these materials can exert spin-transfer torque, necessary for operating spintronics devices such as racetrack memory.

3. ADATOMS IN GRAPHENE

In this chapter, we investigate the impact of deposited adatoms on graphene that is enhancement of the spin-orbit coupling. We overview trivial and topological phases of graphene with enhanced spin-orbit coupling or graphene-like materials hosting intrinsic spin-orbit coupling. We provide numerical results of current-induced spin accumulation that shows graphene (or graphene-like materials) can be utilized as a spin-generator. Furthermore, we explore how valley and spin currents interact with deposited adatoms on graphene. The most remarkable result of our study is that valley currents can be converted into spin currents and vice-versa with the aid of adatoms deposition through coupling spin and valley degrees of freedom. This provides a fertile ground for designing new spin-valley converter devices in spintronics and valleytronics fields.

3.1 Introduction

The possibility of utilizing the electron spin and valley degrees of freedom has been the focus of the emergent fields of spintronics and valleytronics, respectively. Exploring new phenomena and introducing applications based on spin and valley degrees of freedom are widely studied in these fields. Low power consumption, less heat dissipation, more compact, and faster reading or writing of data are the usually cited advantages of using spin and valley instead of the electron charge.

Graphene, a prominent 2D material hosting both spin and valley, has widely attracted attention in spintronics and valleytronics devices [35, 37, 45, 61]. Graphene is a great candidate as a spin-conserver in spintronics perspectives due to its weak spin-orbit coupling. Spin currents can be created by methods such as ferromagnetic contacts or spin Hall effect, manipulated by a magnetic field or spin-orbit field, and measured by ferromagnetic contacts and inverse spin Hall effect [108, 109]. The spin-orbit coupling can be enhanced in graphene by introducing adatoms, strain, and specific substrate as well as applying an external electric field so graphene can be used as a spin-generator. Furthermore, graphene-like materials such as silicene, germanene, stanene, etc., can also be utilized as spin-generators without adding

adatoms since they already have strong intrinsic spin-orbit coupling due to their higher atomic numbers and buckled structures [20–22]. Graphene-like materials and graphene with enhanced spin-orbit coupling could possibly exhibit the quantum spin Hall effect. On the other hand, in the scope of valleytronics, the valley Hall effect, which is analogous to the spin Hall effect, is predicted to be seen, and valley-polarized current can be induced in graphene by an in-plane electric field. However, manipulation and measuring valley currents have proven difficult, which has been a significant obstacle to the use of valleytronics applications.

The details of spin-relaxation in graphene are not still well-understood, even though there have been promising developments in utilizing graphene in spintronics and valleytronics fields. Experimental results for the spin lifetime are much shorter than theoretical expectations: the naive theoretical expectation of spin-relaxation time is in the order of microseconds, and it is experimentally found to be at most in the order of tens of nano-seconds [49, 50]. Recent theoretical research has shown that the adatoms, which can locally strengthen the spin-orbit interactions, [51] might explain the reduction of spin lifetime [110, 111]. The other theoretical approach for resolving this discrepancy is spin scattering by magnetic moments [112] and the interaction with the substrate [113]. According to the *ab initio* calculations, the induced Rashba spin-orbit coupling is one order of magnitude bigger than the intrinsic spin-orbit coupling [55, 114]. Therefore, the induced Rashba spin-orbit coupling possibly explains the observed spin-relaxation time. Here we focus on the spin-valley mixing caused by introducing dilute adatoms on graphene.

This chapter is structured as follows: In Sec. 3.2, we outline the Hamiltonian of graphene, including spin-orbit coupling, Rashba coupling, and staggered potential. Besides, we review quantum spin Hall phase and edge states in addition to the current-induced spin accumulation effect in graphene. In Sec. 3.3, we present that introduced adatoms on graphene induce spin-valley mixing and present the method for numerical calculations of spin and valley conductance. In Sec. 3.3.1, we numerically demonstrate how spin and valley are coupled through introducing adatom(s) on either one or both sublattices. Next, we investigate the effect of introducing random adatoms with different densities on spin and valley conductance and conclude in Sec. 3.4.

3.2 Quantum Spin Hall Effect

the first realization of Dirac fermions in condensed matter was graphene, a 2D honeycomb lattice which is one atom thick. The graphene lattice consists of two

sublattices, as shown in Fig. 3.1. The band structure of the Brillouin zone contains two isolated band touching points, called valleys, with locally linear dispersion relation as shown in Fig. 3.1. The effective Hamiltonian in the vicinity of the band touching point is the Dirac Hamiltonian:

$$H_{\text{graphene}} = v_F(\boldsymbol{\sigma} \cdot \mathbf{p}) = v_F(\sigma_x p_x + \sigma_y p_y), \quad (3.1)$$

where v_F is the Fermi velocity, $\mathbf{p} = (p_x, p_y)$ is the 2D momentum, and the Pauli matrices are in the space of the two sublattices, so-called pseudospin space.

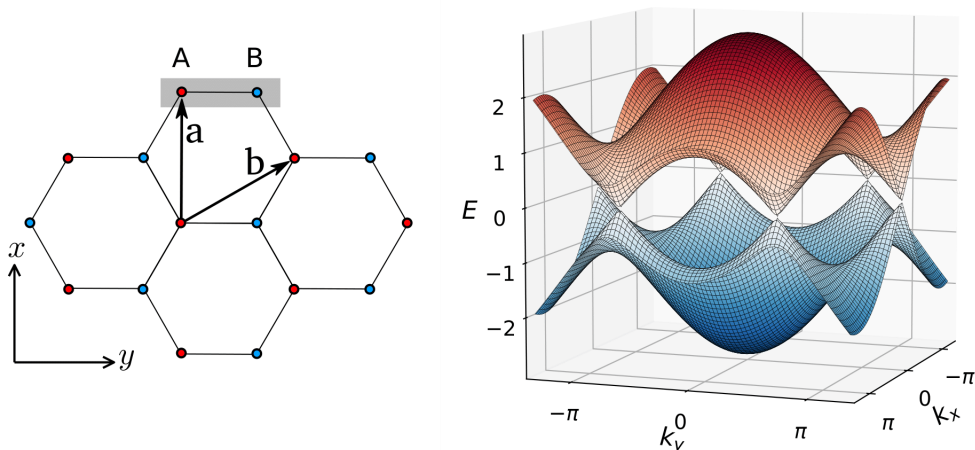


Figure 3.1 Illustration of the graphene lattice (left) and the band structure (right). A and B denote different sublattices. \mathbf{a} and \mathbf{b} are two primitive vectors of the Bravais lattice.

A finite gap can be opened through any perturbation including σ_z , which anti-commutes with the other two Pauli matrices in Eq. (3.1), and plays the role of a mass term in the Dirac Hamiltonian. The source of such gap-inducing perturbations can be adatoms, the substrate, and strain. An intrinsic spin-orbit coupling that breaks sublattice symmetry can also open a finite energy gap. Hence, an ideal sheet of graphene has an intrinsic energy gap that induces a time-reversal invariant topological insulator phase of matter distinct from an ordinary insulator. In the topological insulator phase, protected helical edge states reside in the bulk gap, and their spin is locked to the momentum. Edge states are robust to nonmagnetic disorders, and backscattering is forbidden. Even though the spin-orbit gap in graphene is too small, there are other materials the structures of which are similar to graphene, referred to as graphene-like materials, such as silicene, germanene, and stanene with intrinsic strong spin-orbit coupling which may lead to quantum spin Hall effect. Moreover, spin-orbit strength can be boosted by applying the electric field or introducing substrate or adatoms [115–120].

In order to model the intrinsic spin-orbit interaction, Kane and Mele have proposed the following tight-binding Hamiltonian with time-reversal invariant spin-orbit interactions [121]:

$$H = t \sum_{\langle ij \rangle} c_i^\dagger c_j + i\lambda_{\text{SO}} \sum_{\langle\langle ij \rangle\rangle} \nu_{ij} c_i^\dagger s_z s_j + i\lambda_{\text{R}} \sum_{\langle ij \rangle} c_i^\dagger (\mathbf{s} \times \hat{\mathbf{d}}_{ij})_z c_j + \lambda_{\nu} \sum_{\langle ij \rangle} \xi_i c_i^\dagger c_i. \quad (3.2)$$

Here c_i^\dagger and c_i are the annihilation and creation operators, respectively, and their indices refer to the honeycomb lattice site i . The first term is the well-known nearest neighbor hopping term with the amplitude t . The second term is the spin-orbit interaction that includes spin-dependent next nearest neighbor hopping with the amplitude λ_{SO} . Here $\nu_{ij} = \frac{2}{\sqrt{3}}(\hat{\mathbf{d}}_1 \times \hat{\mathbf{d}}_2)_z = \pm 1$, where $\hat{\mathbf{d}}_1$ and $\hat{\mathbf{d}}_2$ are unit vectors along the two bonds with respect to the assumed origin in the lattice. The third term is the nearest neighbor Rashba term, violating the mirror symmetry ($z \rightarrow -z$), with the strength λ_{R} appearing as a result of a perpendicular electric field or due to an adatom or interaction with a substrate. The fourth term is a staggered sublattice on-site potential ($\xi_i = \pm 1$), which breaks the sublattice symmetry and describes the transition between the quantum spin Hall phase and trivial insulator phase. Pauli matrices s_i denote the electron spin space.

In order to demonstrate the quantum spin Hall physics, we focus on a zigzag nanoribbon graphene (see Fig. 3.2(a)) with spin-orbit coupling. As illustrated in Fig. 3.2(b), edge states traverse in the bulk gap and connect two valleys, although the connection is not shown here. Moreover, the edge states are helical, i.e., states at each edge propagates in both directions with opposite spin due to time-reversal symmetry. This spin and momentum locking originates from the spin-orbit coupling and leads to spin-polarized edge states.

As mentioned above, in the quantum spin Hall phase, a single pair of time-reversal edge states traverses the bulk gap. These edge states are protected against small perturbations, and elastic backscattering is forbidden due to time-reversal symmetry; hence, no localization of edge states exists (unless the disorder is strong enough to disturb the bandstructure). In the trivial insulator phase, localized states can also be present at the edges, but these states are not robust against impurities in disordered systems, and get localized. Therefore, the edge states in the quantum spin Hall and insulating phases are distinguished by the number of edge state pairs modulo two, and the result is one and zero, respectively. Energy bands of these phases are shown in Fig. 3.3 for a zigzag strip.

In order to observe the QSHE in graphene, Kane and Mele found out that the intrinsic spin-orbit coupling should be stronger than the Rashba spin-orbit coupling

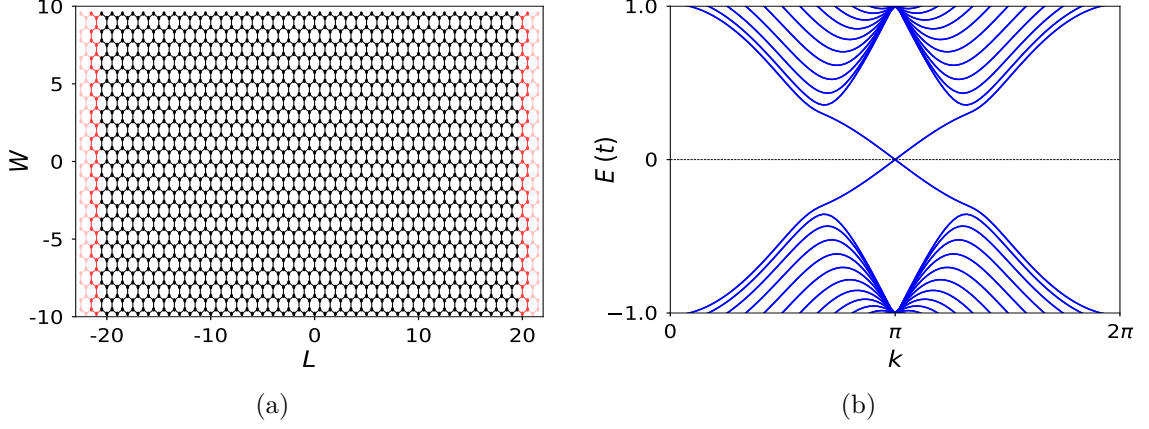


Figure 3.2 (a) Schematic of a zigzag nanoribbon graphene with $L = 40a$ and $W = 67\sqrt{3}a/6$, where a is the magnitude of the primitive vector along \hat{x} direction ($\mathbf{a} = a\hat{x}$). (b) Band structure of a the system shown in panel (a) in quantum spin Hall phase. Parameters used are $\lambda_{\text{SO}} = 0.06t$ and $\lambda_R = \lambda_\nu = 0$.

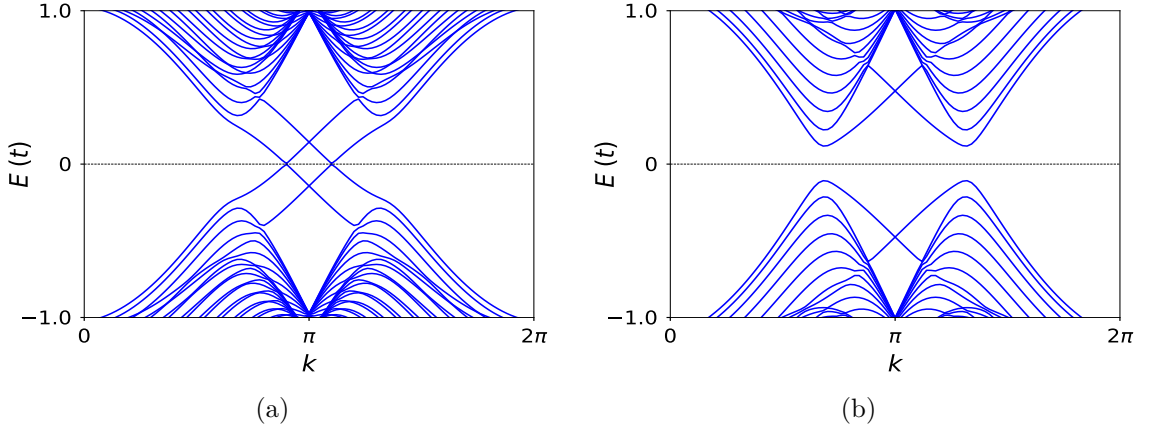


Figure 3.3 Energy bands for a zigzag strip shown in Fig. 3.2(b) in (a) the quantum spin Hall phase $\lambda_\nu = 0.15t$ and (b) the insulating phase $\lambda_\nu = 0.5t$. Parameters used are $\lambda_{\text{SO}} = 0.08t$, and $\lambda_R = 0.06t$. The edge states on a given edge cross at $ka = \pi$.

(see the full phase diagram as a function of λ_{SO} and λ_R [121]). Although later estimates show that the Rashba spin-orbit coupling is higher than the intrinsic spin-orbit coupling [55, 114], it has been proposed that the QSHE might be detected in rippleless graphene in the absence of an external electric field and at a temperature below $0.01K$ [114]. Moreover, it has been shown that the SHE remains even if disorders vanish the intrinsic spin-orbit gap [122].

The current-induced spin accumulation effect at the edges is one of the striking features of the quantum spin Hall phase when Fermi energy lies in the bulk gap (see Fig. 3.4(a) for an illustration of spin accumulation at the edges of a zigzag strip). By reversing the current direction, the spin polarization at the edges also reverses. We also present the current density and z -component of the spin current density

in Figs. 3.4(b) and 3.4(c), respectively, for incoming modes from the left lead. In the simulations, the Hamiltonian of the scattering region is given in Eq. (3.2), with nonzero t and λ_{SO} . It is worth noting that there is no spin accumulation in the insulating phase when the Fermi energy is in the bulk gap unless there are trivial states. The spin accumulation stemming from trivial edge states is suppressed in the presence of disorder since the trivial edge states get localized. Therefore, graphene with enhanced spin-orbit coupling and graphene-like materials can be considered to be a spin-polarized source in spintronics applications. Accumulated spins at the edges can be extracted to another material attached to the nanoribbon side analogous to 2DEGs with spin-orbit coupling. For more details, see Appendix A where we study how to extract accumulated spin from 2DEGs with spin-orbit coupling to the adjoining material without spin-orbit coupling.

3.3 Adatoms Induced Spin-valley Coupling

Adatom deposition on graphene can significantly enhance the spin-orbit coupling. For instance, induced Rashba spin-orbit coupling in Au adsorbed graphene can be about 200 meV [123]. In this section, we study how Rashba spin-orbit coupling induced by an adatom impurity influences the spin conductance and valley polarization (conductance) in graphene. There are different ways that adatoms can be deposited on graphene. The adatoms can be located above the center of each hexagon in the honeycomb structure or above the middle of the bonds between different sublattices or right on top of the carbon atoms. We find the effective Rashba spin-orbit coupling Hamiltonian generated by random, uncorrelated, and dilute adatoms on graphene through projecting the spin-orbit interaction on the bands to low energy states near the K point in the valley isotropic basis [51]. Using this procedure, we obtain

$$H_R = \lambda_R (\tau_0 \sigma_x s_y - \tau_z \sigma_y s_x), \quad (3.3)$$

$$H_{\text{spin-valley}} = \frac{i\lambda_R}{4} (\gamma_- \tau_- s_- - \gamma_+ \tau_+ s_+) \delta(\mathbf{r}_i - \mathbf{r}_a). \quad (3.4)$$

Here λ_R is Rashba coupling constant strength of which should be obtained from DFT calculations [51] and $\gamma_{\pm} = e^{\pm i\zeta(\mathbf{r}_a)}$ with $\zeta(\mathbf{r}_a) = \Delta\mathbf{K} \cdot \mathbf{r}_a$, where $\Delta\mathbf{K}$ is the momentum distance between two Dirac points and \mathbf{r}_a is the position of adatoms located randomly on carbon atoms, \mathbf{r}_i . τ_i , σ_i and s_i for $i = x, y, z$ denote Pauli matrices in the valley, sublattice and spin spaces, respectively. Subscript $i = 0$ identifies unit matrices. Eq. (3.3) is the Rashba type of spin-orbit coupling for graphene [114] with adatoms. Eq. (3.4) asserts spin-valley mixing induced by adatoms. we note that to the best of our knowledge, this term has not been addressed in previous studies,

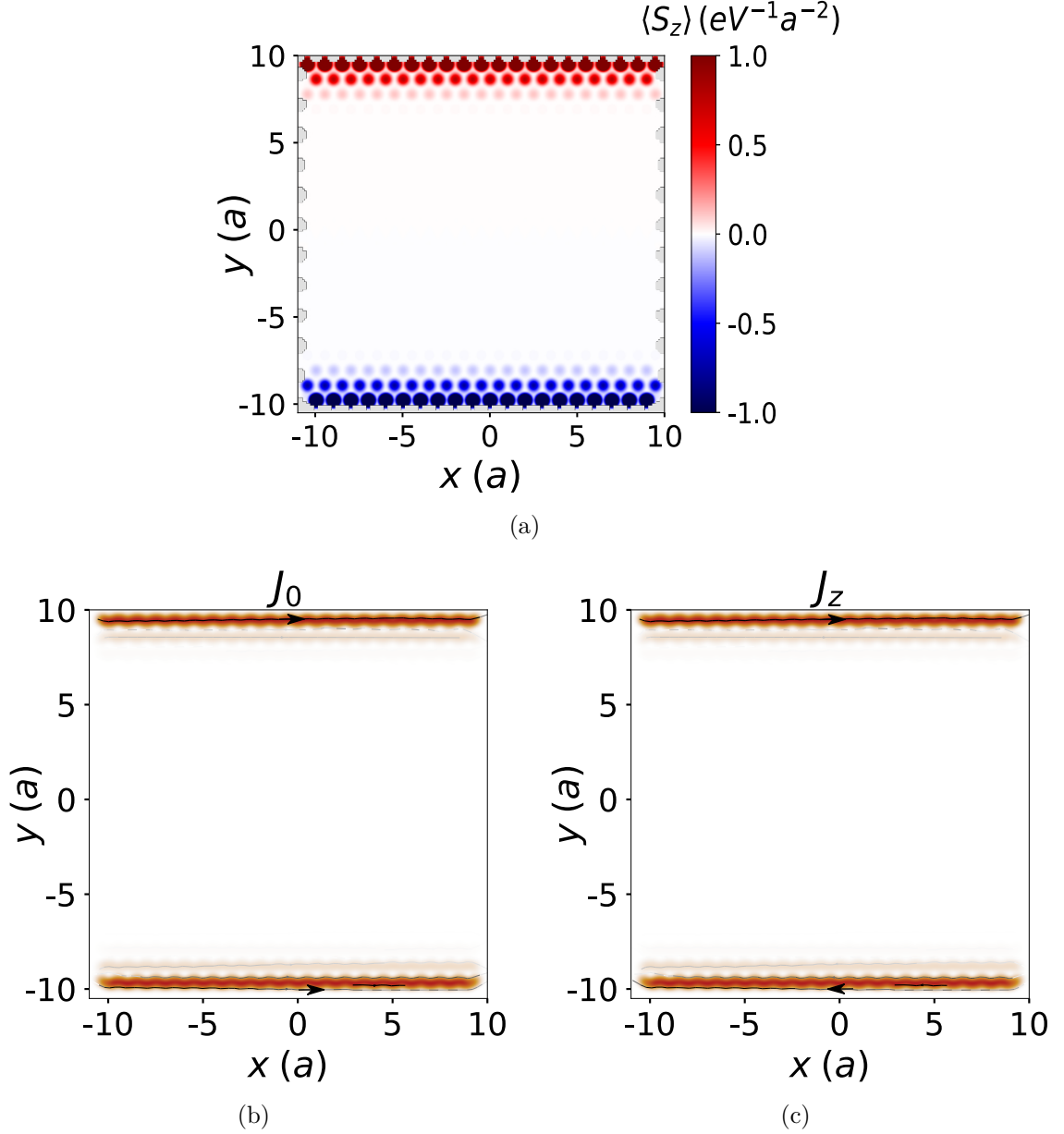


Figure 3.4 (a) $\langle S_z \rangle$ denotes spin polarization in a zigzag nanoribbon graphene. (b) Charge current density and (c) z -component of the spin current density in a zigzag nanoribbon graphene. Parameters used are $L = 20a$, $W = 67\sqrt{3}a/6$, $\lambda_{\text{SO}} = 0.06t$, and $\lambda_R = \lambda_\nu = 0$.

so it needs further attention and discussion. One of the outstanding utilization of spin-valley interaction is spin-to-valley conversion and vice versa, that may establish links between spintronics and valleytronics fields. Hence, graphene with engineering adatoms deposition can be used as a spin to valley converter since flipping the spin can induce a valley-flip.

Having discussed the analytical effective Hamiltonian of deposited adatoms on the graphene, we now perform numerical quantum transport simulations to verify the spin-valley coupling effect. In our numerical study, we use the tight-binding form of

Rashba Hamiltonian in Eq. (3.3) with nonzero λ_R term for nearest-neighbor hopping between sublattices where adatoms are deposited,

$$H = t \sum_{\langle ij \rangle} c_i^\dagger c_j + i\lambda_R \sum_{\langle ij \rangle} c_i^\dagger (\mathbf{s} \times \hat{\mathbf{d}}_{ij})_z c_j. \quad (3.5)$$

The Hamiltonian is essentially the Hamiltonian Eq. (3.2) without the intrinsic spin-orbit coupling and the staggered potential terms. We focus on a zigzag nanoribbon attached to two semi-infinite graphene, see Fig. 3.2(a). We now numerically evaluate spin conductance and valley polarization (conductance) with the aid of KWANT toolbox [124]. To calculate the spin conductance between two leads, we implement two approaches based on Green's function [125] and spin-dependent transmission probability [126]. According to Landauer formula, the spin- α component of the spin conductance is given in linear response as:

$$G_{pq}^{\sigma_\alpha} = \frac{e^2}{h} \text{Tr} [\sigma_\alpha \Gamma_q g_{qp} \Gamma_p g_{qp}^+], \quad (3.6)$$

where $\Gamma_q = i[\Sigma - \Sigma^+]$ is the coupling matrix to the lead q , g_{qp} is the submatrix of the system Green's function connecting sites which interfaces to leads q and p , σ_α is the Pauli matrix along direction α , and Tr denotes the trace. Through the scattering matrix approach, the spin conductance is obtained as [126]

$$G_{pq}^{\sigma_\alpha, \sigma_\beta} = \frac{e^2}{h} \sum_{q \neq p} T_{pq}^{\alpha\beta} = \frac{e^2}{h} \sum_{q \neq p} \sum_{m \in p, n \in q} \text{Tr} [t_{mn}^\dagger \sigma_\alpha t_{mn} \sigma_\beta], \quad (3.7)$$

where σ_α for $\alpha = x, y, z$ are the Pauli matrices and σ_0 is the (2×2) identity matrix. The trace is taken over the spin degree of freedom, and t_{mn} is a 2×2 matrix of spin-dependent transmission amplitudes from channel n in the lead q to channel m in the lead p . We set $\beta = 0$ since we assume that the reservoirs have no spin accumulation, so there is no injected spin current to the system. Eqs. (3.6) and (3.7) are equivalent ($G_{pq}^{\sigma_\alpha} = G_{pq}^{\sigma_\alpha, \sigma_0}$) and the later is more beneficial in terms of computational time cost. For simplicity, we use G_{S_α} for α -component of the spin conductance from now on. We calculate the valley conductance in the way that we subtract transmission probabilities of different valleys, e.g., K' , from the other one K , where each valley transmission probabilities are obtained through scattering matrix and defined as squared of transmission amplitudes from a specific valley in one lead to both valleys in the other lead. Therefore, the valley conductance is

$$G_K - G_{K'} = \frac{e^2}{h} \sum_{q \neq p} (T_{pq}^K - T_{pq}^{K'}). \quad (3.8)$$

Here $T_{pq}^K = \sum_{m \in p, n \in q} |(t_{mn}^K)^\dagger t_{mn}^K|^2$ is the transmission probability found through using t_{mn}^K which is a transmission amplitude from channel n in the valley K of the lead q to channel m in the valley either K or K' of the lead p . Note that we study spin and valley conductances through Landauer formalism in the limit of zero temperature and linear response regime (infinitesimal bias: $\mu_p \approx \mu_q \approx E_F$; $(\mu_p - \mu_q) \rightarrow 0$), where the currents are determined by the transmission probabilities at the Fermi energy according to Landauer formalism. Hence, spin conductance and valley conductance are also only depend on the transmission probabilities at the Fermi energy.

Valley polarization and spin conductance components under applied a small bias voltage (linear response approximation) are depicted in Figs. 3.5 for clean zigzag nanoribbon graphene attached to two leads having identical material properties shown in Fig. 3.2(a). Since there is no spin-orbit coupling and Rashba type term is zero in the absence of adatoms, there is no spin-momentum locking, leading to vanishing spin current. Valley polarization is always two (in units of quantum conductance, e^2/h) because of having one more set of degenerate K modes than K' modes at any E_F .

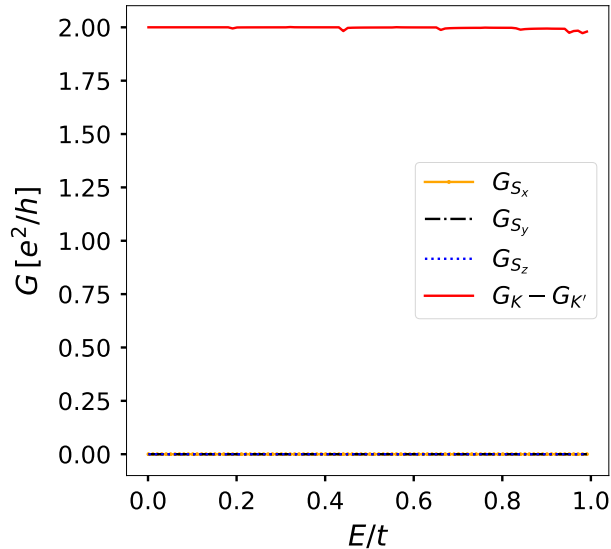


Figure 3.5 Spin and valley conductances in a clean zigzag nanoribbon graphene with $L = 20a$ and $W = 67\sqrt{3}a/6$.

Now, we add an adatom in the center of the scattering region, located on a carbon atom, shown in Fig. 3.6(a) as a green circle. Moreover, in Fig. 3.6(a), the Rashba coupling for the nearest neighbor bonds of the adatom are shown as red lines, and the next nearest bonds denote intrinsic spin-orbit coupling, which we ignore in our numerical simulations. We see in Fig. 3.6(b) that the deposited adatom induces s_z polarized conductance, and correlates valley and spin degrees of free-

dom. Fig. 3.6(c) demonstrates the reduced valley polarization, correspondingly. Fig. 3.6(d) illustrates that there is a good correlation between the z -component of the spin conductance and valley polarization difference between zigzag nanoribbon graphene with an adatom and a clean system. We also investigate the effect of a single adatom located in the center of a hexagon in the middle of the scattering region, shown in Fig. 3.7(a), where red bonds correspond to Rashba coupling due to the presence of an adatom. As illustrated in Figs. 3.7(b) and 3.7(c), we have in-plane, y -component, spin conductance, and a decrease in valley polarization compared to a clear zigzag system. Therefore, an adatom located in the hexagon or on the carbon atom leads to y - and z -components of the spin conductance, respectively. The small peaks and sharp dips at the specific energies correspond to opening a new transmission mode.

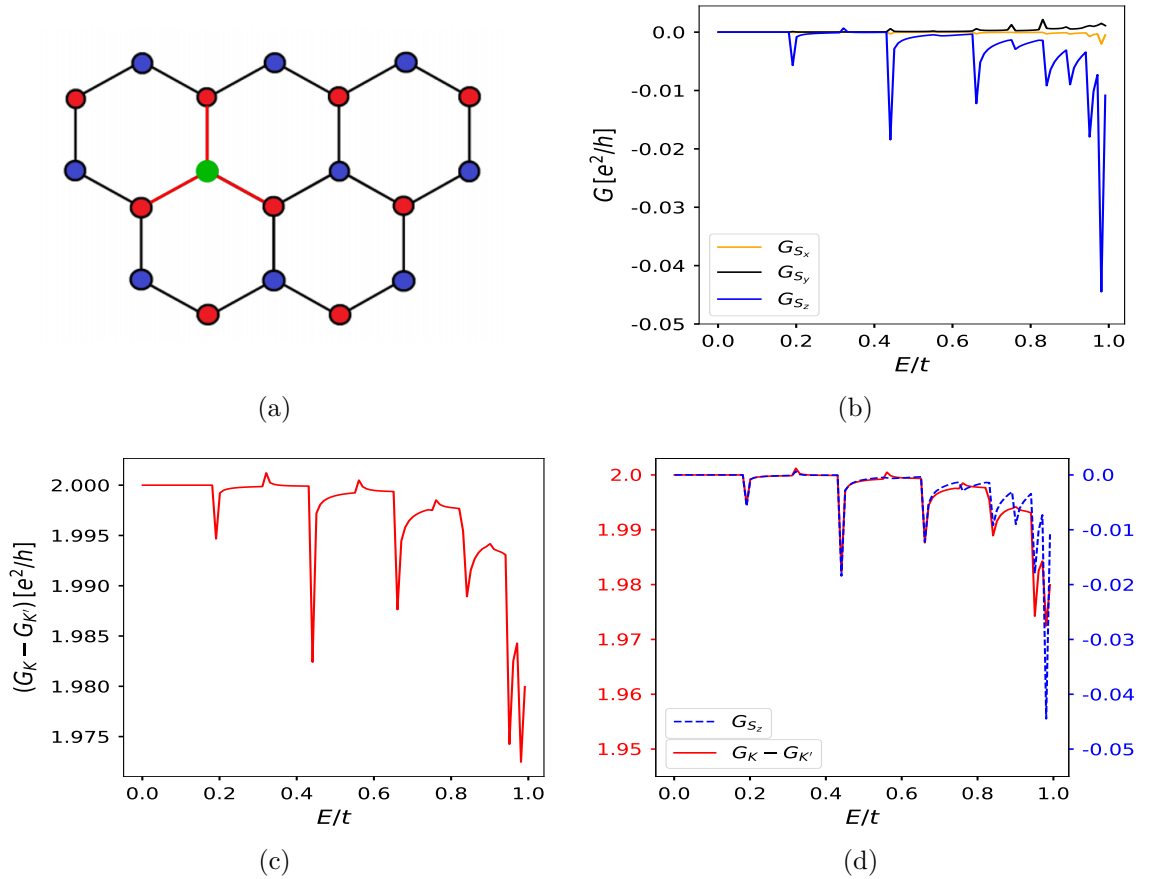


Figure 3.6 (a) Zigzag strip with an adatom impurity (green circle). (b) Spin conductance and (c) valley polarization of the system shown in panel (a). (d) The z -component of the spin conductance in addition to valley polarization for zigzag nanoribbon graphene with a Rashba impurity due to the presence of an adatom. Parameters used are $L = 20a$, $W = 11\sqrt{3}a$, $t = 1$, $\lambda_R = 0.1$, and $\lambda_{SO} = \lambda_\nu = 0$.

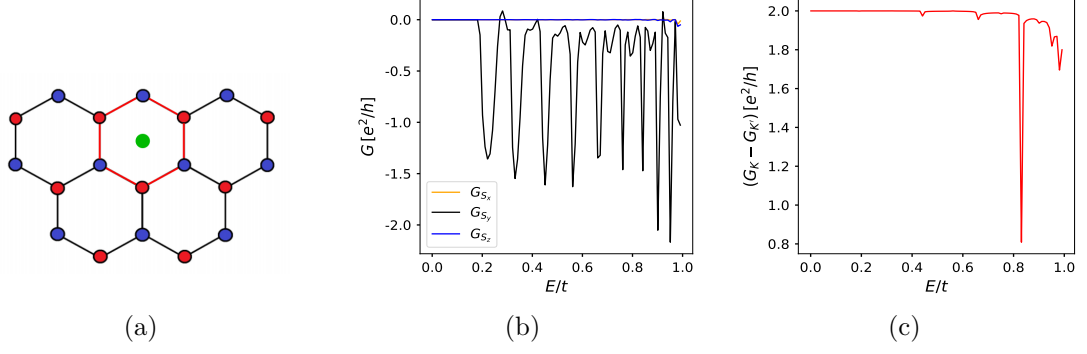


Figure 3.7 (a) Zigzag strip with an adatom impurity in the center of a hexagon in the middle of the scattering region. (b) Spin conductance and (c) valley polarization of the system shown in panel (a). Parameters used are $L = 20a$, $W = 67\sqrt{3}a/6$, $t = 1$, $\lambda_R = 0.1$, and $\lambda_{SO} = \lambda_{\nu} = 0$.

3.3.1 Adatoms on different sublattices

In this section, we study the behavior of adhering an adatom on the carbon located in either sublattice A or sublattice B in the zigzag nanoribbon. Based on our results presented in the previous section, we know the spin and valley are correlated through introducing adatoms. Here, we numerically explore how a deposited adatom on different sublattices influences the spin conductance and the valley polarization. Figs. 3.8 and 3.9 represent that the sign of z -component of the spin conductance is reversed when adatom is located on sublattice B compared to A while valley polarization is unaffected.

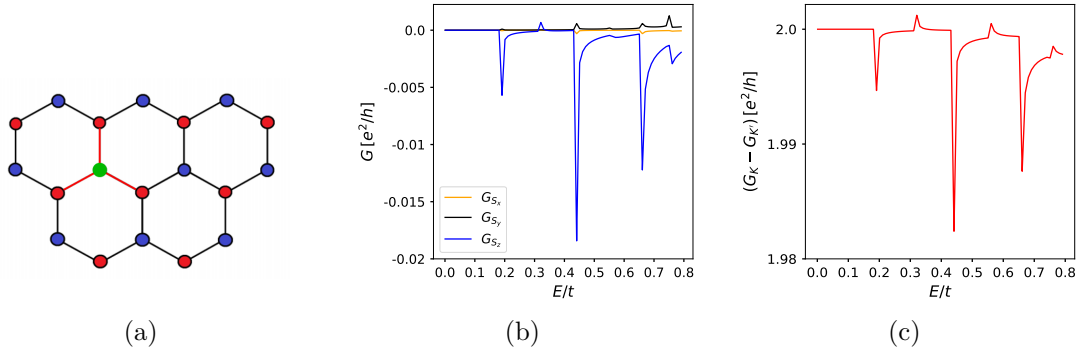


Figure 3.8 (a) Zigzag strip with an adatom impurity on the carbon atom located on sublattice A. (b) Spin conductance and (c) valley polarization of the system shown in panel (a). Parameters used are $L = 20a$, $W = 67\sqrt{3}a/6$, $t = 1$, $\lambda_R = 0.1$, and $\lambda_{SO} = \lambda_{\nu} = 0$.

We also survey the effect of two adatoms adhered to the carbon atoms on the same or different sublattices. Figs. 3.10 and 3.11 illustrate spin and valley conductance in the presence of two adatoms located on sublattices A and B, respectively. Like

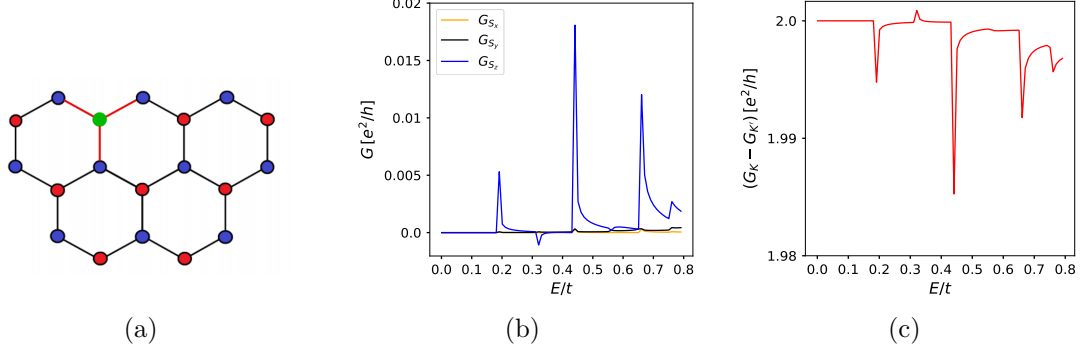


Figure 3.9 (a) Zigzag strip with an adatom impurity on the carbon atom located on the sublattice B. (b) Spin conductance and (c) valley polarization of the system shown in panel (a). Parameters used are $L = 20a$, $W = 67\sqrt{3}a/6$, $t = 1$, $\lambda_R = 0.1$, and $\lambda_{SO} = \lambda_\nu = 0$.

introducing one adatom, spin conductance has an opposite sign when adatoms deposit on sublattices B instead of sublattices A. In both cases, valley conductance trends are similar. Then we locate one adatom on the sublattice A and the other on the sublattice B, as shown in Fig. 3.12(a). We find that y -component of the spin conductance is also present in addition to z -component but with less magnitude, see Fig. 3.12(b). Since the spin-valley coupling depends on the position of the deposited adatoms and ΔK , a quantum fluctuation remains for spin conductance in case the adatoms are deposited on different sublattices. Valley conductance trend is similar to the cases that we have just one adatom on either sublattice A or B, see Fig. 3.12(c). In these figures, the sharp dips or peaks at the specific energies correspond to opening a new transmission mode.

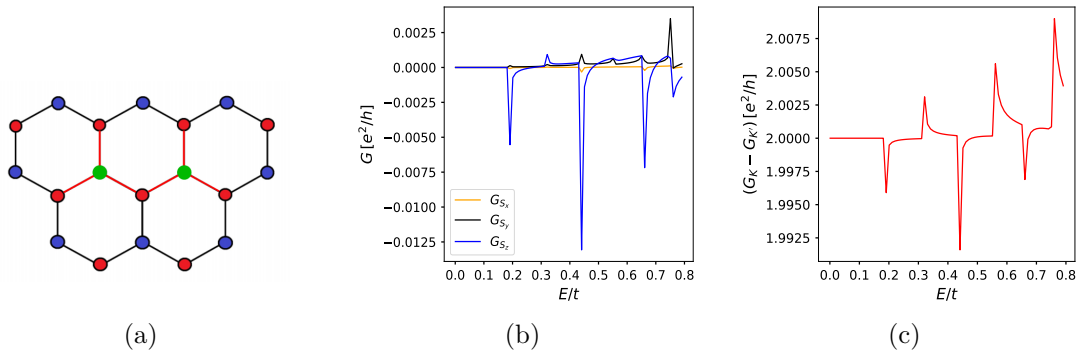


Figure 3.10 (a) Zigzag strip with two adatom impurities on the carbon atoms located on the sublattices A. (b) Spin conductance and (c) valley polarization of system shown in panel (a). Parameters used are $L = 20a$, $W = 67\sqrt{3}a/6$, $t = 1$, $\lambda_R = 0.1$, and $\lambda_{SO} = \lambda_\nu = 0$.

Furthermore, we study spin and valley conductance in a larger system with random adatom impurities. We consider different adatom densities and average over 1000

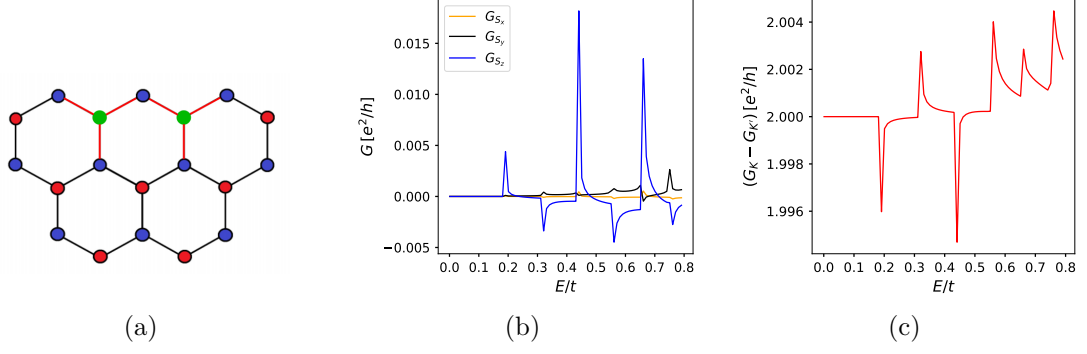


Figure 3.11 (a) Zigzag strip with two adatom impurities on the carbon atoms located on the sublattices B. (b) Spin conductance and (c) valley polarization of the system shown in panel (a). Parameters used are $L = 20a$, $W = 67\sqrt{3}a/6$, $t = 1$, $\lambda_R = 0.1$, and $\lambda_{SO} = \lambda_\nu = 0$.

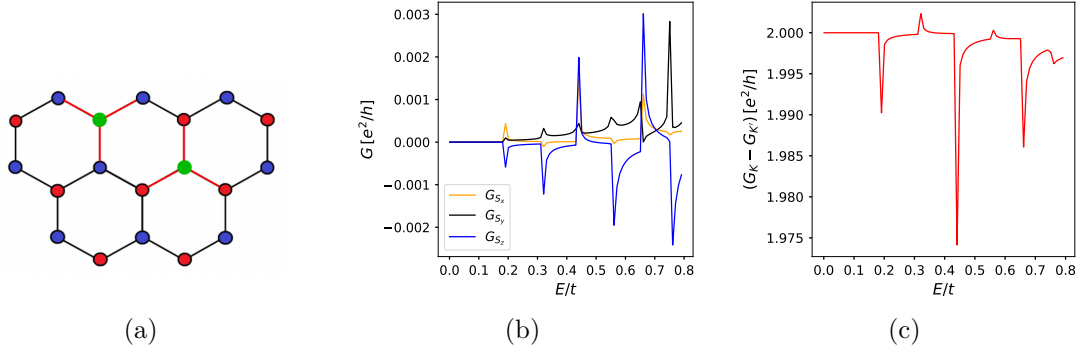


Figure 3.12 (a) Zigzag strip with two adatom impurities on the carbon atoms located on the sublattices B and A. (b) Spin conductance and (c) valley polarization of the system shown in panel (a). Parameters used are $L = 20a$, $W = 67\sqrt{3}a/6$, $t = 1$, $\lambda_R = 0.1$, and $\lambda_{SO} = \lambda_\nu = 0$.

configurations to find spin conductance and valley polarization and their fluctuations defined as

$$\Delta G_\alpha = \sqrt{\langle G_\alpha^2 \rangle - \langle G_\alpha \rangle^2} \quad (3.9)$$

with $\alpha = S_i$ for $i = x, y, z$ different spin conductance components. $\alpha = valley$ denotes valley polarization and $\langle \dots \rangle$ indicates averaging over different ensembles of the zigzag strip with random distributions of adatoms for a particular adatom density. The adatoms are not allocated to the specific sublattice in each configuration; i.e., random selection is used. To the best of our knowledge, the in-plane component of the spin conductance stems from the Rashba effect seen in different structures while the out-of-plane component of the spin conductance originates from spin-valley mixing effect. Hence, averaging over configurations with deposited adatoms results in vanishing out-of-plane component of the spin conductance since the spin-valley mixing depends on the location of adatoms. Fig. 3.13 illustrates this effect as well as the

adatom density does not affect the spin and valley conductance averaged over 1000 configurations, but it influences the ΔG_α . The increase in adatom density reduces spin and valley conductance fluctuations even though their trends are preserved. The important difference arisen in systems with more deposited adatoms is that the out-of-plane (z -component) spin conductance vanishes, and y -component of the spin conductance appears instead as we formerly found the emergence of G_{S_y} when adatoms deposited on different sublattices.

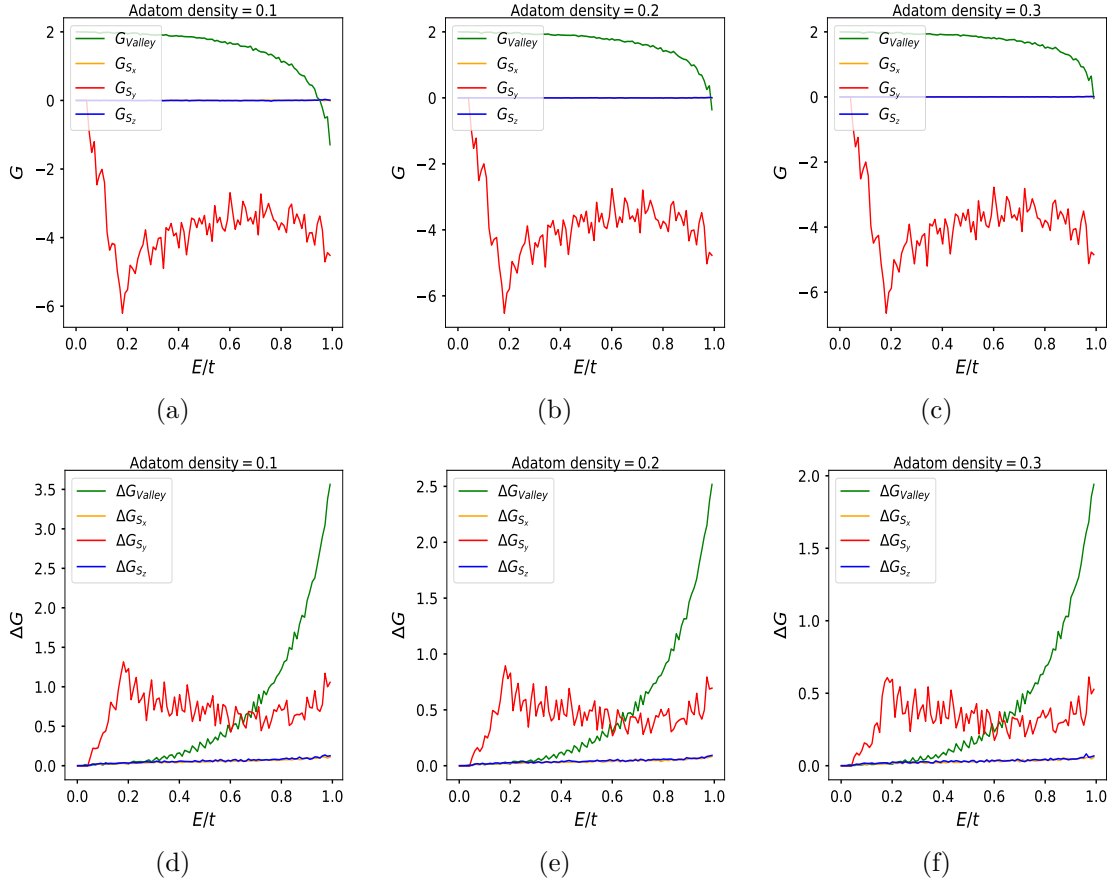


Figure 3.13 Spin conductance and valley conductance for a zigzag strip with $L = 100a$ and $W \simeq 48.16\sqrt{3}a$ averaged over 1000 configurations with particular adatom densities: (a) 0.1, b) 0.2, and c) 0.3. Spin conductance and valley polarization fluctuations for the same systems with the same order of mentioned adatom densities: (d) 0.1, (e) 0.2, and (f) 0.3. Parameters used are $t = 1$, $\lambda_R = 0.1$, and $\lambda_{SO} = \lambda_\nu = 0$.

3.4 Conclusion

In summary, we investigated that graphene with enhanced spin-orbit coupling or graphene-like materials hosting intrinsic spin-orbit coupling could be applied in spintronics applications, especially as a polarized spin source. We have also obtained numerical results demonstrating that dilute deposited adatoms on graphene induce

the novel spin-valley interactions. We have found that the interplay between spin and valley degrees of freedom in graphene provides a powerful tool to achieve state-of-the-art spintronics and valleytronics devices. Our study provides the framework to improve graphene functionality and sheds light on the utilization of spin-valley mixing in detecting the valley polarization. Our research has improved our understanding of the adatoms effect, but future investigations need to be taken.

4. GATE-CONTROLLED SPIN EXTRACTION FROM TOPOLOGICAL INSULATOR SURFACES

In this chapter, we consider a mechanism in topological insulators that allows for local and all-electrical control of electrically generated spins with gates. In most spintronics (or spin-orbitronics) platforms, charge carriers are of a given type, either electron or hole, implying that local application of gates equally couples to both spin species. In others where electron and hole pockets might co-exist, there is no coherence between the electron or hole degree of freedom and the spin degree of freedom. As a consequence, electric gates cannot locally control local spin accumulations in conventional spintronics and spin-orbitronics platforms. On the other hand, the surface (or edge) of 3D (2D) topological insulators features both electron and hole degrees of freedom as well as spin-orbit coupling. Applied gates control the local potential, which couples oppositely to electrons and holes, and spin-orbit coupling allows for spin dependency of electron-hole degrees of freedom. We demonstrate below that this joint property allows for electronic control of spins locally within a region much smaller than the spin precession length, the lengthscale over which spins can be manipulated in conventional spintronics applications [40].

4.1 Introduction

The push towards the utilization of the electron's spin degree of freedom in common electronic devices, which are conventionally based on the manipulation of the electron charge, has matured to the field called spintronics [40]. The various lines of research in this field not only comprise questions of fundamental interest in spin physics but also focus on applications. Possible advantages of utilizing spin-based elements in comparison to charge-based electronic devices might be low power consumption and less heat dissipation, as well as more compact and faster reading or writing of data.

The ferromagnets [41, 127, 128] are the mainstream materials used in spintronics where the ferromagnetic exchange interaction causes the spin-dependency of transport, allowing the creation, manipulation, and detection of spins. However, after the

celebrated Datta-Das spin transistor proposal [129], it became clear that spin-orbit interaction can also be utilized for spin manipulation in electronic devices. As the Datta-Das setting still requires ferromagnetic leads, a parallel approach utilizing materials without intrinsic magnetism, such as paramagnetic metals and semiconductors with only spin-orbit coupling [130–132], has become an attractive alternative.

Various methods of spintronics implementations without ferromagnets have emerged and developed over recent years [133–143]. These methods are commonly based on (i) the SHE [138], where an applied electric current generates a transverse spin current, and (ii) Edelstein (or inverse spin galvanic) effect [133, 144], where an applied electrical current generates a nonzero spin accumulation. Once generated, as these spins drive spintronics circuits, they need to be further manipulated and ultimately detected. For detection, inverse effects corresponding to those mentioned above, namely the inverse spin Hall effect [145–149] and spin galvanic effect (SGE) [150–154] have been successfully utilized. Main methods for spin manipulation are based on exchange and Zeeman fields or spin-orbit coupling to induce spin precession. However, weak coupling requires long length scales over which the induced spins need to remain coherent. This is an issue as spin precession lengths are usually comparable to spin relaxation or dephasing lengths. Furthermore, the spin-orbit coupling needs to be controlled over the precession (hence manipulation) region, while spin generation in part of the circuit needs to remain unaffected. Hence, in order to close the creation, manipulation, and detection cycle reliably, additional electrical methods for spin manipulation are desirable.

As an explicit example, we consider 3D topological insulator materials of the Bi_2Se_3 family the effective model of which is extensively discussed in the literature [155–158]. Qualitatively, our conclusions should apply also to strained (3D) HgTe , though an equally successful effective model for such a system is still missing. We focus on a particular geometry (sketched in Fig. 4.1) and demonstrate how the spin extraction can be controlled in a region smaller than the spin precession length. In this geometry, the spins are generated by the SGE at the surface of the topological insulator. By attaching a side pocket and tuning the chemical potential on the pocket by an applied gate voltage, we demonstrate that the extracted spins can change their polarization, regardless of the generated spins on the topological insulator side.

This chapter is organized as follows: In Sec. 4.2.1, we outline the effective surface Hamiltonian of a 3D topological insulator and the corresponding spin operators. We then present the inverse spin galvanic effect (ISGE), also known as Edelstein effect,

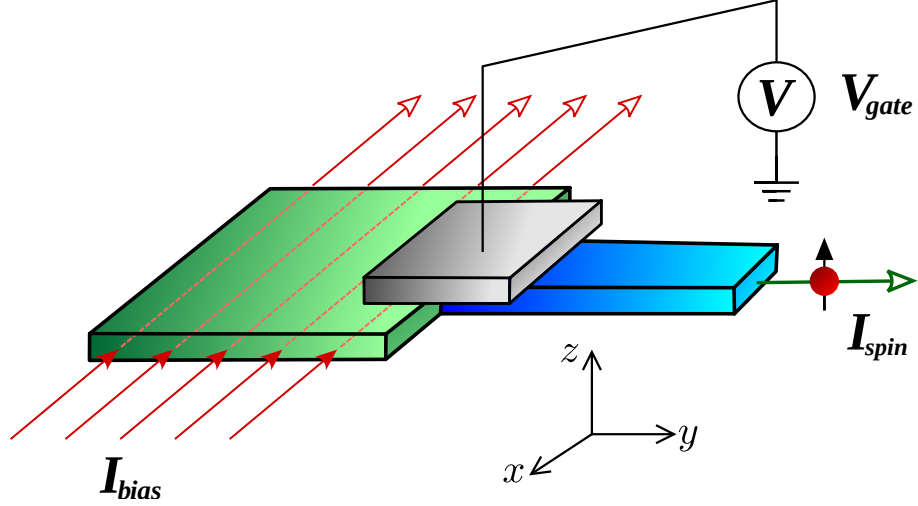


Figure 4.1 (Color online) Slab of a topological insulator (green), current biased with I_{bias} . The induced spin accumulation at the boundaries can be injected into a side contact (blue). A gate potential V_{gate} can be tuned to control the spin polarization of the spin injected current.

through Kubo formalism in Sec. 4.2.2. Different names addressing the same phenomenon are used in the literature depending on context. In Sec. 4.2.3, we state an ISGE paradox with its solution for the surfaces of a 3D topological insulator. Next, we discuss the model and the method proposed for extracting spin from surfaces of a 3D topological insulator in Sec. 4.3.1. In Sec. 4.3.2, we derive the spin behavior on the 3D topological insulator surfaces, which we show to be in close agreement with our numerical simulations. In Sec. 4.3.3, we demonstrate how to extract spins from 3D topological insulator surfaces and how to manipulate their polarization through a gate potential. We close with concluding remarks in Sec. 4.4.

4.2 A Spin-galvanic Paradox and its Solution

4.2.1 Setting the stage

Consider a finite crystal of an anisotropic 3D topological insulator material, such as Bi_2Se_3 , which in its topological insulator phase hosts topologically protected metallic surface states. The existence of these states, described by a single Dirac cone, was confirmed experimentally by angle-resolved photoemission spectroscopy [159, 160] and scanning tunneling spectroscopy [161–165] measurements. Further experiments confirmed the helical nature of such surface states [166]. The anisotropy of these materials implies that the topological metallic states existing on the different crystal faces will be described by Dirac-like effective Hamiltonians featuring different spin structures [156–158]. We are interested in the consequences of the anisotropy of

these materials on the ISGE [133, 144, 167]; for recent discussions see [168–170].

The states of the 2D helical surfaces of Bi_2Se_3 are admixtures of electron- and hole-like states of different parity (\pm) and spin ($\uparrow\downarrow$), coming from Bi and Se p_z orbitals, $|P1_z^+, \uparrow\downarrow\rangle$ and $|P2_z^-, \uparrow\downarrow\rangle$, respectively [155]. As a consequence, the real spin content of such states does not necessarily coincide with the pseudospin degrees of freedom used to label them. Hence, σ_i ($i = x, y, z$) denote the Pauli operators corresponding to the two bands at the surface (the pseudospin), while s_i are the spin operators within this restricted Hilbert space. The effective spin operators for any surface orientation are obtained by projecting the full spin operators of the combined electron and hole bands onto the relevant surface states (see Appendix B). As we show below, this projection misses key physics that we utilize to electrically control spin accumulations. The most commonly "known" low-energy effective Hamiltonian for the topological surface state is that of the "top" and "bottom" surfaces in the growth direction, which we choose to be in the $\hat{\mathbf{z}}$ direction:

$$H^{\pm\hat{\mathbf{z}}} = E_0(\hat{\mathbf{z}}) + v_F(\hat{\mathbf{z}})(\mathbf{k} \times \hat{\mathbf{z}}) \cdot \boldsymbol{\sigma}, \quad (4.1)$$

where $E_0(\hat{\mathbf{z}})$ is the energy of the Dirac point, $v_F(\hat{\mathbf{z}})$ is the corresponding Fermi velocity and \pm refers to the surface normals pointing away from the bulk. In this case, the spin and the pseudospin operators are the same:

$$\mathbf{s} = \boldsymbol{\sigma}. \quad (4.2)$$

This identification as well as the rotational symmetry, however is lost at the side surfaces:

$$H^{\pm\hat{\mathbf{y}}} = E_0(\hat{\mathbf{y}}) \pm v_{F,x}(\hat{\mathbf{y}})k_x\sigma_z \mp v_{F,z}(\hat{\mathbf{y}})k_z\sigma_x, \quad (4.3)$$

where $E_0(\hat{\mathbf{y}})$ is the energy of the Dirac point, and $v_{F,x}(\hat{\mathbf{y}})$ and $v_{F,z}(\hat{\mathbf{y}})$ are the corresponding Fermi velocity in the x and z directions, respectively. In this case, while the x components of the spin and the pseudospin operators are the same, they are merely proportional in the $\hat{\mathbf{y}}$ and $\hat{\mathbf{z}}$ surfaces with the proportionality parameter η :

$$s_x = \sigma_x, \quad s_y = \eta\sigma_y, \quad s_z = \eta\sigma_z. \quad (4.4)$$

For completeness, we express the $\pm\hat{\mathbf{x}}$ surface Hamiltonian as

$$H^{\pm\hat{\mathbf{x}}} = E_0(\hat{\mathbf{x}}) \mp v_{F,y}(\hat{\mathbf{x}})k_y\sigma_z \pm v_{F,z}(\hat{\mathbf{x}})k_z\sigma_y, \quad (4.5)$$

$$s_x = \eta\sigma_x, \quad s_y = \sigma_y, \quad s_z = \eta\sigma_z, \quad (4.6)$$

where $E_0(\hat{\mathbf{x}}) = E_0(\hat{\mathbf{y}})$, $v_{F,y}(\hat{\mathbf{x}})$ and $v_{F,z}(\hat{\mathbf{x}})$ are the Fermi velocities in the y and z directions, respectively. To summarize, the real spin coincides with the Pauli matrices $\sigma_i, i = x, y, z$ of the pseudospin only on the $\pm\hat{\mathbf{z}}$ surface. In particular, if $\eta \rightarrow 0$, the surface states on the $\pm\hat{\mathbf{y}}$ side have $s_y = 0, s_z = 0$. This point is crucial, as we discuss below.

4.2.2 Spin galvanic basics

We consider the spin accumulation, $s_z(\omega)$, generated in response to an applied electric field E_x in a spin-orbit coupled 2D system lying in the $\hat{\mathbf{x}}\text{-}\hat{\mathbf{z}}$ plane – corresponding to the side surfaces $\pm\hat{\mathbf{y}}$. The ISGE can be written in Kubo form [134] as

$$s_z(\omega) = \sigma_{\text{ISGE}}(\omega)E_x(\omega) \quad (4.7)$$

$$= \langle\langle s_z; J_x \rangle\rangle A_x(\omega), \quad (4.8)$$

where $\langle\langle s_z; J_x \rangle\rangle = \frac{-i}{\hbar} \int_0^t \langle [s_z(t), J_x(0)] \rangle e^{i\omega t} dt$ is the Kubo linear response kernel, A is the vector potential and σ_{ISGE} is the frequency-dependent ISGE conductivity. Thus

$$\sigma_{\text{ISGE}}(\omega) = \frac{\langle\langle s_z; J_x \rangle\rangle}{i\omega}. \quad (4.9)$$

Its Onsager reciprocal effect, the SGE, reads [154]

$$J_x(\omega) = \sigma_{\text{SGE}}(\omega)\dot{B}_z(\omega) \quad (4.10)$$

$$= \langle\langle J_x; s_z \rangle\rangle B_z(\omega), \quad (4.11)$$

yielding

$$\sigma_{\text{SGE}}(\omega) = \frac{\langle\langle J_x; s_z \rangle\rangle}{i\omega}. \quad (4.12)$$

In Eq. (4.11) \dot{B} is the time derivative of the magnetic field which generates the non-equilibrium s_z leading to the SGE.

4.2.3 Spin galvanic effect on the surface of a 3D topological insulator

As we stressed above, the relation between the pseudospin $\boldsymbol{\sigma}$ and the real spin \mathbf{s} on the 3D topological insulator surface can be anisotropic. The two quantities are identical on the $\pm\hat{\mathbf{z}}$ surfaces, and hence there is no ambiguity in calculating the ISGE and the SGE on the surfaces. However, on the $\hat{\mathbf{y}}$ surfaces

$$s_z = \eta\sigma_z. \quad (4.13)$$

On the surface of the topological insulator, spin and charge or momentum are locked. To be explicit we assume

$$J_x = v_{F,x}(\hat{\mathbf{y}})\sigma_z \quad (4.14)$$

with $v_{F,x}(\hat{\mathbf{y}})$ the Fermi velocity in the x direction (see Eqs. (4.1)-(4.3)). From Eqs. (4.13) and (4.14) one gets

$$J_x = \frac{v_{F,x}(\hat{\mathbf{y}})}{\eta} s_z. \quad (4.15)$$

Equation (4.15) seems to imply a divergent (“colossal”) SGE for $\eta \rightarrow 0$, while the ISGE should vanish.

This apparent paradox is resolved by judiciously inspecting the SGE and ISGE linear response kernels. First, for the SGE one has

$$J_x = \frac{\langle\langle J_x; s_z \rangle\rangle}{i\omega} B_z(\omega) \quad (4.16)$$

$$= \eta v_{F,x}(\hat{\mathbf{y}}) \underbrace{\frac{\langle\langle \sigma_z; \sigma_z \rangle\rangle}{i\omega}}_{L_{\sigma\sigma}} B_z(\omega), \quad (4.17)$$

which tends to zero for $\eta \rightarrow 0$ as it should: The pseudospin-pseudospin response function $L_{\sigma\sigma}$ defined above has no divergencies. Similarly for the ISGE holds

$$s_z = \frac{\langle\langle s_z; J_x \rangle\rangle}{i\omega} E_x(\omega) \quad (4.18)$$

$$= \eta v_{F,x}(\hat{\mathbf{y}}) \underbrace{\frac{\langle\langle \sigma_z; \sigma_z \rangle\rangle}{i\omega}}_{L_{\sigma\sigma}} E_x(\omega) \quad (4.19)$$

which is given by the same response function $L_{\sigma\sigma}$ and again vanishes in the $\eta \rightarrow 0$ limit.

4.3 Spin Extraction from 3D topological insulator Surfaces

Even though it turns out that there is no paradox in the form of a divergent SGE response, there are interesting consequences when considering $\eta \rightarrow 0$. In particular, as we show below, it is possible to extract current-induced spins from the side surfaces even if these are not spin polarized. The main idea is the following: at the side surfaces of a topological insulator, an analytical examination of the non-equilibrium population of the k_x states (induced by, say, an applied bias) reveals their composition to be a mixture of spin-up electron-like and spin-down hole-like quasiparticles the spins of which partially cancel each other. This is the origin of the parameter

$\eta \neq 1$ in general. In the limit $D_2 \rightarrow 0$ (hence $\eta \rightarrow 0$) the cancellation is perfect. Therefore, it suffices to contact the surface with a “pocket” containing electrons or holes—in practice, a gated semiconductor—so that only the spin-polarized electron- or hole-like part of the surface state will leak out of the topological insulator. A side pocket or lead thus acts as a gate-tunable spin extractor: The sign of the extracted spins can be reversed by simply switching the pocket polarity from n to p type or vice versa, allowing for local electrical control of spin polarization. Note the crucial observation that the size of the region where the spin is reversed can be shorter than the spin precession length (see Fig. 4.7 below).

4.3.1 Model and method

In the rest of this section, we further study the spin extraction effect through analytical and numerical means for 3D topological insulator nanowires. The wires are described by a 3D effective Hamiltonian which captures the basic low-energy properties of the Bi_2Se_3 family, including e.g. Bi_2Se_3 , Bi_2Te_3 and Sb_2Te_3 materials [155, 171]:

$$\begin{aligned} H^{3D} &= E(\mathbf{k})(\sigma_0\tau_0) + M(\mathbf{k})(\sigma_0\tau_z) + A_1 \sin k_z(\sigma_z\tau_x) \\ &+ A_2(\sin k_x(\sigma_x\tau_x) + \sin k_y(\sigma_y\tau_x)), \end{aligned} \quad (4.20)$$

where

$$\begin{aligned} M(\mathbf{k}) &= M_0 - 2B_2(2 - \cos k_x - \cos k_y) - 2B_1(1 - \cos k_z), \\ E(\mathbf{k}) &= C + 2D_2(2 - \cos k_x - \cos k_y) + 2D_1(1 - \cos k_z). \end{aligned}$$

Here, $\sigma_{x,y,z}$ and $\tau_{x,y,z}$ are the Pauli matrices, and σ_0 and τ_0 are the 2×2 identity matrices in spin and orbital space, respectively. If $(M_0/B_1 > 0)$ then the system is in the topologically nontrivial phase and Dirac-like surface states form within the bulk band gap. For a wire, due to the size quantization around the wire, the surface states form 1D channels and the lowest 1D subband is gapped due to its non-trivial Berry phase [172, 173].

In order to find the current-induced spin polarization on the 3D topological insulator nanowire surfaces, we need the spin operators expressed in the basis used to represent Eq. (4.20). The basis states are hybridized states of the Se and Bi p orbitals with even (+) and odd (−) parities and spins up (\uparrow) and down (\downarrow), namely $|P1_z^+, \uparrow\rangle$, $-i|P2_z^-, \uparrow\rangle$, $|P1_z^+, \downarrow\rangle$, and $i|P2_z^-, \downarrow\rangle$, in that order. Then the spin operators in the

basis of bulk states are given by [158]:

$$S_x = \sigma_x \tau_z, \quad S_y = \sigma_y \tau_z, \quad S_z = \sigma_z \tau_0. \quad (4.21)$$

Using the explicit forms of the spin operators, Eqs. (4.21), we generalize the Kubo response kernel of the effective 2D surface model of the previous section to the more realistic 3D model (4.20):

$$S_z(\omega) = \sigma_{\text{ISGE}}(\omega) E_y(\omega) \quad (4.22)$$

$$= \langle\langle S_z; J_y \rangle\rangle A_y(\omega) \quad (4.23)$$

with $S_z = \sigma_z \tau_0$.

The effective surface description is obtained by projecting in to the space spanned by the surface modes. One thus obtains the effective surface spin and Hamiltonian operators (see Appendix B). These surface Hamiltonians and modes for electrons on 3D topological insulator faces defined by their normals $\pm\hat{\mathbf{x}}, \pm\hat{\mathbf{y}}, \pm\hat{\mathbf{z}}$, were computed by Brey and Fertig [158]. In our geometry, the relevant surfaces are $\pm\hat{\mathbf{z}}$ and $\pm\hat{\mathbf{y}}$ where the projections of the spin operators follow Eq. (4.2) and Eq. (4.4), yielding the effective Hamiltonians Eq. (4.1) and Eq. (4.3), respectively. The parameters of surface Hamiltonians are then obtained from Eq. (4.20) [158] by projection. In particular, the band crossing energies of the $\hat{\mathbf{z}}$ and $\hat{\mathbf{y}}$ surfaces (which are the relevant surfaces for our choice of axes) are given by:

$$E_0(\hat{\mathbf{z}}) = C + \xi M_0, \quad (4.24)$$

$$E_0(\hat{\mathbf{y}}) = C + \eta M_0, \quad (4.25)$$

and the corresponding Fermi velocities are given by:

$$v_F(\hat{\mathbf{z}}) = A_2 \sqrt{1 - \xi^2}, \quad (4.26)$$

$$v_{F,x}(\hat{\mathbf{y}}) = A_2 \sqrt{1 - \eta^2}, \quad (4.27)$$

$$v_{F,z}(\hat{\mathbf{y}}) = A_1 \sqrt{1 - \eta^2}, \quad (4.28)$$

where

$$\xi = D_1/B_1, \quad \eta = D_2/B_2. \quad (4.29)$$

In our numerical study, we use the tight-binding representation of the Hamiltonian in Eq. (4.20) and focus on a 3D topological insulator wire attached to two semi-infinite leads (see Fig. 4.2(a)). We evaluate nonequilibrium local spin densities $\langle S_i \rangle(m) = \langle \psi_\alpha(m) | S_i | \psi_\alpha(m) \rangle$ for each site m , where $\psi_\alpha(m)$ is the wavefunction of

the (occupied) state α at site m and S_i are the spin operators defined in Eq. (4.21). We then sum over all occupied states α . For an infinitesimal bias, these are all scattering wavefunctions at a certain energy, E_F originating from one of the leads, depending on the sign of the bias. Local charge density is similarly obtained when $S_i \rightarrow \sigma_0 \tau_0$. We utilize the KWANT toolbox [124] for our numerical simulations. The parameters of our band Hamiltonian are chosen from the *ab initio* band-structure calculations of Bi_2Se_3 [171] in our numerical simulations. The particular values used are $A_1 = 2.2 \text{ eV}\text{\AA}$, $A_2 = 4.1 \text{ eV}\text{\AA}$, $B_1 = 10 \text{ eV}\text{\AA}^2$, $B_2 = 56.6 \text{ eV}\text{\AA}^2$, $C = -0.0068 \text{ eV}$, $D_1 = 1.3 \text{ eV}\text{\AA}^2$, $D_2 = 19.6 \text{ eV}\text{\AA}^2$ and $M = 0.28 \text{ eV}$. We have also set the lattice constant to be $a = 5 \text{\AA}$ in our numerical calculations.

4.3.2 Spin dynamics and accumulation at the surface

As a consequence of (pseudo)spin-momentum locking of the 3D topological insulator surface states, the dynamics of spin and charge are coupled [174, 175]. Thus, even nonmagnetic impurities can flip an electron's spin during scattering, leading to the dominant spin-relaxation mechanism. The situation here is similar to the so-called clean limit of the well-known spin-diffusion equations of a 2DEG with Rashba spin-orbit coupling [176], where the Dyakonov-Perel spin-relaxation time [177] is of the order of the momentum relaxation time. Hence, typical features of spin diffusion in standard semiconductors (which are in the “dirty” limit) such as the motional narrowing do not take place here. The steady-state spin-diffusion equation for the top (i.e., $\hat{\mathbf{z}}$) surface of a 3D topological insulator is given by [174], [see Appendix E for more details],

$$\frac{\Sigma_i}{\tau} = \frac{D}{2} \nabla^2 \Sigma_i + |\epsilon_{ij}| D \frac{\partial \Xi}{\partial x_j} - \epsilon_{ij} \frac{v_F}{2} \frac{\partial n}{\partial x_j}, \quad (4.30)$$

where $\Sigma_i, i = x, y$ are the in-plane components of the pseudospin density $\mathbf{\Sigma}$, $\Xi = \partial \Sigma_x / \partial y + \partial \Sigma_y / \partial x$, and n is the charge density. Furthermore, ϵ_{ij} is the 2D anti-symmetric tensor and $D = v_F^2 \tau / 2$ is the diffusion constant, with τ the momentum scattering time and v_F the Fermi velocity ($v_F(\hat{\mathbf{z}})$). We stress that these equations are valid only if the spin and charge accumulations vary appreciably at length scales much larger than the mean free path [175]. In the present work, we only consider geometries where this condition is satisfied. In order to obtain the equations applicable to the side surfaces, [$v_F = v_{F,x}(\hat{\mathbf{y}})$, see Appendix C], we generalize the diffusion equations to anisotropic surfaces and obtain the dependence of the real spin density

on the charge gradients due to the applied voltage bias:

$$\left(\frac{\langle S_z \rangle}{d\langle n \rangle/dx}\right)_{\pm\hat{y}} = \mp \left(\eta \frac{v_{F,x}(\hat{y})\tau}{2}\right)_{\pm\hat{y}}, \quad (4.31)$$

$$\left(\frac{\langle S_y \rangle}{d\langle n \rangle/dx}\right)_{\pm\hat{z}} = \pm \left(\frac{v_F(\hat{z})\tau}{2}\right)_{\pm\hat{z}}. \quad (4.32)$$

Hence, if E_F sits in the bulk gap, then applying a bias voltage yields surface currents flowing in the x direction, which in turn induces spin accumulations on the $\pm\hat{y}$ and the $\pm\hat{z}$ surfaces. This is the ISGE. In order to test these predictions, we numerically obtain spin densities via the method described in Sec. 4.3.1. Our results are shown in Figs. 4.2(b) and 4.2(c), where we plot the x -averaged cross-sectional profile for $\langle S_y \rangle$ and $\langle S_z \rangle$. Note that both components of the spin accumulation are localized to the respective surfaces and have opposite sign on opposite surfaces. Notice also that $\langle S_x \rangle = 0$ in our configuration since it is along the current direction. Furthermore, $\langle S_z \rangle$ is smaller than $\langle S_y \rangle$ for $\eta < 1$. The case $D_2 = 0$, as mentioned earlier, corresponds to a vanishing ISGE $\langle S_z \rangle$ and the "paradoxical" regime $\eta = 0$ of Sec. 4.2.

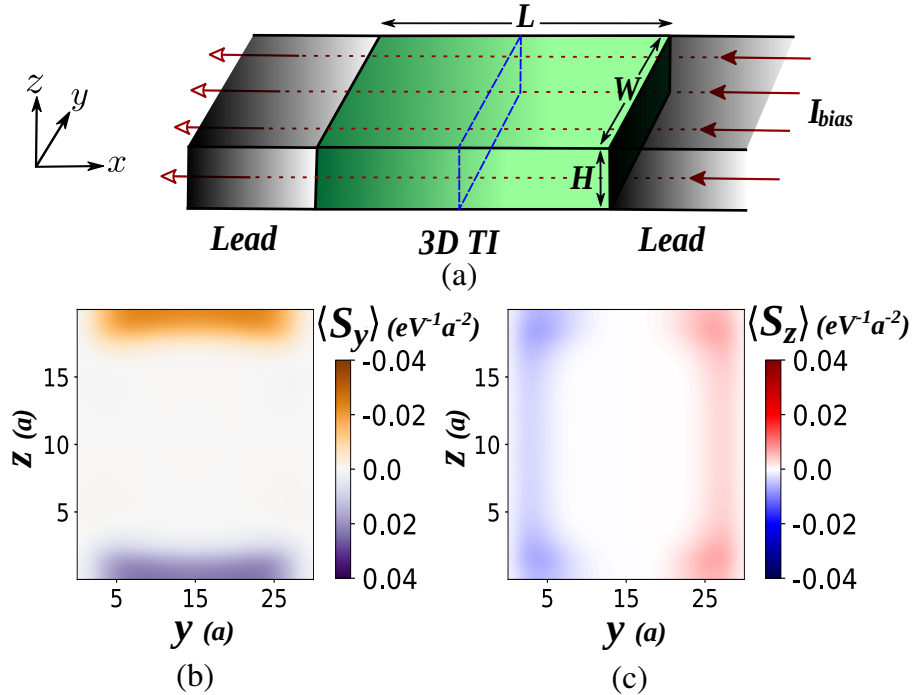


Figure 4.2 Surface spin polarization of a 3D topological insulator nanowire. (a) Sketch of a 3D topological insulator nanowire attached to two semi-infinite leads. (b) $\langle S_y \rangle$ and (c) $\langle S_z \rangle$ denote the spatial profile of the averaged spin polarization (averaged over 1000 disorder configurations) along cross sections, oriented in the \hat{x} direction and marked as the blue rectangle in panel (a). Parameters used are $L = 30a$, $W = 30a$, $H = 20a$, $H_{SP} = 10a$, $U_0 = 0.5\text{eV}$, and $E_F = 0.15\text{eV}$, which is in the bulk gap.

In order to test Eqs. (4.31) and (4.32) numerically, we consider the quotient on the left hand side of these equations as a function of disorder strength U_0 . Since in Fermi's "golden rule" regime $1/\tau \sim U_0^2$, we expect a U_0^{-2} behavior. In order to get the exact relation, we analytically calculate the mean free time using a $\mathbf{k} \cdot \mathbf{p}$ approximation for surface eigenmodes in Appendix C. Next, we perform numerical simulations and obtain the local spin or charge accumulations and average these over a square region in the middle of the $+\hat{z}$ and $-\hat{y}$ surfaces as well as over different disorder configurations with strength U_0 . Finally, we compare our analytical prediction (the blue line) for the left-hand sides of Eqs. (4.31) and (4.32) against the numerical simulations (red dots) in Figs. 4.3(a) and 4.3(b), respectively. We find that our numerical results for ISGE are well described by the analytical formulas in Eqs. (4.31) and (4.32).

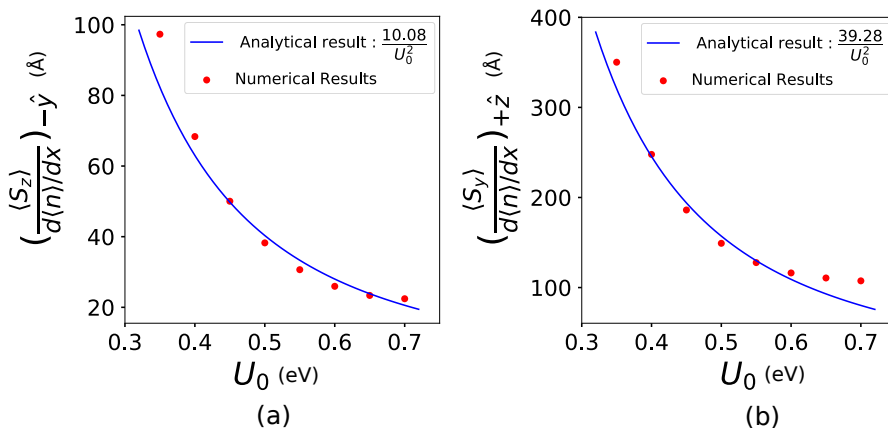


Figure 4.3 Average ratios (a) $(\langle S_z \rangle / d\langle n \rangle / dx)_{-\hat{y}}$ and (b) $(\langle S_y \rangle / d\langle n \rangle / dx)_{+\hat{z}}$ as a function of disorder strength U_0 . The blue curves show the analytical and the red symbols the numerical results. Parameters in our simulations are $L = 30a$, $W = 30a$, $H = 20a$, and $E_F = 0.15\text{eV}$ which is in the bulk gap.

4.3.3 Spin extraction

Having discussed how spins can be induced at a topological insulator surface, we now study how these spins can be extracted to be used in (presumably topologically trivial) spintronics circuitry. To this end, we focus on a geometry where a topologically trivial side pocket is attached to the topological insulator nanowire (see Figs. 4.4(a) and 4.5(a)). The current-induced spins at the topological insulator surface can then leak into the side pocket, generating nonzero spin accumulation inside the side pocket. The nanowire size is chosen such that its length and width $L = W = 15\text{nm}$ exceed the mean free path l , ensuring diffusive carrier dynamics. The mean free path is estimated in terms of the disorder potential strength U_0 using Fermi's "golden rule" (see Appendix C for details).

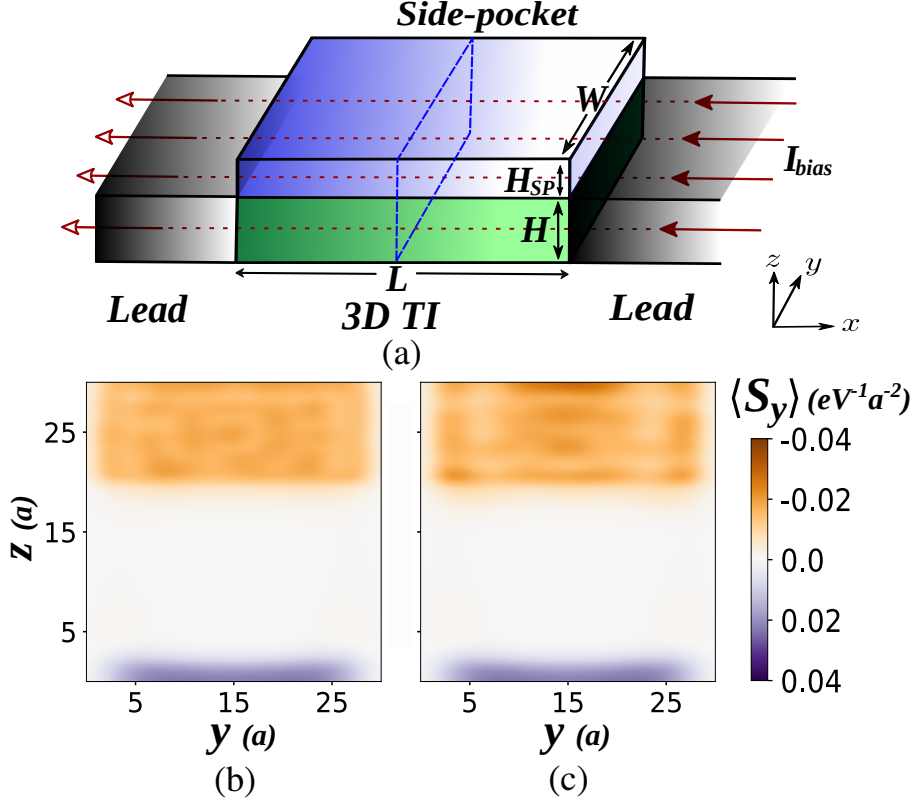


Figure 4.4 Current-induced spin polarization into a side pocket at the top surface. (a-c) Spatial profile of the averaged spin polarization $\langle S_y(y, z) \rangle$ (averaged over 1000 disorder configurations) along cross sections in the \hat{x} direction shown as a dashed blue rectangle in panel (a). In panels (b) and (c) the side pockets are doped to hole bands ($V_{\text{gate}} = -0.8 \text{ eV}$) and electron bands ($V_{\text{gate}} = 0.9 \text{ eV}$), respectively. Common parameters are $L = 30a$, $W = 30a$, $H = 20a$, $H_{SP} = 10a$, $U_0 = 0.5 \text{ eV}$ and $E_F = 0.15 \text{ eV}$ which is in the bulk gap.

Spin extraction can take place at pockets that are attached to either surface of the 3D topological insulator nanowire [see Fig. 4.4(a) and Fig. 4.5(a) for the geometry where the pocket is attached to the \hat{z} surface or the \hat{y} surface, respectively]. The pockets are gated in order to tune them to a metallic state, while charge carriers can be either electron- or hole-like states; thus, there is a coupling only to the electron- or hole-like spin-momentum locked components of the 3D topological insulator surface states. The gating is modeled by adding a corresponding on-site energy term in the tight-binding grid while keeping the other parameters of the effective Hamiltonian unchanged.

We perform tight-binding simulations and numerically calculate the current-induced spin polarization $\langle S_i \rangle$, ($i = y, z$), averaging over 1000 disorder configurations for a nanowire with side pockets. Figs. 4.4(b), 4.4(c) and Figs. 4.5(b), 4.5(c) show the spatial profile of the spin polarization along a perpendicular cross section for fixed doping values in the hole and electron bands, respectively. Focusing on the top (\hat{z})

surface, our simulations show all expected features: A substantial non-equilibrium spin accumulation can be extracted into the doped side pockets (Fig. 4.4). The extraction to the side (\hat{y}) surface (Fig. 4.5), on the other hand, has nontrivial features. We first note the somewhat surprising fact that even if the 3D topological insulator surface has negligibly small spin accumulation, $\eta \approx 0$, the spin accumulation extracted into the side pocket is nonnegligible (see corresponding figures in Appendix D). Furthermore, the extracted spin polarization changes sign when the gate voltage is tuned so that the charge carriers change from electrons to holes as can be seen from Figs. 4.5(b) and 4.5(c). We find that the geometry of the contact does not play a crucial role as it does for a 2DEG with Rashba spin-orbit coupling: In that case, wide contacts lead to reduced extraction [152] while for topological insulators wider contacts lead to enhanced extraction. In order to further study the spin-gate effect mentioned above, we plot the spin accumulation $\langle S_z \rangle$ averaged over the side pocket, as a function of the gate voltage applied to the side pocket, in Fig. 4.6. We find that the spin accumulation depends linearly on the gate voltage and the sign of polarization changes by switching the side pocket polarity from hole to electron type.

Finally, we show that one can locally control the polarization direction of different parts of side pockets by local gating. In Fig. 4.7, we apply the local gate profile where the electron puddles change into hole puddles within a region much smaller than the spin precession length ℓ_{sp} . We find that the spatial profile of the polarization of the extracted spin accumulation closely follows the local gate potential. Thus, we show that it is possible to electrically control local spin polarization within length scales much smaller than the spin precession length.

4.4 Conclusion

In conclusion, we focus on the current-induced spins at the surfaces of 3D topological insulators and show how to extract these spins into topologically trivial materials commonly used in electronic devices. We find that unlike the corresponding effect in 2DEGs with Rashba spin-orbit interaction the mixing of the electron and hole degrees of freedom at the topological insulator surface allows for additional methods for spin manipulation. In particular, we exposed a way to use electrical gate potentials to locally manipulate spins in regions smaller than the spin precession length. The extracted spins can then be detected via usual spintronics methods such as attaching a ferromagnetic lead or using magneto-optical Kerr microscopy. This opens up new possibilities for spin manipulation in spintronics devices.

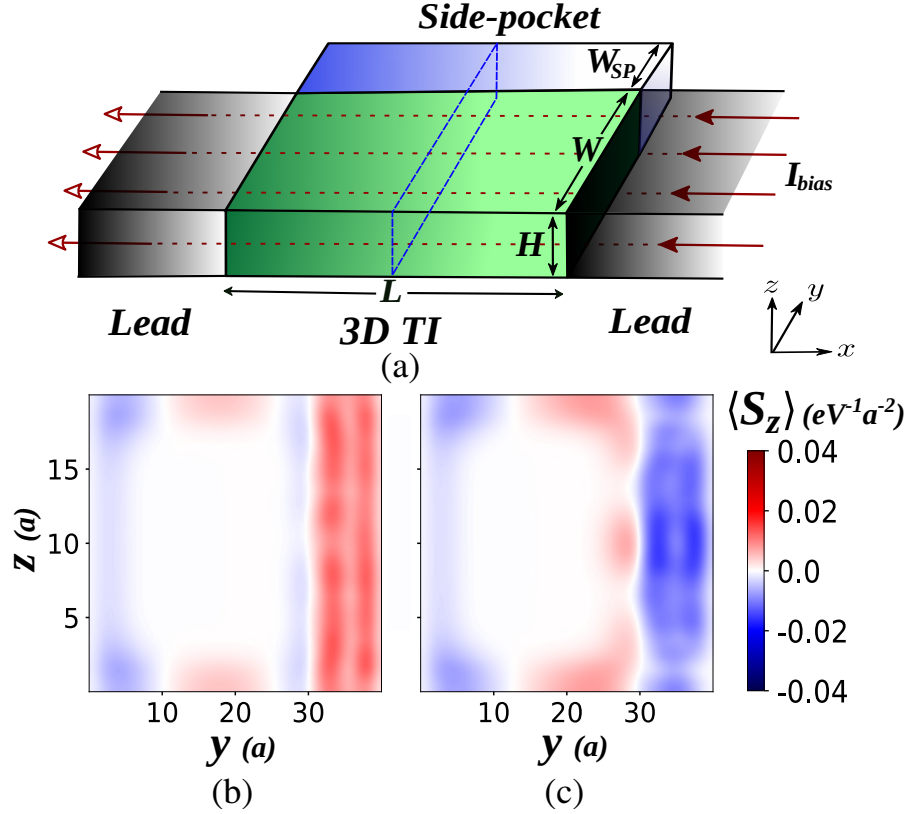


Figure 4.5 Current-induced spin polarization into a side pocket at the side surface. (a) Sketch of a side pocket attached to the side surface of the system shown in Fig. 4.2(a). (b), (c) Spatial profile of the averaged spin polarization $\langle S_z(y, z) \rangle$ (averaged over 1000 disorder configurations) along cross sections in the \hat{x} direction shown as a dashed blue rectangle in panel (a). In panels (b) and (c) the side pockets are doped to hole bands ($V_{\text{gate}} = -0.8\text{eV}$) and electron bands ($V_{\text{gate}} = 0.9\text{eV}$), respectively. Common parameters are $L = 30a$, $W = 30a$, $H = 20a$, $W_{SP} = 10a$, $U_0 = 0.5\text{eV}$, and $E_F = 0.15\text{eV}$, which is in the bulk gap.

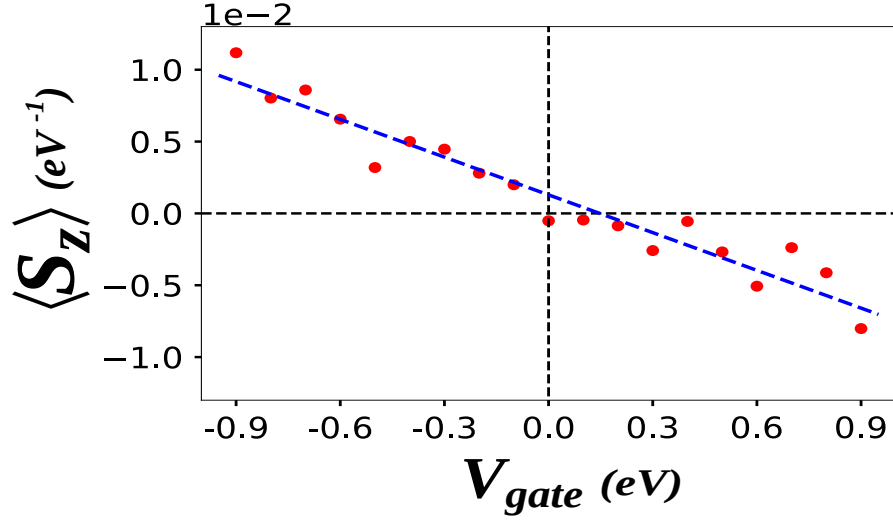


Figure 4.6 Gate dependence of side pocket spin polarization. $\langle S_z \rangle$ averaged over 1000 disordered configurations and doped side pocket sites is plotted vs gate potential. We consider the following parameters: $L = 30a$, $W = 30a$, $H = 20a$, $W_{SP} = 10a$, $U_0 = 0.5 \text{ eV}$, and $E_F = 0.15 \text{ eV}$, which is in the bulk gap. The blue line is the best fitted line.

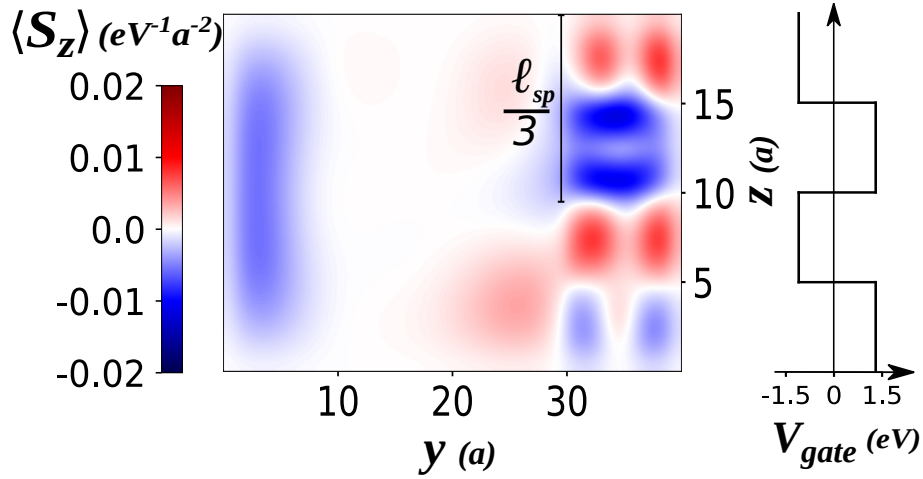


Figure 4.7 Spatial profile of the averaged spin polarization $\langle S_z(y, z) \rangle$ (averaged over 1000 disorder configurations) along cross sections in the \hat{x} direction for the system shown in Fig. 4.5(a). The side pocket is alternatively doped to electron bands ($V_{\text{gate}} = 1.3 \text{ eV}$) and hole bands ($V_{\text{gate}} = -1.1 \text{ eV}$). The side pocket is divided into four parts in the \hat{z} direction and the spatial profile is averaged over \hat{x} planes. Spin precession length in the \hat{z} direction, $\ell_{sp} \simeq 32a$ (considering $B_1 = B_2$). Other parameters used are $W_{SP} = 10a$, $L = 30a$, $W = 30a$, $H = 20a$, $U_0 = 0.7 \text{ eV}$, and $E_F = 0.15 \text{ eV}$, which is in the bulk gap.

5. HYPERFINE INTERACTION FOR THREE-DIMENSIONAL TOPOLOGICAL INSULATORS IN THE BISMUTH-SELENIDE FAMILY

In this chapter, we obtain effective expressions for the hyperfine interactions in 3D topological insulator materials belonging to the Bi_2Se_3 family within the effective model that was introduced in Refs. [155–158]. We also derive analytic expressions for the surface states corresponding to different faces of a Bi-based topological insulator with semi-infinite geometry. We utilize our results to explore how the hyperfine interactions differ for different surface states. We investigate transitions between and within surface states of any plane of a 3D topological insulator and discuss possible elastic backscattering spin-flip and forward scattering processes induced by the hyperfine interactions.

5.1 Introduction

Over the past decade, there has been a rising interest in electrically manipulating spin in nonmagnetic materials, e.g., paramagnetic metals and semiconductors with spin-orbit coupling, in parallel to the prevailing utilization of ferromagnets in the spintronics field. As we saw in previous chapters of this thesis, novel materials like topological insulators with spin-orbit coupling are good alternative materials for spintronics applications. 3D or 2D topological insulators host surface or edge states located in the bulk gap. Protection of time-reversal symmetry implies that topological surface or edge states are robust in topological insulators and against perturbations preserving time-reversal symmetry, such as nonmagnetic impurities. In 2D the situation is even more drastic, due to the time-reversal symmetry and spin-orbit coupling in topological insulators, the gapless surface (edge) states are spin-polarized helical 2D Dirac fermions (counterpropagating 1D helical pairs) at Fermi energy lies in the bulk gap, where backscattering, elastic scattering between paired modes, is forbidden since there is no available state for the reversed direction of propagation with similar spin polarization. All these features also lead to current-induced spin accumulation phenomenon in topological insulators studied

in the previous chapter, which has been observed experimentally [77, 83–88, 178]. From an application perspective, spin polarization obtained this way needs to be long-lasting and controllable for devices such as spin battery and spin memory. Nuclear spin and/or magnetic impurities violate time-reversal symmetry in topological insulators and lead to backscattering, which can be observed as a deviation from perfect quantized conductance. Thus, nuclear spin and/or magnetic impurities reduce electron spin-coherence time, becoming an obstacle in quantum computing devices. Nevertheless, there are recent proposals of potential applications that use such impurities in spintronics, such as a rechargeable spin battery [94] and memory resource [179].

Hyperfine interactions between the electron and nuclear spins have been studied in the context of nanostructures [180, 181], semiconductors [182, 183], quantum dots [184–192], spin blockade regime of quantum dots [193–197], quantum wells [198–200], 1D systems [201, 202], 2DEGs [203, 204], and at the edge of 2DEGs [205–207] as well as 2D topological insulators [208, 209]. Although hyperfine interactions are often weak, it plays an essential role in physical phenomena such as the electron or hole spin decoherence processes and allows manipulation of electron or hole spin with nuclear spins and vice versa. The isotropic hyperfine interaction called contact hyperfine interaction involves electrons in *s*-like orbital states, and is important while studying the conduction band of semiconductors, 2DEGs, or quantum dots (electron spin). The anisotropic hyperfine interaction and nuclear-orbital interaction are dominant in *p*-like orbital states, and are important for the valence band of semiconductors and the hole spin of quantum dots. Since surface/edge states of topological insulators is a quantum superposition of both electron and hole states, it is important to consider all the types of hyperfine interactions. This is the reason Lunde and Platero consider all aforementioned hyperfine interactions for a 2D topological insulator (HgTe quantum wire) within the BHZ model [75] including both *s*- and *p*-like orbitals [209]. We follow their approach to find hyperfine interactions in 3D topological insulators, particularly the Bi₂Se₃ family, within the effective band model.

This chapter is organized as follows: In Sec. 5.2 and Sec. 5.3, we outline the various types of hyperfine interactions and the effective band model for the Bi₂Se₃ family, respectively. Then we present the hyperfine interactions within this model which includes not only dominant *p*-like states but also *s*-like states in Sec. 5.4. Next, in Sec. 5.5 we derive the total hyperfine interactions for a Bi-based topological insulator slab as well as surface states of different planes of a 3D topological insulator with zero in-plane momentum. We conclude in Sec. 5.6.

5.2 Hyperfine Interactions

The interaction of an electron with a nucleus is described by the Dirac Hamiltonian:

$$H = \boldsymbol{\alpha} \cdot \boldsymbol{\pi} + \beta mc^2 + qV, \quad (5.1)$$

where m and q are the electron mass and charge, respectively. Here, $\boldsymbol{\pi} = c(\mathbf{p} - q\mathbf{A})$ with c the speed of light and p the momentum. V and \mathbf{A} are the scalar and vector potentials of the electromagnetic field created by the nucleus. $\boldsymbol{\alpha}$ and β are the 4×4 Dirac matrices. Therefore, one can obtain the terms including the coupling of electron and nucleus through decoupling electron and positron spinors and utilizing Foldy–Wouthuysen transformation to find the well-known relativistic corrections to the Pauli Hamiltonian [210, 211]:

$$H_{\text{ihf}} = \frac{q^2 \hbar}{4m^2 c^2} (\mathbf{E} \times \mathbf{A}) \cdot \boldsymbol{\sigma}, \quad (5.2)$$

$$H_{\text{ahf}} = -\frac{q \hbar}{2m} (\nabla \times \mathbf{A}) \cdot \boldsymbol{\sigma}, \quad (5.3)$$

$$H_{\text{ang}} = -\frac{q}{m} \mathbf{A} \cdot \mathbf{p}. \quad (5.4)$$

These terms represent the coupling of the charge and magnetic moment of nuclei (giving rise to \mathbf{E} and \mathbf{A}) and the spin, $\boldsymbol{\sigma}$, and momentum, \mathbf{p} of electron. The first two are referred as isotropic and anisotropic hyperfine interaction, respectively, and the last one corresponds to the coupling of electron orbital angular momentum and the nuclear spin. It is customary to rewrite Eqs. (5.2)-(5.4) in the form of effective Hamiltonians [209, 210, 212] in the same order as follows,

$$h_{1,n} = \gamma_1 \mathbf{S} \cdot \mathbf{I}_n \delta(\mathbf{r}_n), \quad (5.5)$$

$$h_{2,n} = \gamma_2 r_n^{-3} (3(\mathbf{e}_n \cdot \mathbf{S})(\mathbf{e}_n \cdot \mathbf{I}_n) - \mathbf{S} \cdot \mathbf{I}_n), \quad (5.6)$$

$$h_{3,n} = \gamma_2 r_n^{-3} \mathbf{L}_n \cdot \mathbf{I}_n. \quad (5.7)$$

Here, \mathbf{I}_n (\mathbf{S}) is the nuclear (electron) spin operator, and \mathbf{L}_n is the orbital momentum operator of the electron. $\mathbf{r}_n = \mathbf{r} - \mathbf{R}_n$ is the vector pointing from the n th nucleus to the electron, $r_n \equiv |\mathbf{r}_n|$, $\mathbf{e}_n \equiv \mathbf{r}_n/r_n$. For definition of the prefactors γ_i for $i = 1, 2, 3$, see Appendix H. The first term is known as "Fermi contact interaction" and its contribution is non-vanishing when the electron spin density is finite at the nucleus position (only s -orbital has this property among all orbitals). The second term is a dipole-dipole-like interaction (the anisotropic hyperfine interaction corresponding to p -orbitals). The last term corresponds to the interaction between nuclear spin and orbital angular momentum of the electron (and similar to the previous term, it

is relevant for p -orbitals).

In order to find the hyperfine interaction matrix elements, we follow Lunde and Platero's approach and assumptions [209], see Appendix G. They have found hyperfine interactions for HgTe within BHZ model [75] for states consisting only the p -like band as well as states consisting the mixtures of the s - and p -like bands. In this thesis, we obtain hyperfine interactions for Bi₂Se₃ family materials the band model of which includes only the p -like states. We will also consider s -orbitals because the Fermi contact interaction arising from s -orbitals is the strongest one among all hyperfine interactions [189], and even a small amount of s -mixing will have an important effect.

5.3 The Band Model of Bi-based Topological Insulators

The 3D effective Hamiltonian capturing the basic low-energy properties of Bi₂Se₃ family materials was considered in the previous chapter, Eq. (4.20). The dominant p -orbital states with angular momentum $m_j = \pm 1/2$ and parity $P = \pm 1$ are close to the Fermi energy [155]. These states are mixture of p_z and p_{\pm} orbitals due to the spin-orbit coupling. The $P = \pm 1$ hybridized states correspond to states from the Bi and Se atoms (for more details see Appendix F). Hence, the effective Hamiltonian is given in the basis below, expressed in terms of $|\text{Bi}(\text{Se})_p, m_l, m_s\rangle$:

$$|\text{Bi}_p, \frac{1}{2}\rangle = u_1 |\text{Bi}_p, 1, -\frac{1}{2}\rangle + v_1 |\text{Bi}_p, 0, \frac{1}{2}\rangle, \quad (5.8)$$

$$|\text{Se}_p, \frac{1}{2}\rangle = u_2 |\text{Se}_p, 1, -\frac{1}{2}\rangle + v_2 |\text{Se}_p, 0, \frac{1}{2}\rangle, \quad (5.9)$$

$$|\text{Bi}_p, -\frac{1}{2}\rangle = u_1 |\text{Bi}_p, -1, \frac{1}{2}\rangle + v_1 |\text{Bi}_p, 0, -\frac{1}{2}\rangle, \quad (5.10)$$

$$|\text{Se}_p, -\frac{1}{2}\rangle = u_2 |\text{Se}_p, -1, \frac{1}{2}\rangle + v_2 |\text{Se}_p, 0, -\frac{1}{2}\rangle, \quad (5.11)$$

where u_i and v_i include all the information about the spin-orbit coupling. We also define the real space basis functions for a Bi-based topological insulator:

$$\varphi_{\mathbf{k}, \text{Bi}_p \pm \frac{1}{2}}(\mathbf{r}) = \sqrt{\frac{v_a}{V}} e^{i\mathbf{k}\cdot\mathbf{r}} w_{\text{Bi}_p, \pm \frac{1}{2}}(\mathbf{r}), \quad (5.12)$$

$$\varphi_{\mathbf{k}, \text{Se}_p \pm \frac{1}{2}}(\mathbf{r}) = \sqrt{\frac{v_a}{V}} e^{i\mathbf{k}\cdot\mathbf{r}} w_{\text{Se}_p, \pm \frac{1}{2}}(\mathbf{r}), \quad (5.13)$$

where $\mathbf{r} = (x, y, z)$, $w_{\text{Bi}(\text{Se})_p, m_j}(\mathbf{r}) = \langle \mathbf{r} | \text{Bi}(\text{Se})_p, m_j \rangle$ is the real space lattice periodic functions at $\mathbf{k} = 0$, v_a is the unit cell volume, and V is the volume of the system.

We simplify the calculation of matrix elements interaction by approximating the lattice periodic functions via using a linear combination of atomic orbitals (LCAO) approach [189, 213, 214], see Appendix G.1 for more details.

5.4 Hyperfine Interactions within Bismuth-based Topological Insulator Band Model

In this section, we present hyperfine interactions within Bi-based 3D topological insulator band model. As we mention above, we obtain these interactions by generalizing Lunde and Platero's approach [209]. As it is already mentioned, the Fermi contact $H_{\text{HF},1}$ is zero for p -orbitals while matrix elements of $H_{\text{HF},i}$ for $i = 2, 3$ vanish for s -like states because of their spherical symmetry. In Bi_2Se_3 , the states close to the Fermi energy are p -like orbitals so $H_{\text{HF},2}$ and $H_{\text{HF},3}$ are hyperfine interaction with more contributions. But, we will also take into account the possibility of s -orbital-mixing. The s -mixing is nonnegligible because the Fermi contact interaction is the strongest one among all hyperfine interactions [189], so, even the smallest mixing is important. Based on numerical results [215], the contribution to the wavefunctions is about 10%, which is also confirmed by experimental findings [216].

Since the hyperfine interactions are local in space and depend on the nuclei locations, we focus on wavefunction around the nucleus. We sum over only lattice points with a nonzero nuclear spin to find the hyperfine interactions

$$H_{\text{HF}} = H_{\text{HF},1} + H_{\text{HF},2} + H_{\text{HF},3} = \sum_n h_{1,n} + \sum_n h_{2,n} + \sum_n h_{3,n}. \quad (5.14)$$

While most Bi nuclei have nonzero nuclear spin, other atoms in 3D topological insulator Bi_2Se_3 family, the simplest members of which are Bi_2Se_3 , Bi_2Te_3 , and Sb_2Te_3 , may have zero nuclear spin as well. For instance, the natural abundances of stable nuclei with a nonzero spin in the materials mentioned above are approximately [181]

$$\begin{aligned} 100\% \text{ for } ^{209}\text{Bi} \text{ (spin-9/2)}, & \quad 8\% \text{ for } ^{77}\text{Se} \text{ (spin-1/2)}, \\ 1\% \text{ for } ^{123}\text{Te} \text{ (spin-1/2)}, & \quad 7\% \text{ for } ^{125}\text{Te} \text{ (spin-1/2)}, \\ 57\% \text{ for } ^{121}\text{Sb} \text{ (spin-5/2)}, & \quad 43\% \text{ for } ^{123}\text{Sb} \text{ (spin-7/2)}. \end{aligned} \quad (5.15)$$

We find the effective hyperfine interactions by projecting onto the relevant bonds,

for which we need the following matrix elements

$$\mathcal{H}_{\text{HF},i} = \sum_{\mathbf{k},\mathbf{k}'} \sum_{v,v'} \sum_{\tau,\tau'=\pm\frac{1}{2}} \langle \varphi_{\mathbf{k},v,\tau} | H_{\text{HF},i} | \varphi_{\mathbf{k}',v',\tau'} \rangle c_{\mathbf{k},v,\tau}^\dagger c_{\mathbf{k}',v',\tau'} \quad (5.16)$$

for $i = 1, 2, 3$ corresponds to different hyperfine interactions. Here $\varphi_{\mathbf{k},v\pm 1/2}(\mathbf{r})$ is the real basis function (Eqs. (5.12) and (5.13) with $v(v') = \text{Bi}_p, \text{Se}_p$).

5.4.1 The hyperfine interaction for p -like states

The dominant orbitals of the Bi_2Se_3 are p -orbitals; therefore, the dipole-dipole like interaction and electron orbital momentum-nuclear spin coupling are the prominent hyperfine interactions. We obtain the contribution of $\mathcal{H}_{\text{HF},2}$ interaction to the p -like states in the band model of Bi-based 3D topological insulators by projecting dipole-dipole hyperfine interaction, Eq. (5.6), onto the real basis functions, Eqs. (5.12) and (5.13) (see Appendix G for more details). The projected Hamiltonian becomes:

$$\mathcal{H}_{\text{HF},2} = \sum_n \sum_{\mathbf{k},\mathbf{k}'} \frac{e^{i(\mathbf{k}'-\mathbf{k})\cdot\mathcal{R}_n}}{V} \mathbf{c}_{\mathbf{k}}^\dagger \tilde{H}_{\text{HF},2} \mathbf{c}_{\mathbf{k}'}, \quad (5.17)$$

where $\mathbf{c}_{\mathbf{k}}^\dagger = (c_{\mathbf{k},E+}^\dagger, c_{\mathbf{k},H+}^\dagger, c_{\mathbf{k},E-}^\dagger, c_{\mathbf{k},H-}^\dagger)$, $\mathcal{R}_n \equiv (\mathcal{X}_n, \mathcal{Y}_n, \mathcal{Z}_n)$ is the Bravais lattice vector for n th unit cell with a nonzero nuclear spin, and

$$\tilde{H}_{\text{HF},2} = \frac{1}{5\hbar} \begin{pmatrix} A_{11}I_{z,n} & A_{12}I_{-,n} \\ A_{12}I_{+,n} & -A_{11}I_{z,n} \end{pmatrix}, \quad (5.18)$$

where

$$A_{11} = \begin{pmatrix} A_1 A_{p,j_n}^{++} & A_2 A_{p,j_n}^{+-} \\ A_2 A_{p,j_n}^{-+} & A_3 A_{p,j_n}^{--} \end{pmatrix}, \quad A_{12} = \begin{pmatrix} A_4 A_{p,j_n}^{++} & A_5 A_{p,j_n}^{+-} \\ A_5 A_{p,j_n}^{-+} & A_6 A_{p,j_n}^{--} \end{pmatrix}.$$

We note that the definitions of the real parameters A_i as well as A_{p,j_n} are given in Appendix H.

The contribution of the $\mathcal{H}_{\text{HF},3}$ interaction to the p -like states in this model is found again by projecting the hyperfine interaction between nuclear spin and orbital angular momentum field of the electron, Eq. (5.7), onto the real basis functions, Eqs. (5.12) and (5.13) (see Appendix G). We obtain

$$\mathcal{H}_{\text{HF},3} = \sum_n \sum_{\mathbf{k},\mathbf{k}'} \frac{e^{i(\mathbf{k}'-\mathbf{k})\cdot\mathcal{R}_n}}{V} \mathbf{c}_{\mathbf{k}}^\dagger \tilde{H}_{\text{HF},3} \mathbf{c}_{\mathbf{k}'}, \quad (5.19)$$

where

$$\tilde{H}_{\text{HF},3} = \frac{1}{\hbar} \begin{pmatrix} B_{11}I_{z,n} & B_{12}I_{-,n} \\ B_{12}I_{+,n} & -B_{11}I_{z,n} \end{pmatrix} \quad (5.20)$$

with

$$B_{11} = \begin{pmatrix} B_1 A_{p,j_n}^{++} & B_2 A_{p,j_n}^{+-} \\ B_2 A_{p,j_n}^{-+} & B_3 A_{p,j_n}^{--} \end{pmatrix}, \quad B_{12} = \begin{pmatrix} B_4 A_{p,j_n}^{++} & B_5 A_{p,j_n}^{+-} \\ B_5 A_{p,j_n}^{-+} & B_6 A_{p,j_n}^{--} \end{pmatrix}.$$

The detailed definitions of B_i terms can be found in Appendix H.

5.4.2 Taking into account s -like states' contributions to the band model

The matrix elements that include contact hyperfine interaction are zero for p -orbitals due to the fact that p -orbitals vanish at the atomic center where the nuclei reside, and the effect of contact hyperfine interaction is only on the nuclei. Therefore, one gets zero matrix elements for $H_{\text{HF},1}$ if s -orbitals are neglected. As stated earlier, the states close to the Fermi energy are predominantly p -like states in the Bi_2Se_3 family, hence, the contact hyperfine interaction is zero. On the other hand, it is claimed numerically [215] and experimentally [216] that the s -orbital contribution to the bands is around 10%, so that the hyperfine coupling constants could be one order of magnitude higher [189]. Therefore, we study the contact hyperfine interaction in this section. In order to consider the effect of s -orbitals, we write the lattice periodic functions as a mixture of s - and p -orbitals

$$w_{\text{Bi},\pm\frac{1}{2}}(\mathbf{r}) = u_{\text{Bi}_s,\pm\frac{1}{2}}(\mathbf{r}) + u_{\text{Bi}_p,\pm\frac{1}{2}}(\mathbf{r}), \quad (5.21)$$

$$w_{\text{Se},\pm\frac{1}{2}}(\mathbf{r}) = u_{\text{Se}_s,\pm\frac{1}{2}}(\mathbf{r}) + u_{\text{Se}_p,\pm\frac{1}{2}}(\mathbf{r}), \quad (5.22)$$

where u 's with lower indices $\text{Bi}(\text{Se})_s$ and $\text{Bi}(\text{Se})_p$ are the lattice periodic functions corresponding to the s - and p -orbitals of $\text{Bi}(\text{Se})$ atom, respectively, and they can be approximated similar to Eqs. (G.1) and (G.2) via using the LCAO method, see Appendix H.

The contact hyperfine interaction in the Bi-based 3D topological insulator band model basis is again found via projecting Fermi contact interaction, Eq. (5.5) onto the real basis functions. This procedure produces

$$\mathcal{H}_{\text{HF},1} = \sum_n \sum_{\mathbf{k}, \mathbf{k}'} \frac{e^{i(\mathbf{k}' - \mathbf{k}) \cdot \mathcal{R}_n}}{V} \mathbf{c}_{\mathbf{k}}^\dagger \tilde{H}_{\text{HF},1} \mathbf{c}_{\mathbf{k}'}, \quad (5.23)$$

where

$$\tilde{H}_{\text{HF},1} = \frac{1}{2\hbar} \begin{pmatrix} AI_{z,n} & AI_{-,n} \\ AI_{+,n} & -AI_{z,n} \end{pmatrix} \quad (5.24)$$

with

$$A = \begin{pmatrix} A_{s,j_n}^{++} & A_{s,j_n}^{+-} \\ A_{s,j_n}^{-+} & A_{s,j_n}^{--} \end{pmatrix}.$$

Again the precise definitions of the s -like hyperfine couplings, A_{s,j_n} , are given in Appendix H.

5.5 Hyperfine Interactions for Surface States

In this section, we shift our focus from the bulk to the surface and obtain the expressions for hyperfine interactions for surface states of 3D Bi₂Se₃ family topological insulator slabs with semi-infinite boundary condition (BC). The total hyperfine interaction according to the previous sections gives rise to

$$\mathcal{H}_{\text{HF}} = \sum_{i=1}^3 \mathcal{H}_{\text{HF},i} = \sum_n \sum_{\mathbf{k}, \mathbf{k}'} \frac{e^{i(\mathbf{k}' - \mathbf{k}) \cdot \mathcal{R}_n}}{V} \mathbf{c}_{\mathbf{k}}^\dagger \tilde{H}_{\text{HF}} \mathbf{c}_{\mathbf{k}'}, \quad (5.25)$$

where

$$\tilde{H}_{\text{HF}} = \frac{1}{\hbar} \begin{pmatrix} C_{11}I_{z,n} & C_{12}I_{-,n} \\ C_{12}I_{+,n} & -C_{11}I_{z,n} \end{pmatrix} \quad (5.26)$$

with

$$C_{11} = \frac{A}{2} + \frac{A_{11}}{5} + B_{11}, \quad C_{12} = \frac{A}{2} + \frac{A_{12}}{5} + B_{12}.$$

Using this, we can find the hyperfine interaction for any nanostructure in a Bi₂Se₃ family quantum wires through projecting the total hyperfine interaction, Eq. (5.25), onto the associated envelope wavefunctions of the quantum wires, $\Phi(\mathcal{R}_{n\perp})$,

$$\mathcal{H}_{\text{HF}} = \sum_n \sum_{\nu, \nu'} [\Phi_\nu(\mathcal{R}_{n\perp})]^\dagger \tilde{H}_{\text{HF}} \Phi_{\nu'}(\mathcal{R}_{n\perp}) c_\nu^\dagger c_{\nu'}, \quad (5.27)$$

where the sum includes only the atomic sites n with a nonzero nuclear spin, and $\mathcal{R}_{n\perp}$ is the projected Bravais lattice vector for n th unit cell with a nonzero nuclear spin onto the surface of the extended directions.

We now consider a 3D topological insulator slab where the lattice periodic basis functions include plane wave envelope functions in two directions, x_i and x_j , and an envelope function in the other direction, x_k . Hence, the real basis functions are as

follows

$$\varphi_{\mathbf{k},\text{BiP},\pm\frac{1}{2}}(\mathbf{r}) = \sqrt{\frac{v_a}{L_{x_i}L_{x_j}}} e^{i(k_{x_i}x_i+k_{x_j}x_j)} f_{\text{BiP}}(x_k) w_{\text{BiP},\pm\frac{1}{2}}(\mathbf{r}), \quad (5.28)$$

$$\varphi_{\mathbf{k},\text{SeP},\pm\frac{1}{2}}(\mathbf{r}) = \sqrt{\frac{v_a}{L_{x_i}L_{x_j}}} e^{i(k_{x_i}x_i+k_{x_j}x_j)} f_{\text{SeP}}(x_k) w_{\text{SeP},\pm\frac{1}{2}}(\mathbf{r}), \quad (5.29)$$

where $f(x_k)$ are the transverse envelope functions in the x_k direction perpendicular to the extended directions of the slab, $(x_i, x_j, x_k) = (x, y, z)$, and L_{x_i} are the lengths of the slab in the x_i -direction. Since the hyperfine interactions act on the atomic length scale, the gradually changing envelope functions become multiplicative factors in the hyperfine interactions that leads to the position dependent hyperfine interaction couplings, see Appendix H.

For finding the effective hyperfine interaction for surface states of 3D topological insulator slab, we utilize the full wavefunction of a pair of surface states obtained in the rest of this section by considering semi-infinite BC. For example, for the $\hat{\mathbf{z}}$ surface, we have

$$\Psi^\varsigma(x, y, z) = \frac{1}{\sqrt{L_x L_y}} e^{i(k_x x + k_y y)} \psi_{k_\parallel}^{\hat{\mathbf{z}}, \varsigma}(z) \quad \text{for } \varsigma = \text{u, d} \quad (5.30)$$

with $\psi_{k_\parallel}^{\hat{\mathbf{z}}, \varsigma}(z)$ is a spinor which decays as a function of z as z moves away from the boundary. Here, $\varsigma = \text{u, d}$ corresponds to two states, eigenvectors of Hamiltonian (4.20), resulting from surface problems. For $\hat{\mathbf{z}}$ surface, "u" and "d" can be regarded as spin-up and down feature of spinors due to the basis states of Hamiltonian (4.20) whereas this interpretation is not valid for $\hat{\mathbf{x}}$ and $\hat{\mathbf{y}}$ surfaces since surface states include an admixture of electron and hole with opposite spins on these surfaces, as we show later in this chapter. Therefore, we can find hyperfine interaction by plugging surface states into Eq. (5.27). Corresponding calculations for finding surface states of different surfaces of a 3D topological insulator through considering semi-infinite BC are discussed in Appendix B.

5.5.1 $\hat{\mathbf{z}}$ surface states

We insert surface states of $\hat{\mathbf{z}}$ planes found via considering semi-infinite BC, into the hyperfine interaction formula (5.27) to find total hyperfine interaction for $\hat{\mathbf{z}}$ surfaces of a 3D topological insulator. The surface states with zero in-plane momentum for

semi-infinite BC are as follows,

$$\psi_{k_{\parallel}=0}^{\pm\hat{\mathbf{z}},\text{u}}(z) = \begin{bmatrix} \text{sgn}(B_1 A_1) \sqrt{|1+\xi|} \\ \mp i \sqrt{|1-\xi|} \\ 0 \\ 0 \end{bmatrix} g_{\pm}(z), \quad \psi_{k_{\parallel}=0}^{\pm\hat{\mathbf{z}},\text{d}}(z) = \begin{bmatrix} 0 \\ 0 \\ \text{sgn}(B_1 A_1) \sqrt{|1+\xi|} \\ \pm i \sqrt{|1-\xi|} \end{bmatrix} g_{\pm}(z), \quad (5.31)$$

where \pm corresponds to $\psi(z = \mp\infty) = 0$, $\xi = D_1/B_1$, and

$$g_{\pm}(z) = \frac{N}{\sqrt{2}} (e^{\pm\lambda_1 z} - e^{\pm\lambda_2 z}) \quad (5.32)$$

with

$$N = \left(\frac{1}{2\lambda_1} + \frac{1}{2\lambda_2} - \frac{2}{\lambda_1 + \lambda_2} \right)^{-\frac{1}{2}} \text{ for } \lambda_1, \lambda_2 \in \mathbb{R}, \quad (5.33)$$

$$N = \left(\frac{1}{a} - \frac{a}{a^2 + b^2} \right)^{-\frac{1}{2}} \text{ for } \lambda_1 = \lambda_2^* = a + ib, \quad (5.34)$$

which are normalization constants for different possibilities of having surface states according to the solutions for λ . Hence, the total hyperfine interaction for $\hat{\mathbf{z}}$ surface states for a single nuclear spin is

$$\mathcal{H}_{\text{HF},\pm\hat{\mathbf{z}}} = \frac{\Lambda_{\pm}(\mathcal{Z}) e^{i(\mathbf{k}' - \mathbf{k}) \cdot \mathcal{R}_{\perp}}}{L_x L_y \hbar} \left[\mathcal{B}_1 \sigma_z I_z + \mathcal{B}_{2,\pm} \sigma_+ I_- + \text{h.c.} \right], \quad (5.35)$$

where σ_z is the Pauli matrix in the pseudospin space (bands at the surface), σ_0 denotes 2×2 identity matrix, and $\sigma_+ = \begin{pmatrix} 0 & 1 \\ 0 & 0 \end{pmatrix}$, $\Lambda_{\pm}(\mathcal{Z}) = |g_{\pm}(\mathcal{Z})|^2$, and the other parameters are

$$\begin{aligned} \mathcal{B}_1 &= |1 + \xi| \mathcal{A}_1^{++} + |1 - \xi| \mathcal{A}_1^{--}, \\ \mathcal{B}_{2,\pm} &= |1 + \xi| \mathcal{A}_2^{++} - |1 - \xi| \mathcal{A}_2^{--} \pm 2i \text{sgn}(B_1 A_1) \sqrt{1 - \xi^2} \text{Re}(\mathcal{A}_2^{+-}), \end{aligned}$$

where the hyperfine couplings are defined in Appendix H. *Lambda* is the position dependency part of the hyperfine interaction couplings and it is also real because it corresponds to the decay function of surface states. We also used the fact that \mathcal{A}_i 's are real. The hyperfine interaction for the $\hat{\mathbf{z}}$ surface demonstrates the transition between $\Psi^{\text{u}}(x, y, z)$ and $\Psi^{\text{d}}(x, y, z)$ only if the nuclear spin state changes. This means that nuclei behave as impurities and breaks time-reversal symmetry from the standpoint of the electron. However, time-reversal symmetry in the system that includes electrons and nuclei is conserved since the total angular momentum (including electron spin and nuclear spin) is conserved.

5.5.2 \hat{y} surface states

We now obtain the effective hyperfine interaction for \hat{y} surfaces of a 3D topological insulator as we did for the \hat{z} surfaces. We substitute surface states of \hat{y} planes, found through considering semi-infinite BC, into the hyperfine interaction formula (5.27). For the \hat{y} surface, the full wavefunction can be written as follows,

$$\Psi^\varsigma(x, y, z) = \frac{1}{\sqrt{L_x L_z}} e^{i(k_x x + k_z z)} \psi_{k_x, z}^{\hat{y}, \varsigma}(y), \quad \text{for } \varsigma = \text{u, d} \quad (5.36)$$

where $\psi_{k_x, z}^{\hat{y}, \varsigma}(y)$ is a spinor which includes a y -dependent decay function. The \hat{y} surface states with zero in-plane momentum for semi-infinite BC are

$$\psi_{k_x, k_z=0}^{\pm \hat{y}, \text{u}}(y) = \begin{bmatrix} \text{sgn}(B_2 A_2) \sqrt{|1 + \eta|} \\ 0 \\ 0 \\ \pm \sqrt{|1 - \eta|} \end{bmatrix} g_\pm(y), \quad (5.37)$$

$$\psi_{k_x, k_z=0}^{\pm \hat{y}, \text{d}}(y) = \begin{bmatrix} 0 \\ \mp \sqrt{|1 - \eta|} \\ \text{sgn}(B_2 A_2) \sqrt{|1 + \eta|} \\ 0 \end{bmatrix} g_\pm(y),$$

where \pm corresponds to considering $\psi(y = \mp \infty) = 0$, $\eta = D_2/B_2$, and

$$g_\pm k_{x,z}(y) = \frac{N}{\sqrt{2}} (e^{\pm \lambda_1 y} - e^{\pm \lambda_2 y}). \quad (5.38)$$

As we can see, superscripts "u" and "d" do not belong to spin blocks anymore. Hence, the total hyperfine interaction for \hat{y} surface states for one nuclear spin is

$$\mathcal{H}_{\text{HF}, \pm \hat{y}} = \frac{\Lambda_\pm(\mathcal{Y}) e^{i(\mathbf{k}' - \mathbf{k}) \cdot \mathcal{R}_\perp}}{L_x L_z \hbar} \left[\sigma_z \left(\mathcal{B}_3 I_z \pm 2\kappa \text{Re}(\mathcal{A}_2^{+-}) I_x \right) + \sigma_+ \left(\mathcal{B}_4 I_- - \mathcal{B}_5 I_+ \mp 2\kappa \text{Re}(\mathcal{A}_1^{+-}) I_z \right) + \text{h.c.} \right], \quad (5.39)$$

where $\Lambda_\pm(\mathcal{Y}) = |g_\pm(\mathcal{Y})|^2$, $\kappa = \text{sgn}(B_2 A_2) \sqrt{|1 - \eta|^2}$, and the other parameters are

$$\mathcal{B}_3 = |1 + \eta| \mathcal{A}_1^{++} - |1 - \eta| \mathcal{A}_1^{--}, \quad \mathcal{B}_4 = |1 + \eta| \mathcal{A}_2^{++}, \quad \mathcal{B}_5 = |1 - \eta| \mathcal{A}_2^{--}.$$

In contrast to hyperfine interaction found for \hat{z} surface states, Eq. (5.35), the hyperfine interaction for \hat{y} surface states include an additional term, $I_{x,n}$, which couples the transition within a surface state to both spins. Furthermore, the transition

between surface states contains not only terms involving I_{\pm} , similar to $\hat{\mathbf{z}}$ surface hyperfine interaction, but also I_z terms. These differences stem from the fact that surface states of $\hat{\mathbf{y}}$ planes are an admixture of electron and hole with opposite spins, while surface states of $\hat{\mathbf{z}}$ planes are a mixture of electron and hole with the same spin.

5.5.3 $\hat{\mathbf{x}}$ surface states

Although it is very similar to the $\hat{\mathbf{y}}$ surface, for completeness, we obtain the total hyperfine interactions for $\hat{\mathbf{x}}$ surface states of a 3D topological insulator with inserting surface states of $\hat{\mathbf{x}}$ planes, calculated through considering semi-infinite BC, into eq. (5.27). Accordingly, we have the full wavefunction as follows,

$$\Psi^{\varsigma}(x, y, z) = \frac{1}{\sqrt{L_y L_z}} e^{i(k_y y + k_z z)} \psi_{k_y, z}^{\hat{\mathbf{x}}, \varsigma}(x) \quad \text{for } \varsigma = \text{u, d} \quad (5.40)$$

with the spinor $\psi_{k_y, z}^{\hat{\mathbf{x}}, \varsigma}(x)$ including a x -dependent decay function. The $\hat{\mathbf{x}}$ surface states with zero in-plane momentum for semi-infinite BC are,

$$\psi_{k_y, k_z=0}^{\pm \hat{\mathbf{x}}, \text{u}}(x) = \begin{bmatrix} \text{sgn}(B_2 A_2) \sqrt{|1 + \eta|} \\ 0 \\ 0 \\ \mp i \sqrt{|1 - \eta|} \end{bmatrix} g_{\pm}(x), \quad (5.41)$$

$$\psi_{k_y, k_z=0}^{\pm \hat{\mathbf{x}}, \text{d}}(x) = \begin{bmatrix} 0 \\ \mp i \sqrt{|1 - \eta|} \\ \text{sgn}(B_2 A_2) \sqrt{|1 + \eta|} \\ 0 \end{bmatrix} g_{\pm}(x),$$

where \pm corresponds to considering $\psi(x = \mp \infty) = 0$ and

$$g_{\pm}(x) = \frac{N}{\sqrt{2}} (e^{\pm \lambda_1 x} - e^{\pm \lambda_2 x}). \quad (5.42)$$

The effective hyperfine interaction for $\hat{\mathbf{x}}$ surface states for one nuclear spin is

$$\begin{aligned} \mathcal{H}_{\text{HF}, \pm \hat{\mathbf{x}}} = \frac{\Lambda_{\pm}(\mathcal{X}) e^{i(\mathbf{k}' - \mathbf{k}) \cdot \mathcal{R}_{\perp}}}{L_y L_z \hbar} & \left[\sigma_z \left(\mathcal{B}_3 I_z \mp 2\kappa \text{Re}(\mathcal{A}_2^{+-}) I_y \right) \right. \\ & \left. + \sigma_{\pm} \left(\mathcal{B}_4 I_{-} + \mathcal{B}_5 I_{+} \mp 2i\kappa \text{Re}(\mathcal{A}_1^{+-}) I_z \right) + \text{h.c.} \right], \end{aligned} \quad (5.43)$$

where $\Lambda_{\pm}(\mathcal{X}) = |g_{\pm}(\mathcal{X})|^2$. The $\hat{\mathbf{x}}$ surface states hyperfine interaction is similar to the $\hat{\mathbf{y}}$ surface states hyperfine interaction except for some coefficients, originating from the imaginary unit i in the components of $\hat{\mathbf{x}}$ spinors as well as I_x is replaced by I_y .

5.6 Conclusion

In conclusion, we derived analytic expressions for the effective hyperfine interactions for low-lying quasiparticle states of a 3D topological insulator belonging to the Bi_2Se_3 family. We obtained zero in-plane momentum surface states of the edges of a 3D topological insulator slab with considering semi-infinite BC in the specific direction. We also obtained hyperfine interactions for different surface states of a Bi-based topological insulator. The upshot of our results is general enough to be applied for any material in the Bi_2Se_3 family. The findings of this study indicate that hyperfine interactions imply elastic backscattering spin-flip process through transitions between surface states corresponding to any edges of a Bi-based topological insulator. Furthermore, we have obtained extra terms regarding coupling the transition within surface states of $\hat{\mathbf{x}}$ or $\hat{\mathbf{y}}$ planes with nuclear spins while there is not such a coupling for $\hat{\mathbf{z}}$ surface states. These terms will affect the nuclear spin polarization and its associated Overhauser effective magnetic field complicatedly. In our view, these results constitute an excellent initial step toward understanding hyperfine interactions for anisotropic 3D topological insulator materials, and we hope that further tests will confirm our findings, which leads to spintronics applications.

6. GIANT MAGNETORELECTRIC EFFECT IN WEYL SEMIMETALS

In this chapter, we consider a mechanism in magnetic Weyl semimetals that allows blocking or transmitting carriers through manipulating Weyl nodes' chiralities. Chirality in this context specifies whether the spins are essentially locked parallel or antiparallel to the momentum of the charge carriers, see Eq. (2.3) for a precise definition. This effect is analogous to the GMR effect which is mostly observed in junctions including Ferromagnetic layers and conductors, and electrical resistance can be tuned by changing the magnetization of ferromagnetic layers. In the ferromagnetic case, the conductance of layers with antiparallel magnetization will be lower than layers with parallel magnetization. Similarly, Weyl layers with opposite chiralities show lower conductance than layers with identical chiralities. Hence, we show below that manipulating Weyl points' chiralities can adjust the electrical resistance and lead to a new GMR device for nanoelectronics and valleytronics applications. In order to investigate the generality and robustness of this effect against the presence of nonmagnetic and magnetic impurities in our systems, we study both clean and disordered junctions that include different Weyl semimetals in terms of symmetries.

6.1 Introduction

Weyl semimetals, 3D analogs of graphene, are gapless materials, where the bulk bands cross at nodes, called Weyl points. Near the crossing, the energy depends linearly on the momentum. There are an even number of Weyl points with opposite chiralities in the Brillouin zone due to the fermion doubling theorem. Pairs of Weyl points are connected through the surface states called the Fermi arcs [32]. Interesting quantum transport properties such as extremely large magnetoresistance (MR) [217, 218], unprecedented carrier mobilities [217, 218], and negative MR induced by the chiral anomaly [219, 220] in these materials have attracted extensive attention from the condensed matter and material science communities. Moreover, Weyl fermions are robust in the presence of impurity scattering due to the inter-

play of spin conservation with the chiral Weyl points. Moreover, each chiral Weyl node behaves as a monopole in momentum space so that this magnetic property can be utilized in the spintronics and valleytronics fields. To realize these theoretically predicted properties and introduce prevalent devices, further experimental research need to be conducted in Weyl semimetals.

The electrical resistance change in the presence of a magnetic field is an exceptional characteristic of different materials, which becomes a fundamental diagnostic tool in condensed matter and can be utilized in electronics and spintronics devices such as magnetic sensors and magnetic storage devices. The most practical tool is made of thin films composed of magnetic elements that exhibit giant negative MR [221] due to the suppression of the spin scattering in a magnetic field. Metals, semiconductors, and semimetals show positive MR [222]. Large MR was also reported in 3D Dirac semimetal and Weyl semimetal materials recently [223, 224]. Hence, many studies have been recently conducted to investigate MR in various Weyl semimetal materials for fundamental physics and applicable devices.

In this chapter, we focus on the manipulation of Weyl cones' chiralities in junctions made of Weyl semimetals, and show how this leads to an analogue of the GMR effect. We start with an effective model of Weyl semimetals commonly adopted in the literature [225–227]. We then focus on a layered geometry (sketched in Fig. 6.4) and demonstrate how chirality blocks or transmits current. Our considered junctions are based on Weyl semimetals in which either time-reversal symmetry or inversion symmetry is broken. Next, we show that the current can be blocked by reversing the Weyl points' chiralities. We finally study to what extent this effect is robust against the random nonmagnetic and magnetic disorder.

The outline of this chapter is as follows. In Sec. 6.2, we outline the effective Hamiltonian of a Weyl semimetal. In Sec. 6.3, we present our analytical and numerical results for different junctions based on Weyl semimetal in which inversion symmetry or time-reversal symmetry is preserved. We then show that the GMR effect can be seen in our considered systems. In Sec. 6.3.3, we demonstrate how nonmagnetic or magnetic impurities influence the conductance of Weyl semimetal junctions. We close with concluding remarks in Sec. 6.4.

6.2 Method and Model

The bulk gap closes when a 3D topological insulator undergoes a phase transition to the trivial insulator or vice versa. At this critical transition point the system becomes a 3D massless Dirac semimetal which have been experimentally observed

in $\text{TlBi}(\text{S}_{1-x}\text{Se}_x)_2$ crystals [228] and $(\text{Bi}_{1-x}\text{In}_x)_2\text{Se}_2$ [229] films. Here the low energy spectrum satisfies the 3D form of Dirac equation. The Dirac points are doubly degenerate due to the presence of time-reversal and inversion symmetries and can be split into a pair of Weyl points by breaking one of the symmetries. The Weyl points can be separated from each other either in momentum or in energy. Symmetry determines the location and the number of Weyl points in the momentum space. To see this, note that the time-reversal symmetry maps \mathbf{k} to $-\mathbf{k}$ and reverses Berry curvature, $\boldsymbol{\Omega}(-\mathbf{k}) = -\boldsymbol{\Omega}(\mathbf{k})$ so the chirality of Weyl point does not change. Therefore, in Weyl semimetals with preserved time-reversal symmetry (and with broken inversion symmetry), there should be at least four Weyl points to fulfill the fermion doubling theorem. Inversion symmetry keeps the k -space "magnetic field", $\boldsymbol{\Omega}(-\mathbf{k}) = \boldsymbol{\Omega}(\mathbf{k})$ so the chirality of a Weyl point at \mathbf{k} is reversed under inversion symmetry and mapped to $-\mathbf{k}$. Hence, Weyl semimetals with broken time-reversal symmetry can host two Weyl cones.

To have better intuition of constructing a Weyl semimetal with the smallest number of Dirac points, which is two, in a real space, Burkov and Balents [28] have proposed the simplest realistic model that is composed of stacking the topological and trivial insulators, such as Bi_2Se_3 , alternatively. A Zeeman field breaks time-reversal symmetry by adding magnetic impurities, see Fig. 6.1. Producing ultrathin films of Bi_2Se_3 in experiments [230–232] paves the way of fabricating the proposed multilayer heterostructure. Their model is written based on the two different short-range tunneling parameters corresponding to tunneling between surface states within the same layer and neighboring layers. Regardless of magnetism, the multilayer heterostructure can be in a topological or trivial phase based on the strength of tunneling parameters. By inducing magnetization to the topological insulator layers through doping magnetic impurities, the system shows the Weyl semimetal phase determined by tuning tunneling parameters. The analogous structure has also been proposed by breaking the inversion symmetry to reach a Weyl semimetal material [233]. Furthermore, another model for a Weyl semimetal realization has also been suggested based on the stacking 1D primitives according to the Aubry-Andre-Harper model [234]. Weyl Semimetal phase can also be reached at the transition point between topological and trivial insulators where bulk gap closes [28, 34, 233, 235, 236].

Different forms of Hamiltonians that feature low energy physics consisting of Weyl semimetals that can easily be transformed into each other by applying a unitary transformation. We start with the Weyl semimetal Hamiltonian introduced by Vazifeh and Franz [225] who have started with the standard 3D topological insulator model for the Bi_2Se_3 family. However, the Hamiltonian is presented in a basis that is different from what we used in the previous chapters for 3D topological insulators.

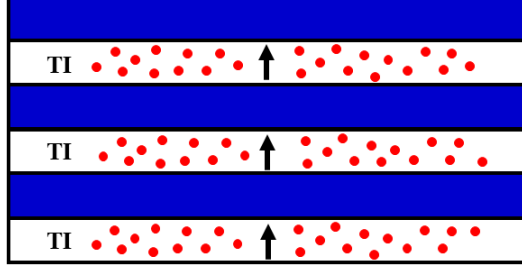


Figure 6.1 The multilayer structure includes topological insulator layers and trivial insulator spacers (shown as blue layers). The induced magnetization direction due to introducing magnetic impurities (shown as red circles) is shown by the arrow in each topological insulator layer.

The momentum space Hamiltonian of Vazifeh and Franz is,

$$H_0(\mathbf{k}) = 2\lambda\tau_z(\sigma_x\sin(k_y) - \sigma_y\sin(k_x)) + 2\lambda_z\tau_y\sin(k_z) + \tau_x M_{\mathbf{k}} \quad (6.1)$$

with $\boldsymbol{\tau}$ and $\boldsymbol{\sigma}$ the Pauli matrices in the orbital and spin space, respectively, and $M_{\mathbf{k}} = \epsilon - 2t\sum_{\alpha}\cos(k_{\alpha})$. This model describes a strong topological insulator when λ and λ_z have positive values in the range of $(2t, 6t)$. We can easily transform this Hamiltonian to the form of the effective Hamiltonian introduced by Zhang et al. [155] for 3D topological insulators through a unitary transformation. Hence, $H_{3\text{DTI}} = UH_{\text{Vazifeh}}U^{\dagger}$ with

$$U = \exp(-i[\frac{\pi}{2}\tau_z\sigma_0 - \frac{\pi}{4}\tau_y\sigma_0 + \frac{\pi}{4}\tau_x\sigma_z - \frac{3\pi}{4}\tau_0\sigma_z]). \quad (6.2)$$

As a result, the Hamiltonian is in the following basis, $(|E \uparrow\rangle, |H \uparrow\rangle, |E \downarrow\rangle, |H \downarrow\rangle)$ which enables us to use associated spin operators [158] for adding appropriate magnetic impurities later. The Hamiltonian in Eq. (6.1) includes the transition point of a topological insulator phase and a trivial insulator phase, 3D Dirac point, where gap closes at $k = 0$ when $\epsilon = 6t$. Furthermore, in order to explore the Weyl phases, Vazifeh and Franz introduce the following perturbation [225];

$$H_1(\mathbf{k}) = b_0\tau_y\sigma_z + \mathbf{b} \cdot (-\tau_x\sigma_x, \tau_x\sigma_y, \sigma_z). \quad (6.3)$$

Here nonzero b_0 breaks the inversion symmetry but preserves the time-reversal symmetry while \mathbf{b} breaks the time-reversal symmetry, keeping the inversion symmetry intact. In the case $\mathbf{b} = b_z\hat{z}$, there is a pair of Weyl points located at $\mathbf{k} = \pm \frac{b_z}{2\lambda_z}\hat{z}$ in momentum space. The band structure of $H = H_0$ and $H = H_0 + H_1$ for the mentioned cases are displayed in Fig. 6.2.

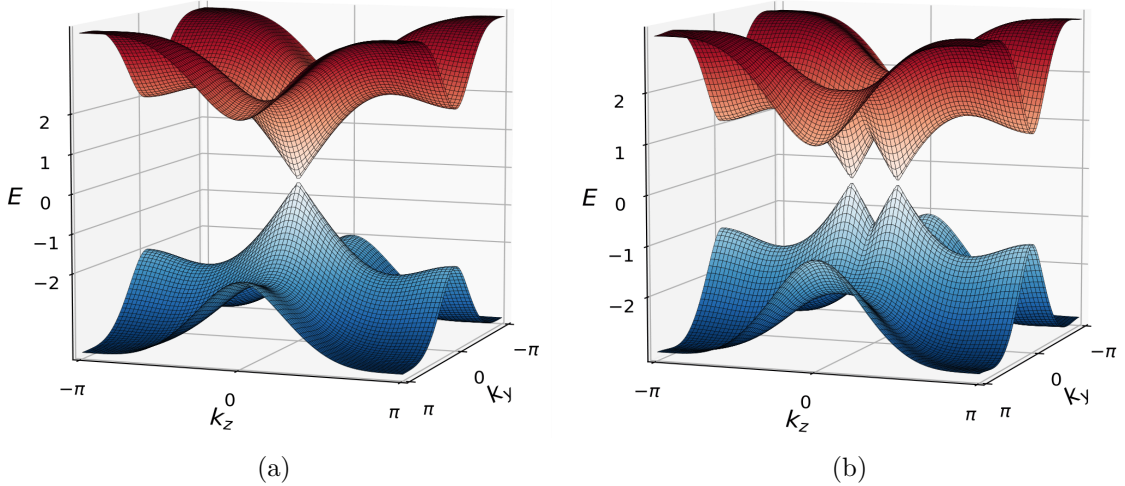


Figure 6.2 The band structure of the Weyl semimetal lattice model. (a) Doubly degenerate 3D Dirac point when $H_1 = 0$. (b) Momentum-shifted Weyl point for $b_z = 1.0$ and $b_0 = 0$. In both panels, $\epsilon = 6t$, $\lambda = \lambda_z = 1.0$, and $t = 0.5$.

In our numerical study, we utilize the KWANT toolbox [124] and use the tight-binding representation of the Hamiltonian given in Eqs. (6.1) and (6.3), and focus on a 3D wire attached to two semi-infinite leads. We use different structures for the scattering region, such as a uniform Weyl semimetal or a heterostructure of Weyl semimetals, where the Weyl cones are separated differently in the momentum space. We numerically evaluate the charge conductance according to Eq. (3.7) for an infinitesimal bias (linear response regime) at a specific energy, E_F , originating from one of the leads, depending on the sign of the bias.

6.3 Weyl Semimetal Junction, GMR Effect

The GMR effect is usually observed in systems including a nonmagnetic layer (usually a conductor) between alternating ferromagnetic layers. There is a substantial change in the electrical resistance depending on the magnetization direction of adjoining ferromagnetic layers. The resistance for parallel alignment of the magnetization of the ferromagnetic layers is much lower than that of the antiparallel alignment. The GMR effect has many applications for reading, writing, and storing data in the field of electronics and spintronics, such as magnetic field sensors and magnetoresistive random-access memory [237].

Weyl cones with different chiralities behave like magnetic monopoles (sink or source) in the momentum space. When a left-handed Weyl fermion is incident on a region allowing right-handed Weyl fermions then the transmission will be diminished compared to the case where both fermions are left-handed. Since the chirality in

magnetic Weyl semimetals are controlled by the magnetization, this situation is very similar to the GMR effect. Therefore, we expect that Weyl semimetal junctions with different chiralities directions of "magnetization" might be utilized as a chirality-valve analogous to GMR devices. we explore this idea in the next section.

6.3.1 Junctions with broken time-reversal symmetry

Consider a slab junction including Weyl semimetals with broken time-reversal symmetry where two Weyl points are located at $\mathbf{k} = \pm \frac{b_z}{2\lambda_z} \hat{z}$. Hence, we take only the b_z term to be nonzero in Eq. (6.3). We want to find the transmission and reflection coefficients for two junctions shown in Fig. 6.3 through the wavefunction matching method. For the region I in both junctions, we consider a Weyl semimetal the Weyl cones of which are separated in the \hat{z} direction in momentum space. The region II of the first junction, shown in Fig. 6.3(a), is identical to the region I, i.e., chiralities of the Weyl points remain unchanged. By contrast, the chiralities of the Weyl points in region II of the junction shown in Fig. 6.3(b) are reversed with respect to the chirality of Weyl points in the region I. The magnitude of the b_z term is considered the same in all regions. In order to match the wavefunction at $x = 0$, the interface between two regions, we need to find eigenvalues and corresponding eigenvectors of $H = H_0 + H_1$.

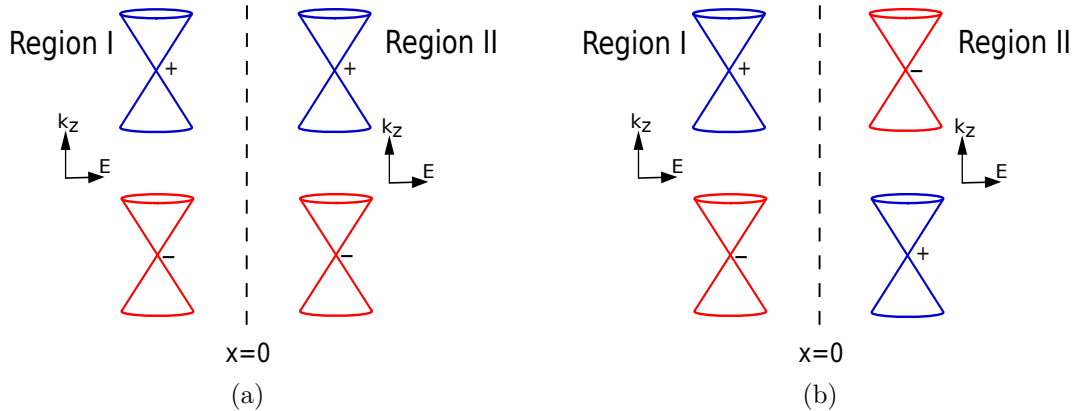


Figure 6.3 Junction of Weyl semimetals slabs with a pair of Weyl cone shifted in the \hat{z} direction in momentum space with (a) the identical chiralities and (b) reversed chiralities at the location of Weyl points. Weyl cones of different colors represent opposite chiralities.

In case $\mathbf{b} = |b_z| \hat{z}$ and $b_0 = 0$, we find four energies which are $E_{\pm}^{\text{low}} = \pm \sqrt{A \mp 2\sqrt{B}}$ and $E_{\pm}^{\text{high}} = \pm \sqrt{A \pm 2\sqrt{B}}$, where $A = M_{\mathbf{k}}^2 + b_z^2 + 4\lambda^2(\sin^2(k_x) + \sin^2(k_y)) + 4\lambda_z^2 \sin^2(k_z)$ and $B = b_z^2(M_{\mathbf{k}}^2 + 4\lambda_z^2 \sin^2(k_z))$. We focus on low energy region since the two low-

energy bands E_{\pm}^{low} form a pair of Weyl cones and their spinors are simplified as follows

$$\phi_{\pm}^{\text{low}}(\mathbf{k}, E_{\pm}) = \frac{1}{N_{\pm}} \begin{bmatrix} \frac{i\sqrt{B}(|b_z|^2 - \sqrt{B} + |b_z|E_{\pm})}{2\lambda|b_z|^2(\sin(k_x) + i\sin(k_y))(M_{\mathbf{k}} + 2i\lambda_z \sin(k_z))} \\ \frac{\sqrt{B}}{|b_z|(M_{\mathbf{k}} + 2i\lambda_z \sin(k_z))} \\ \frac{-i(|b_z|^2 - \sqrt{B} + |b_z|E_{\pm})}{2\lambda|b_z|(\sin(k_x) + i\sin(k_y))} \\ 1 \end{bmatrix}, \quad (6.4)$$

where N_{\pm} are normalization constants. In the case $\mathbf{b} = -|b_z|\hat{z}$, we find identical energies since energy dispersion does not change and just the chirality of Weyl points are reversed. Even though, terms $|b_z|$ in spinors should be replaced to $-|b_z|$.

Case $b_z = |b_z|$ in region II:

For simplicity we consider the energy dispersion along the k_z -axis and assume $k_x = k_y = 0$ in Hamiltonian, hence, low energies are $E_{\pm} = \pm|b_z| \mp |F(k_z)|$ with $F(k_z) = \sqrt{(\epsilon - t(2 + \cos(k_z))) + 2i\lambda_z \sin(k_z)}$ and corresponding spinors are as follows

$$u(k_z) = \frac{1}{\sqrt{2}} \begin{bmatrix} \frac{E_+ - |b_z|}{F(k_z)} \\ 0 \\ 1 \\ 0 \end{bmatrix}, \quad v(k'_z) = \frac{1}{\sqrt{2}} \begin{bmatrix} 0 \\ \frac{E_- + |b_z|}{F_{k'_z}} \\ 0 \\ 1 \end{bmatrix}. \quad (6.5)$$

The fixed energy, E_F , intersects low energy bands at four points, $\pm k_z$ and $\pm k'_z$, where $E_F = E_+(\pm k_z) = E_-(\pm k'_z)$. The incoming mode is a linear superposition of both cones, but we consider incident electron near the cone located at $\mathbf{k} = (0, 0, b_z/2\lambda_z)$ since the other Weyl cone at opposite \mathbf{k} in the Brillouin zone gives the same contribution to the conductance. Based on these considerations, we can write the wavefunctions of both regions in the form of

$$\Psi_{\text{I}} = \frac{1}{\sqrt{2}} \left(u(k_z)e^{i(k_x x + k_y y + k_z z)} + v(k'_z)e^{i(k_x x + k_y y + k'_z z)} \right) + r_1 u(k_z)e^{i(-k_x x + k_y y + k_z z)} + r_1 v(k'_z)e^{i(-k_x x + k_y y + k'_z z)}, \quad (6.6)$$

$$\Psi_{\text{II}} = t_1 u(k_z)e^{i(k_x x + k_y y + k_z z)} + t_2 v(k'_z)e^{i(k_x x + k_y y + k'_z z)}. \quad (6.7)$$

The wavefunction must be continuous at the interface $x = 0$, thus the transmission and reflection coefficients are found as $r_1 = r_2 = 0$, and $t_1 = t_2 = 1/\sqrt{2}$. The con-

ductance is obtained via $G = \frac{e^2}{h} T$ where $T = \text{Tr}[t^\dagger t]$, in the limit of infinitesimal voltage bias and zero temperature, and is 1 when considering only these bands. In addition, there is not any reflection obviously because both regions are identical and any incoming modes propagate to the other part.

Case $b_z = -|b_z|$ in region II:

The bands at low energies are identical to the previous section, but spinors are different, which is key to our results. Now the spinors are given by

$$u(k_z) = \frac{1}{\sqrt{2}} \begin{bmatrix} 0 \\ \frac{E_+ - |b_z|}{F(k_z)} \\ 0 \\ 1 \end{bmatrix}, \quad v(k_z) = \frac{1}{\sqrt{2}} \begin{bmatrix} \frac{E_- + |b_z|}{F(k_z)} \\ 0 \\ 1 \\ 0 \end{bmatrix}. \quad (6.8)$$

Therefore, while Ψ_I is unchanged, Ψ_{II} changes to the form based on the spinors given above. By applying the matching BCs at the interface, we obtain $r_1 = r_2 = -1/\sqrt{2}$ and $t_1 = t_2 = 0$. This implies that the current is switched to zero if we switch the chirality in region II with respect to the region I under constant bias. Hence, manipulation Weyl points' chiralities in heterostructures results in a magnetoelectric effect.

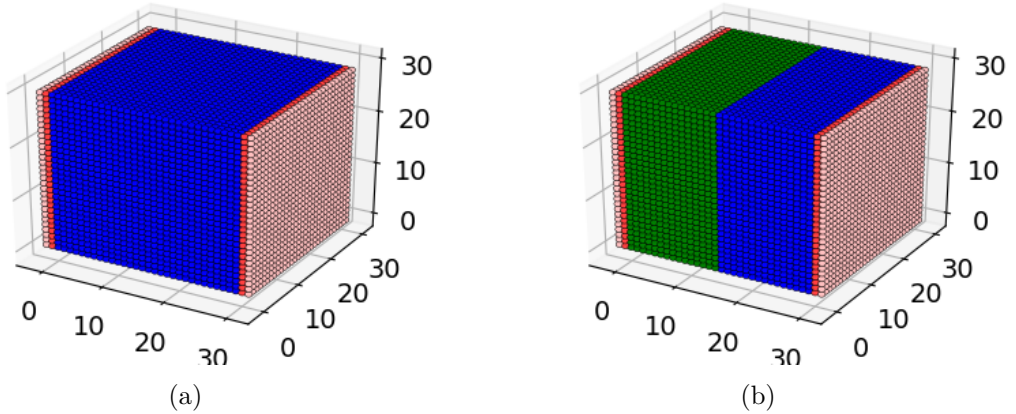


Figure 6.4 (a) Schematic representation of a Weyl semimetal nanowire with a pair of Weyl cone shifted in the \hat{z} direction in momentum space. (b) Schematic representation of a Weyl semimetal junction with a pair of Weyl cone shifted in the \hat{z} direction in momentum space and have opposite chirality at the location of Dirac points as shown in Fig. 6.3(b).

We also numerically find the charge conductance for Weyl junctions attached to

two leads along the $\hat{\mathbf{x}}$ direction as shown in Fig. 6.4. The Weyl semimetals considered in all parts of nanowire shown in Fig. 6.4(a) have Weyl cones separated along the $\hat{\mathbf{z}}$ direction in momentum space. This situation analogous to the case of two ferromagnetic layers with the same direction of magnetization. On the other hand, in Fig. 6.4(b) we sketch a junction including Weyl semimetals with a pair of Weyl cones shifted again in the $\hat{\mathbf{z}}$ direction in momentum space, but this time with opposite chiralities. In other words, b_z terms in their Hamiltonians have opposite signs, and each Weyl semimetal have a pair of Weyl cones shifted in momentum space with opposite chirality (similar to the same sign case) but the location of the cones have switched. The different sign of b_z terms are depicted as different colors in Fig. 6.4(b). Also, the left lead is similar to the left part of the junction in the scattering region, and the right lead has the same properties as the right side of the system. Two semi-infinite Weyl semimetals with opposite chirality of separated cones mimic two ferromagnetic layers with antiparallel alignment.

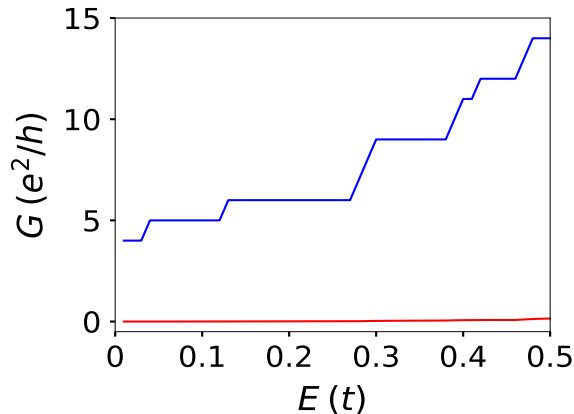


Figure 6.5 Conductance of the systems shown in Fig. 6.4. The blue line shows the conductance of a Weyl semimetal nanowire the cones of which are separated in the $\hat{\mathbf{z}}$ direction, see Fig. 6.4(a). The red line illustrates the conductance of a Weyl junction where the sign of b_z terms are opposite in different regions, see Fig. 6.4(b). Parameters used are $\epsilon = 6t$, $\lambda = \lambda_z = 1.0$, $t = 0.5$, $b_z = |1.0|$, and $b_0 = b_x = b_y = 0$.

In Fig. 6.5 the numerical results for the conductance of a junction of two Weyl semimetals with opposite sign of b_z as well as a Weyl semimetal nanowire the b_z term of which has the same sign is plotted. We see that the junction with the same chirality structure behaves as a conductor with quantized conductance, the junction with opposite chirality essentially have zero conductance. Our numerical simulations are therefore in good agreement with our analytical expectations.

We also perform numerical simulations for the conductance of Weyl junctions where the Weyl cones are separated in the k_x and the k_y directions, centered at opposite points in $\pm\mathbf{k} = (\pm b_x/2\lambda, 0, 0)$ and $\pm\mathbf{k} = (0, \pm b_y/2\lambda, 0)$, respectively. The numerical

results plotted in Fig. 6.6 shows that the conductance for junctions with nonzero b_y term is identical to the previous case since the system is isotropic in the yz -plane. On the other hand, the conductance for the system where Weyl cones are separated in the k_x direction is less compared to the systems where Weyl cones are separated in the k_y or k_z direction. The reason is that only one of the cones contribute to the conductance since the current is in the \hat{x} direction. In summary, a junction including Weyl semimetals in which the magnetization can be tuned to be parallel and antiparallel (i.e., their Weyl cones have different chiralities) might be applied as a GMR device.

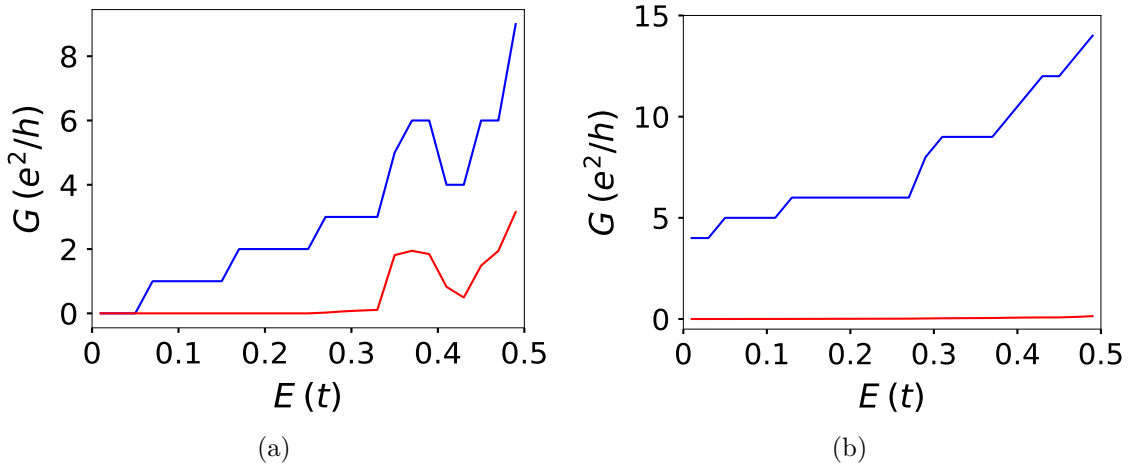


Figure 6.6 Conductance of the systems the Weyl cones of which are separated in the (a) k_x direction, where $b_x = |1.0|$ and $b_y = 0.0$; and (b) k_y direction, where $b_x = 0.0$ and $b_y = |1.0|$. In both figures, the blue (red) lines show the conductance of a Weyl semimetal nanowire junction where the chiralities of Weyl points in region II are identical (opposite) with respect to the chiralities of Weyl points in region I. Common parameters are $\epsilon = 6t$, $\lambda = \lambda_z = 1.0$, $t = 0.5$, and $b_0 = b_z = 0$.

6.3.2 Junctions with broken inversion symmetry

Weyl semimetal materials where time-reversal symmetry is broken are more accessible compared to Weyl semimetal materials with broken inversion symmetry. Because introducing magnetic impurities or applying magnetic field for breaking time-reversal symmetry make materials potentially tunable. Besides, the electronic band structure is also simpler in time-reversal symmetry broken Weyl materials. A Weyl semimetal phase can also be reached at the phase transition from a topological insulator to a trivial insulator by applying strain, hence with violating the inversion symmetry [34]. We note that, TaAs is intrinsically found to be a Weyl semimetal due to the lack of inversion symmetry, which splits degenerate spin bands [18]. In this section, we consider a Weyl semimetal with broken inversion symmetry and

intact time-reversal symmetry. This perturbation can be introduced as a spin-orbit interaction term, $\tau_y \sigma_z$, see the Hamiltonian (6.3) as a result of strain. As we said earlier, at least four (i.e., two pairs) of Weyl points are separated in energy, see Fig. 6.7(a).

We now focus on the conductance for Weyl junction nanowires with a lack of inversion symmetry and preserved time-reversal symmetry. Hence, we set $\mathbf{b} = 0$ and $b_0 \neq 0$ in the tight-binding form of Hamiltonian (6.3) for our numerical simulations. Again, in one system, the sign of b_0 term is considered identical in both regions, while in another junction, the sign of the broken inversion symmetry term is reversed, i.e., chiralities of two pairs of Weyl points are changed. Fig. 6.7(b) represents that the GMR effect can also be obtained by using broken inversion symmetry Weyl semimetals. This magnetoelectric effect is not as perfect as junctions based on Weyl semimetals with broken time-reversal symmetry discussed in the previous section. The reason is that there are four Weyl points shifted in energy, and the band structure is complicated due to spin splitting bands.

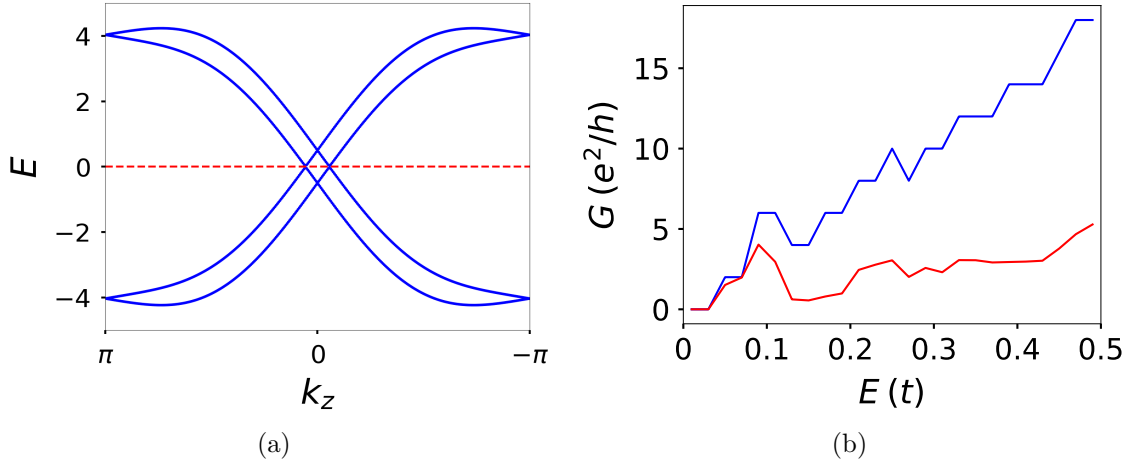


Figure 6.7 (a) The band structure of the broken inversion symmetry Weyl semimetal lattice model. (b) Conductance of the Weyl junction systems with broken inversion symmetry. The blue (red) line shows the conductance of a Weyl semimetal nanowire junction where the sign of b_0 term in region II is same (opposite) the b_0 term in region I. Common parameters are $\epsilon = 6t$, $\mathbf{b} = 0.0$, $|b_0| = 0.5$, $\lambda = \lambda_z = 1.0$, and $t = 0.5$.

6.3.3 Disordered systems

In this section, we numerically find conductance of different Weyl semimetals junctions in the presence of either nonmagnetic or magnetic impurities. For model nonmagnetic disorder by adding an on-site potential randomly chosen from a Gaussian distribution with strength U_0 to the tight-binding Hamiltonian of a Weyl semimetal (6.1) and (6.3). We find that the magnetoelectric effect in junctions

based on time-reversal symmetry broken Weyl semimetals is robust against disorder, see Fig. 6.8(a). On the other hand, there is an increase in the charge conductance for the broken inversion symmetry Weyl semimetal junctions with opposite chiralities of Weyl points, see Fig. 6.8(b), because there could be an interaction between energy-shifted Weyl cones in the presence of scalar disorder. Consequently, the magnetoelectric effect in our proposed junctions is intact in the presence of weak nonmagnetic disorder.

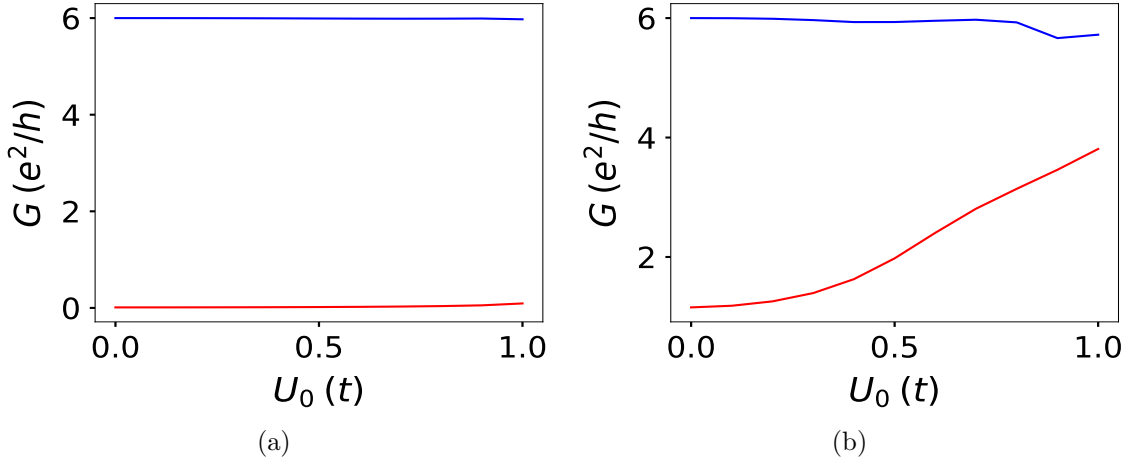


Figure 6.8 Conductance of the Weyl junction systems in the presence of nonmagnetic impurities at the fixed energy, $E_F = 0.2$. (a) The blue (red) line shows the conductance of a Weyl semimetal nanowire junction where the sign of b_z terms are same (opposite) in Hamiltonian of regions I and II, see Fig. 6.4(b). We set $|b_z| = 1.0$ and $b_0 = 0$. (b) The blue (red) lines show the conductance of a Weyl semimetal nanowire junction where the sign of b_0 terms are same (opposite) in the Hamiltonian of regions I and II. We set $|b_0| = 0.5$ and $b_z = 0$. Common parameters are $\epsilon = 6t$, $b_x = b_y = 0.0$, $\lambda = \lambda_z = 1.0$, $t = 0.5$, and U_0 is the on-site disorder strength.

To study the effect of a static magnetic impurity, we add $\mathbf{M} \cdot \sigma \tau_0$ term to the unitary transformed form of Hamiltonian Eq. (6.2). \mathbf{M} models the magnetization. In our simulations, we consider $\mathbf{M} = M_z \hat{z}$ which means that the magnetic disorder is polarized. In addition, we distribute magnetic disorder randomly on a few percentages of sites. We find that the GMR effect in broken time-reversal symmetry Weyl semimetal junction is intact in the presence of random magnetic impurities, see Fig. 6.9(a). Because magnetic impurities also break time-reversal symmetry, which was already broken in this junction. Introducing magnetic impurities does not significantly affect the conductance of junctions based on Weyl semimetals with broken inversion symmetry, see Fig. 6.9(b). When both time-reversal and inversion symmetries are violated, Weyl nodes are shifted in the opposite direction in energy and momentum space. Hence, there should not be any significant change in the conductance. Thus, introducing magnetic impurities with nonzero z -component of

the exchange field does not affect the chirality-valve effect discussed in this section.

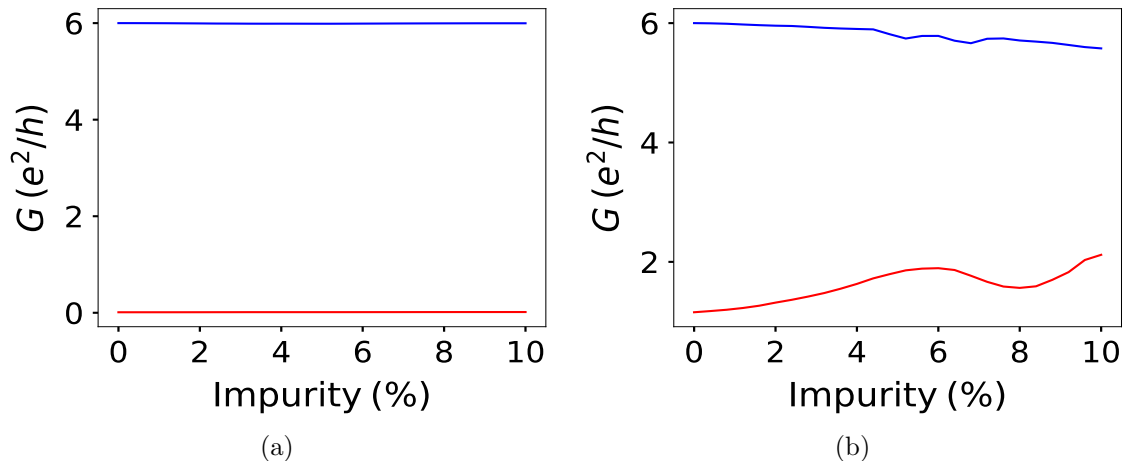


Figure 6.9 Conductance of the Weyl junction systems in the presence of magnetic impurities at the fixed energy, $E_F = 0.2$. (a) The blue (red) line shows the conductance of a Weyl semimetal nanowire junction where the sign of b_z terms are same (opposite) in Hamiltonian of regions I and II, see Fig. 6.4(b). We set $|b_z| = 1.0$ and $b_0 = 0$. (b) The blue (red) line shows the conductance of a Weyl semimetal nanowire junction where the sign of b_0 terms are same (opposite) in the Hamiltonian of regions I and II. We set $|b_0| = 0.5$ and $b_z = 0$. Common parameters are $\epsilon = 6t$, $b_x = b_y = 0.0$, $\lambda = \lambda_z = 1.0$, $t = 0.5$, and $M_z = 1.0$.

6.4 Conclusion

In conclusion, we find a chirality-valve effect in junctions based on Weyl semimetals with preserving either inversion symmetry or time-reversal symmetry. We show that current can be totally blocked by reversing Weyl points' chiralities in junctions based on time-reversal symmetry broken Weyl semimetals. We find that this effect also exists in Weyl semimetal junctions with broken inversion symmetry, but the effect is weaker as the conductance is not zero due to the presence of at least four Weyl points. We numerically find that the magnetoelectric effect in Weyl semimetal junctions is robust against weak nonmagnetic and magnetic impurities. This chirality blockade in Weyl semimetals opens up new possibilities for nanoelectronics devices.

7. CONCLUSION

In this thesis, we studied the quantum transport of internal quantum degrees of freedom in Dirac materials, in particular, graphene, topological insulators, and Weyl semimetals. Based on our findings, we proposed various spintronics and valleytronics applications.

In chapter 2, we gave a brief overview of Dirac materials properties and applications as a background in consideration of the subject matter of the thesis.

In chapter 3, we showed that graphene with enhanced spin-orbit coupling can be used as a spin generator. We demonstrated that dilute adatoms deposited on graphene induce novel spin-valley interactions. We then checked this effect with numerical tight-binding simulations and investigated how valley currents transform into spin currents by introducing adatoms on graphene. We found that the increase of deposited adatoms on graphene leads to an in-plane polarized spin current. We proposed a valley-spin converter device that can be utilized in spintronics and valleytronics fields.

In chapter 4, we focused on the Edelstein effect at the surfaces of a 3D topological insulator, Bi_2Se_3 , and investigated the extraction of the spin accumulation from topological insulator surfaces into topologically trivial materials. We found that admixture of electron and hole degrees of freedom at the topological insulator surface allows for additional methods for spin manipulation. We derived the spin-charge coupled dynamics formula at anisotropic topological insulator surfaces and obtained the dependence of the real spin density on the charge gradients due to the applied voltage bias. We numerically tested our formula via the tight-binding method, and we found that the analytical formulas well describe our numerical results for the Edelstein effect at topological insulator surfaces. We exposed a way to use electrical gate potentials to locally manipulate spins, especially at the edges of crystals that are not in the growth direction in regions smaller than the spin precession length. We proposed a new spin device based on topological insulator for spin manipulation in spintronics applications.

In chapter 5, We studied hyperfine interactions that include the contact hyperfine

interaction, the dipole-dipole-like hyperfine interaction, and the interaction between the nuclear spin and the electrons orbital for 3D topological insulators, particularly the Bi_2Se_3 family. We derived surface states of all surface planes for a 3D topological insulator slab that are general enough to be applied for any material in the Bi_2Se_3 family. We then found hyperfine interactions for all surface states of a 3D topological insulator. We demonstrated that hyperfine interactions imply elastic backscattering spin-flip process through transitions between surface states of any planes of a 3D topological insulator. We have also obtained intra-transition only in surface states of the edges of crystals that are not in the growth direction due to the admixture of electron- and hole-like states with different spins at the corresponding surfaces.

In chapter 6, we found a chirality-valve effect in junctions based on different Weyl semimetals. We analytically derived that junctions made of Weyl semimetals with broken time-reversal symmetry are ideal candidates for GMR devices. We have also found similar results via performing tight-binding simulations. We showed that chirality could be tuned to allow or block the current. We have also investigated this effect in our proposed systems with the presence of nonmagnetic and magnetic disorders. We found a new magnetoelectric effect due to the chirality of valley degree of freedom in Weyl semimetal materials and proposed a chirality-valve device to be used in nanoelectronics applications.

Bibliography

- [1] P. A. M. Dirac and R. H. Fowler, “The quantum theory of the electron,” *Proceedings of the Royal Society of London. Series A, Containing Papers of a Mathematical and Physical Character*, vol. 117, no. 778, pp. 610-624, 1928.
- [2] B. Thaller, “The Dirac equation,” *Springer Science and Business Media*, 2013.
- [3] A. Castro Neto, F. Guinea, N. M. Peres, K. S. Novoselov, and A. K. Geim, “The electronic properties of graphene,” *Reviews of modern physics*, vol. 81, no. 1, pp. 109-162, 2009.
- [4] K. S. Novoselov, A. K. Geim, S. V. Morozov, D. Jiang, M. I. Katsnelson, I. V. Grigorieva, S. V. Dubonos, and A. A. Firsov, “Two-dimensional gas of massless Dirac fermions in graphene,” *Nature*, vol. 438, no. 7065, pp. 197-200, 2005.
- [5] L. Brey and H. A. Fertig, “Electronic states of graphene nanoribbons studied with the Dirac equation,” *Physical Review B*, vol. 73, no. 23, p. 235411, 2006.
- [6] O. Vafek and A. Vishwanath, “Dirac fermions in solids: from high-Tc cuprates and graphene to topological insulators and Weyl semimetals,” *Annual Review of Condensed Matter Physics*, vol. 5, no. 1, pp. 83-112, 2014.
- [7] X.-L. Qi and S.-C. Zhang, “The quantum spin Hall effect and topological insulators,” *arXiv preprint arXiv:1001.1602*, 2010.
- [8] X.-L. Qi and S.-C. Zhang, “Topological insulators and superconductors,” *Reviews of Modern Physics*, vol. 83, no. 4, pp. 1057-1110, 2011.
- [9] J. E. Moore, “The birth of topological insulators,” *Nature*, vol. 464, no. 7286, pp. 194-198, 2010.
- [10] M. Z. Hasan and C. L. Kane, “Colloquium: topological insulators,” *Reviews of Modern Physics*, vol. 82, no. 4, pp. 3045-3067, 2010.
- [11] Z. Zeng, Z. Yin, X. Huang, H. Li, Q. He, G. Lu, F. Boey, and H. Zhang, “Single-layer semiconducting nanosheets: High-yield preparation and device fabrication,” *Angewandte Chemie International Edition*, vol. 50, no. 47, pp. 11093-11097, 2011.
- [12] M. Ezawa, “Spin valleytronics in silicene: Quantum spin Hall–quantum anomalous Hall insulators and single-valley semimetals,” *Physical Review B*, vol. 87, no. 15, p. 155415, 2013.

- [13] I. Crassee, R. Sankar, W.-L. Lee, A. Akrap, and M. Orlita, “3D Dirac semimetal Cd_3As_2 : A review of material properties,” *Physical Review Materials*, vol. 2, no. 12, p. 120302, 2018.
- [14] T. Wehling, A. M. Black-Schaffer, and A. V. Balatsky, “Dirac materials,” *Advances in Physics*, vol. 63, no. 1, pp. 1-76, 2014.
- [15] Q. D. Gibson, L. M. Schoop, L. Muechler, L. S. Xie, M. Hirschberger, N. P. Ong, R. Car, and R. J. Cava, “Three-dimensional Dirac semimetals: Design principles and predictions of new materials,” *Physical Review B*, vol. 91, no. 20, p. 205128, 2015.
- [16] S. A. Yang, “Dirac and Weyl materials: fundamental aspects and some spintronics applications,” *Spin*, vol. 6, no. 2, p. 1640003, World Scientific, 2016.
- [17] B. Yan and C. Felser, “Topological materials: Weyl semimetals,” *Annual Review of Condensed Matter Physics*, vol. 8, no. 1, pp. 337-354, 2017.
- [18] B. Q. Lv, H. M. Weng, B. B. Fu, X. P. Wang, H. Miao, J. Ma, P. Richard, X. C. Huang, L. X. Zhao, G. F. Chen, Z. Fang, X. Dai, T. Qian, and H. Ding, “Experimental discovery of Weyl semimetal TaAs,” *Physical Review X*, vol. 5, no. 3, p. 031013, 2015.
- [19] D. Xiao, W. Yao, and Q. Niu, “Valley-contrasting physics in graphene: Magnetic moment and topological transport,” *Physical Review Letters*, vol. 99, no. 23, p. 236809, 2007.
- [20] C.-C. Liu, W. Feng, and Y. Yao, “Quantum spin Hall effect in silicene and two-dimensional germanium,” *Physical Review Letters*, vol. 107, no. 7, p. 076802, 2011.
- [21] Y. Xu, B. Yan, H.-J. Zhang, J. Wang, G. Xu, P. Tang, W. Duan, and S.-C. Zhang, “Large-gap quantum spin Hall insulators in tin films,” *Physical Review Letters*, vol. 111, no. 13, p. 136804, 2013.
- [22] Y. H. Lu, D. Zhou, T. Wang, S. A. Yang, and J. Z. Jiang, “Topological properties of atomic lead film with honeycomb structure,” *Scientific Reports*, vol. 6, no. 1, p. 21723, 2016.
- [23] F. D. M. Haldane, “Model for a quantum Hall effect without Landau levels: Condensed-matter realization of the "parity-anomaly",” *Physics Review Letters*, vol. 61, no. 18, pp. 2015-2018, 1988.
- [24] S. Ryu, C. Mudry, C.-Y. Hou, and C. Chamon, “Masses in graphenelike two-dimensional electronic systems: Topological defects in order parameters and their fractional exchange statistics,” *Physical Review B*, vol. 80, no. 20, p. 205319, 2009.
- [25] B. A. Bernevig and S.-C. Zhang, “Quantum spin Hall effect,” *Physical Review Letters*, vol. 96, no. 10, p. 106802, 2006.

- [26] C. Xu and J. E. Moore, “Stability of the quantum spin Hall effect: Effects of interactions, disorder, and \mathbb{Z}_2 topology,” *Physical Review B*, vol. 73, no. 4, p. 045322, 2006.
- [27] X. Wan, A. M. Turner, A. Vishwanath, and S. Y. Savrasov, “Topological semimetal and Fermi-arc surface states in the electronic structure of pyrochlore iridates,” *Physical Review B*, vol. 83, no. 20, p. 205101, 2011.
- [28] A. A. Burkov and L. Balents, “Weyl semimetal in a topological insulator multilayer,” *Physical Review Letters*, vol. 107, no. 12, p. 127205, 2011.
- [29] L. Lu, L. Fu, J. D. Joannopoulos, and M. Soljačić, “Weyl points and line nodes in gyroid photonic crystals,” *Nature Photonics*, vol. 7, no. 4, pp. 294-299, 2013.
- [30] M. Gong, S. Tewari, and C. Zhang, “BCS-BEC crossover and topological phase transition in 3D spin-orbit coupled degenerate Fermi gases,” *Physical Review Letters*, vol. 107, no. 19, p. 195303, 2011.
- [31] H. Weng, C. Fang, Z. Fang, B. A. Bernevig, and X. Dai, “Weyl semimetal phase in noncentrosymmetric transition-metal monophosphides,” *Physical Review X*, vol. 5, no. 1, p. 011029, 2015.
- [32] S.-Y. Xu, I. Belopolski, N. Alidoust, M. Neupane, G. Bian, C. Zhang, R. Sankar, G. Chang, Z. Yuan, C.-C. Lee, S. -M. Huang, H. Zheng, J. Ma, D. S. Sanchez, B. Wang, A. Bansil, F. Chou, P. P. Shibayev, H. Lin, S. Jia, and M. Z. Hasan, “Discovery of a Weyl fermion semimetal and topological Fermi arcs,” *Science*, vol. 349, no. 6248, pp. 613-617, 2015.
- [33] L. X. Yang, Z. K. Liu, Y. Sun, H. Peng, H. F. Yang, T. Zhang, B. Zhou, Y. Zhang, Y. F. Guo, M. Rahn, D. Prabhakaran, Z. Hussain, S. -K. Mo, C. Felser, B. Yan, and Y. L. Chen, “Weyl semimetal phase in the non-centrosymmetric compound TaAs,” *Nature Physics*, vol. 11, no. 9, pp. 728-732, 2015.
- [34] S. Murakami, “Phase transition between the quantum spin Hall and insulator phases in 3D: emergence of a topological gapless phase,” *New Journal of Physics*, vol. 9, no. 9, pp. 356-356, 2007.
- [35] D. Pesin and A. H. MacDonald, “Spintronics and pseudospintronics in graphene and topological insulators,” *Nature Materials*, vol. 11, no. 5, pp. 409-416, 2012.
- [36] V. K. Joshi, “Spintronics: A contemporary review of emerging electronics devices,” *Engineering Science and Technology, an International Journal*, vol. 19, no. 3, pp. 1503-1513, 2016.
- [37] W. Han, R. K. Kawakami, M. Gmitra, and J. Fabian, “Graphene spintronics,” *Nature Nanotechnology*, vol. 9, no. 10, pp. 794-807, 2014.
- [38] A. Candini, S. Klyatskaya, M. Ruben, W. Wernsdorfer, and M. Affronte, “Graphene spintronic devices with molecular nanomagnets,” *Nano Letters*, vol. 11, no. 7, pp. 2634-2639, 2011.

- [39] S. D. Bader and S. S. P. Parkin, “Spintronics,” *Annual Review of Condensed Matter Physics*, vol. 1, no. 1, pp. 71-88, 2010.
- [40] I. Žutić, J. Fabian, and S. D. Sarma, “Spintronics: Fundamentals and applications,” *Reviews of Modern Physics*, vol. 76, no. 2, pp. 323-410, 2004.
- [41] S. A. Wolf, D. D. Awschalom, R. A. Buhrman, J. M. Daughton, S. Von Molnár, M. L. Roukes, A. Y. Chtchelkanova, and D. M. Treger, “Spintronics: a spin-based electronics vision for the future,” *Science*, vol. 294, no. 5546, pp. 1488-1495, 2001.
- [42] Y. Fan and K. L. Wang, “Spintronics based on topological insulators,” *Spin*, vol. 6, no. 2, p. 1640001, World Scientific, 2016.
- [43] D. Awschalom and N. Samarth, “Trend: Spintronics without magnetism,” *Physics*, vol. 2, p. 50, 2009.
- [44] K. Behnia, “Polarized light boosts valleytronics,” *Nature Nanotechnology*, vol. 7, no. 8, pp. 488-489, 2012.
- [45] J. R. Schaibley, H. Yu, G. Clark, P. Rivera, J. S. Ross, K. L. Seyler, W. Yao, and X. Xu, “Valleytronics in 2D materials,” *Nature Reviews Materials*, vol. 1, no. 11, pp. 1-15, 2016.
- [46] S. A. Vitale, D. Nezich, J. O. Varghese, P. Kim, N. Gedik, P. Jarillo-Herrero, D. Xiao, and M. Rothschild, “Valleytronics: Opportunities, challenges, and paths forward,” *Small*, vol. 14, no. 38, p. 1801483, 2018.
- [47] N. Tombros, C. Jozsa, M. Popinciuc, H. T. Jonkman, and B. J. Van Wees, “Electronic spin transport and spin precession in single graphene layers at room temperature,” *Nature*, vol. 448, no. 7153, pp. 571-574, 2007.
- [48] B. Dlubak, M.-B. Martin, C. Deranlot, B. Servet, S. Xavier, R. Mattana, M. Sprinkle, C. Berger, W. A. De Heer, F. Petroff, A. Anane, P. Seneor, and A. Fert, “Highly efficient spin transport in epitaxial graphene on SiC,” *Nature Physics*, vol. 8, no. 7, pp. 557-561, 2012.
- [49] W. Han and R. K. Kawakami, “Spin relaxation in single-layer and bilayer graphene,” *Physical Review Letters*, vol. 107, no. 4, p. 047207, 2011.
- [50] S. Jo, D.-K. Ki, D. Jeong, H.-J. Lee, and S. Kettemann, “Spin relaxation properties in graphene due to its linear dispersion,” *Physical Review B*, vol. 84, no. 7, p. 075453, 2011.
- [51] M. Gmitra, D. Kochan, and J. Fabian, “Spin-orbit coupling in hydrogenated graphene,” *Physical Review Letters*, vol. 110, no. 24, p. 246602, 2013.
- [52] C. Weeks, J. Hu, J. Alicea, M. Franz, and R. Wu, “Engineering a robust quantum spin Hall state in graphene via adatom deposition,” *Physical Review X*, vol. 1, no. 2, p. 021001, 2011.

- [53] J. Hu, J. Alicea, R. Wu, and M. Franz, “Giant topological insulator gap in graphene with $5d$ adatoms,” *Physical Review Letters*, vol. 109, no. 26, p. 266801, 2012.
- [54] Y. S. Dedkov, M. Fonin, U. Rüdiger, and C. Laubschat, “Rashba effect in the graphene/Ni(111) system,” *Physical Review Letters*, vol. 100, no. 10, p. 107602, 2008.
- [55] D. Huertas-Hernando, F. Guinea, and A. Brataas, “Spin-orbit coupling in curved graphene, fullerenes, nanotubes, and nanotube caps,” *Physical Review B*, vol. 74, no. 15, p. 155426, 2006.
- [56] M. P. López-Sancho and M. C. Muñoz, “Intrinsic spin-orbit interactions in flat and curved graphene nanoribbons,” *Physical Review B*, vol. 83, no. 7, p. 075406, 2011.
- [57] M. Zarea and N. Sandler, “Rashba spin-orbit interaction in graphene and zigzag nanoribbons,” *Physical Review B*, vol. 79, no. 16, p. 165442, 2009.
- [58] J. Balakrishnan, G. K. W. Koon, A. Avsar, Y. Ho, J. H. Lee, M. Jaiswal, S.-J. Baeck, J.-H. Ahn, A. Ferreira, M. A. Cazalilla, A. H. Castro Neto, and B. Özyilmaz, “Giant spin Hall effect in graphene grown by chemical vapour deposition,” *Nature Communications*, vol. 5, no. 1, p. 4748, 2014.
- [59] L. Wang, I. Meric, P. Y. Huang, Q. Gao, Y. Gao, H. Tran, T. Taniguchi, K. Watanabe, L. M. Campos, D. A. Muller, J. Guo, P. Kim, J. Hone, K. L. Shepard, and C. R. Dean, “One-dimensional electrical contact to a two-dimensional material,” *Science*, vol. 342, no. 6158, pp. 614-617, 2013.
- [60] H. Dery, H. Wu, B. Ciftcioglu, M. Huang, Y. Song, R. Kawakami, J. Shi, I. Krivorotov, I. Zutic, and L. J. Sham, “Nanospintronics based on magnetologic gates,” *IEEE Transactions on Electron Devices*, vol. 59, no. 1, pp. 259-262, 2011.
- [61] A. Rycerz, J. Tworzydło, and C. W. J. Beenakker, “Valley filter and valley valve in graphene,” *Nature Physics*, vol. 3, no. 3, pp. 172-175, 2007.
- [62] J. L. Garcia-Pomar, A. Cortijo, and M. Nieto-Vesperinas, “Fully valley-polarized electron beams in graphene,” *Physical Review Letters*, vol. 100, no. 23, p. 236801, 2008.
- [63] H. Schomerus, “Helical scattering and valleytronics in bilayer graphene,” *Physical Review B*, vol. 82, no. 16, p. 165409, 2010.
- [64] W. Yao, D. Xiao, and Q. Niu, “Valley-dependent optoelectronics from inversion symmetry breaking,” *Physical Review B*, vol. 77, no. 23, p. 235406, 2008.
- [65] T. Cai, S. A. Yang, X. Li, F. Zhang, J. Shi, W. Yao, and Q. Niu, “Magnetic control of the valley degree of freedom of massive Dirac fermions with application to transition metal dichalcogenides,” *Physical Review B*, vol. 88, no. 11, p. 115140, 2013.

- [66] P. Recher, B. Trauzettel, A. Rycerz, Y. M. Blanter, C. W. J. Beenakker, and A. F. Morpurgo, “Aharonov-Bohm effect and broken valley degeneracy in graphene rings,” *Physical Review B*, vol. 76, no. 23, p. 235404, 2007.
- [67] D. S. L. Abergel and T. Chakraborty, “Generation of valley polarized current in bilayer graphene,” *Applied Physics Letters*, vol. 95, no. 6, p. 062107, 2009.
- [68] D. Gunlycke and C. T. White, “Valley and spin polarization from graphene line defect scattering,” *Journal of Vacuum Science & Technology B*, vol. 30, no. 3, p. 03D112, 2012.
- [69] Y. Jiang, T. Low, K. Chang, M. I. Katsnelson, and F. Guinea, “Generation of pure bulk valley current in graphene,” *Physical Review Letters*, vol. 110, no. 4, p. 046601, 2013.
- [70] T. Fujita, M. B. A. Jalil, and S. G. Tan, “Valley filter in strain engineered graphene,” *Applied Physics Letters*, vol. 97, no. 4, p. 043508, 2010.
- [71] H. Pan, X. Li, H. Jiang, Y. Yao, and S. A. Yang, “Valley-polarized quantum anomalous Hall phase and disorder-induced valley-filtered chiral edge channels,” *Physical Review B*, vol. 91, no. 4, p. 045404, 2015.
- [72] F. Zhang, J. Jung, G. A. Fiete, Q. Niu, and A. H. MacDonald, “Spontaneous quantum Hall states in chirally stacked few-layer graphene systems,” *Physical Review Letters*, vol. 106, no. 15, p. 156801, 2011.
- [73] R. V. Gorbachev, J. C. W. Song, G. L. Yu, A. V. Kretinin, F. Withers, Y. Cao, A. Mishchenko, I. V. Grigorieva, K. S. Novoselov, L. S. Levitov, and A. K. Geim, “Detecting topological currents in graphene superlattices,” *Science*, vol. 346, no. 6208, pp. 448-451, 2014.
- [74] H. Pan, X. Li, F. Zhang, and S. A. Yang, “Perfect valley filter in a topological domain wall,” *Physical Review B*, vol. 92, no. 4, p. 041404, 2015.
- [75] B. A. Bernevig, T. L. Hughes, and S.-C. Zhang, “Quantum spin Hall effect and topological phase transition in HgTe quantum wells,” *Science*, vol. 314, no. 5806, pp. 1757-1761, 2006.
- [76] A. R. Mellnik, J. S. Lee, A. Richardella, J. L. Grab, P. J. Mintun, M. H. Fischer, A. Vaezi, A. Manchon, E.-A. Kim, N. Samarth, and D. C. Ralph, “Spin-transfer torque generated by a topological insulator,” *Nature*, vol. 511, no. 7510, pp. 449-451, 2014.
- [77] L. Liu, A. Richardella, I. Garate, Y. Zhu, N. Samarth, and C.-T. Chen, “Spin-polarized tunneling study of spin-momentum locking in topological insulators,” *Physical Review B*, vol. 91, no. 23, p. 235437, 2015.
- [78] J. Wu, J. Liu, and X.-J. Liu, “Topological spin texture in a quantum anomalous Hall insulator,” *Physical Review Letters*, vol. 113, no. 13, p. 136403, 2014.
- [79] S. Guan, Z.-M. Yu, Y. Liu, G.-B. Liu, L. Dong, Y. Lu, Y. Yao, and S. A. Yang, “Artificial gravity field, astrophysical analogues, and topological phase

- transitions in strained topological semimetals,” *npj Quantum Materials*, vol. 2, no. 1, p. 23, 2017.
- [80] X. Xiao, Y. Liu, Z. Liu, G. Ai, S. A. Yang, and G. Zhou, “All-electric spin modulator based on a two-dimensional topological insulator,” *Applied Physics Letters*, vol. 108, no. 3, p. 032403, 2016.
- [81] Y. Fan, P. Upadhyaya, X. Kou, M. Lang, S. Takei, Z. Wang, J. Tang, L. He, L.-T. Chang, M. Montazeri, G. Yu, W. Jiang, T. Nie, R. N. Schwartz, Y. Tserkovnyak, and K. L. Wang, “Magnetization switching through giant spin-orbit torque in a magnetically doped topological insulator heterostructure,” *Nature Materials*, vol. 13, no. 7, pp. 699-704, 2014.
- [82] Y. Fan, X. Kou, P. Upadhyaya, Q. Shao, L. Pan, M. Lang, X. Che, J. Tang, M. Montazeri, K. Murata, L.-T. Chang, M. Akyol, G. Yu, T. Nie, K. L. Wong, J. Liu, Y. Wang, Y. Tserkovnyak, and K. L. Wang, “Electric-field control of spin-orbit torque in a magnetically doped topological insulator,” *Nature Nanotechnology*, vol. 11, no. 4, pp. 352-359, 2016.
- [83] C. H. Li, O. Van’t Erve, J. T. Robinson, Y. Liu, L. Li, and B. T. Jonker, “Electrical detection of charge-current-induced spin polarization due to spin-momentum locking in Bi_2Se_3 ,” *Nature Nanotechnology*, vol. 9, no. 3, p. 218, 2014.
- [84] J. Tang, L.-T. Chang, X. Kou, K. Murata, E. S. Choi, M. Lang, Y. Fan, Y. Jiang, M. Montazeri, W. Jiang, Y. Wang, L. He, and K. L. Wang, “Electrical detection of spin-polarized surface states conduction in $(\text{Bi}_{0.53}\text{Sb}_{0.47})_2\text{Te}_3$ topological insulator,” *Nano Letters*, vol. 14, no. 9, pp. 5423-5429, 2014.
- [85] Y. Ando, T. Hamasaki, T. Kurokawa, K. Ichiba, F. Yang, M. Novak, S. Sasaki, K. Segawa, Y. Ando, and M. Shiraishi, “Electrical detection of the spin polarization due to charge flow in the surface state of the topological insulator $\text{Bi}_{1.5}\text{Sb}_{0.5}\text{Te}_{1.7}\text{Se}_{1.3}$,” *Nano Letters*, vol. 14, no. 11, pp. 6226-6230, 2014.
- [86] J. Tian, I. Childres, H. Cao, T. Shen, I. Miotkowski, and Y. P. Chen, “Topological insulator based spin valve devices: Evidence for spin polarized transport of spin-momentum-locked topological surface states,” *Solid State Communications*, vol. 191, pp. 1-5, 2014.
- [87] J. Tian, I. Miotkowski, S. Hong, and Y. P. Chen, “Electrical injection and detection of spin-polarized currents in topological insulator $\text{Bi}_2\text{Te}_2\text{Se}$,” *Scientific Reports*, vol. 5, no. 1, p. 14293, 2015.
- [88] A. Dankert, J. Geurs, M. V. Kamalakar, S. Charpentier, and S. P. Dash, “Room temperature electrical detection of spin polarized currents in topological insulators,” *Nano Letters*, vol. 15, no. 12, pp. 7976-7981, 2015.
- [89] Y. Shiomi, K. Nomura, Y. Kajiwara, K. Eto, M. Novak, K. Segawa, Y. Ando, and E. Saitoh, “Spin-electricity conversion induced by spin injection into topological insulators,” *Physical Review Letters*, vol. 113, no. 19, p. 196601, 2014.

- [90] P. Deorani, J. Son, K. Banerjee, N. Koirala, M. Brahlek, S. Oh, and H. Yang, “Observation of inverse spin Hall effect in bismuth selenide,” *Physical Review B*, vol. 90, no. 9, p. 094403, 2014.
- [91] M. Jamali, J. S. Lee, J. S. Jeong, F. Mahfouzi, Y. Lv, Z. Zhao, B. K. Nikolić, K. A. Mkhoyan, N. Samarth, and J.-P. Wang, “Giant spin pumping and inverse spin Hall effect in the presence of surface and bulk spin-orbit coupling of topological insulator Bi_2Se_3 ,” *Nano Letters*, vol. 15, no. 10, pp. 7126-7132, 2015.
- [92] A. A. Baker, A. I. Figueroa, L. J. Collins-McIntyre, G. van der Laan, and T. Hesjedal, “Spin pumping in ferromagnet-topological insulator-ferromagnet heterostructures,” *Scientific Reports*, vol. 5, no. 1, p. 7907, 2015.
- [93] J.-C. Rojas-Sánchez, S. Oyarzún, Y. Fu, A. Marty, C. Vergnaud, S. Gambarelli, L. Vila, M. Jamet, Y. Ohtsubo, A. Taleb-Ibrahimi, P. Le Fèvre, F. Bertran, N. Reyren, J.-M. George, and A. Fert, “Spin to charge conversion at room temperature by spin pumping into a new type of topological insulator: α -Sn films,” *Physical Review Letters*, vol. 116, no. 9, p. 096602, 2016.
- [94] J. Tian, S. Hong, I. Miotkowski, S. Datta, and Y. P. Chen, “Observation of current-induced, long-lived persistent spin polarization in a topological insulator: A rechargeable spin battery,” *Science Advances*, vol. 3, no. 4, p. e1602531, 2017.
- [95] D. Kurebayashi and K. Nomura, “Theory for spin torque in Weyl semimetal with magnetic texture,” *Scientific Reports*, vol. 9, no. 1, p. 5365, 2019.
- [96] D. E. Kharzeev and H.-U. Yee, “Anomaly induced chiral magnetic current in a Weyl semimetal: Chiral electronics,” *Physical Review B*, vol. 88, no. 11, p. 115119, 2013.
- [97] S. S.-L. Zhang, A. A. Burkov, I. Martin, and O. G. Heinonen, “Spin-to-charge conversion in magnetic Weyl semimetals,” *Physical Review Letters*, vol. 123, no. 18, p. 187201, 2019.
- [98] S.-Y. Xu, I. Belopolski, D. S. Sanchez, M. Neupane, G. Chang, K. Yaji, Z. Yuan, C. Zhang, K. Kuroda, G. Bian, C. Guo, H. Lu, T.-R. Chang, N. Alidoust, H. Zheng, C.-C. Lee, S.-M. Huang, C.-H. Hsu, H.-T. Jeng, A. Bansil, T. Neupert, F. Komori, T. Kondo, S. Shin, H. Lin, S. Jia, and M. Z. Hasan, “Spin polarization and texture of the Fermi arcs in the Weyl fermion semimetal TaAs,” *Physical Review Letters*, vol. 116, no. 9, p. 096801, 2016.
- [99] H. B. Nielsen and M. Ninomiya, “The Adler-Bell-Jackiw anomaly and Weyl fermions in a crystal,” *Physics Letters B*, vol. 130, no. 6, pp. 389-396, 1983.
- [100] D. T. Son and B. Z. Spivak, “Chiral anomaly and classical negative magnetoresistance of Weyl metals,” *Physical Review B*, vol. 88, no. 10, p. 104412, 2013.
- [101] S. A. Parameswaran, T. Grover, D. A. Abanin, D. A. Pesin, and A. Vishwanath, “Probing the chiral anomaly with nonlocal transport in three-

- dimensional topological semimetals,” *Physical Review X*, vol. 4, no. 3, p. 031035, 2014.
- [102] A. C. Potter, I. Kimchi, and A. Vishwanath, “Quantum oscillations from surface Fermi arcs in Weyl and Dirac semimetals,” *Nature Communications*, vol. 5, no. 1, p. 5161, 2014.
- [103] S. A. Yang, H. Pan, and F. Zhang, “Chirality-dependent Hall effect in Weyl semimetals,” *Physical Review Letters*, vol. 115, no. 15, p. 156603, 2015.
- [104] H. Pan, M. Wu, Y. Liu, and S. A. Yang, “Electric control of topological phase transitions in Dirac semimetal thin films,” *Scientific Reports*, vol. 5, no. 1, p. 14639, 2015.
- [105] E. Liu, Y. Sun, N. Kumar, L. Muechler, A. Sun, L. Jiao, S.-Y. Yang, D. Liu, A. Liang, Q. Xu, J. Kroder, V. Süß, H. Borrmann, C. Shekhar, Z. Wang, C. Xi, W. Wang, W. Schnelle, S. Wirth, Y. Chen, S. T. B. Goennenwein, and C. Felser, “Giant anomalous Hall effect in a ferromagnetic kagome-lattice semimetal,” *Nature Physics*, vol. 14, no. 11, pp. 1125-1131, 2018.
- [106] D. Kurebayashi and K. Nomura, “Voltage-driven magnetization switching and spin pumping in Weyl semimetals,” *Physical Review Applied*, vol. 6, no. 4, p. 044013, 2016.
- [107] P. Li, J. Koo, W. Ning, J. Li, L. Miao, L. Min, Y. Zhu, Y. Wang, N. Alem, C.-X. Liu, Z. Mao, and B. Yan, “Giant room temperature anomalous Hall effect and tunable topology in a ferromagnetic topological semimetal Co_2MnAl ,” *Nature Communications*, vol. 11, no. 1, p. 3476, 2020.
- [108] J. Sinova, S. O. Valenzuela, J. Wunderlich, C. H. Back, and T. Jungwirth, “Spin Hall effects,” *Reviews of Modern Physics*, vol. 87, no. 4, pp. 1213-1260, 2015.
- [109] W. Han, Y. Otani, and S. Maekawa, “Quantum materials for spin and charge conversion,” *npj Quantum Materials*, vol. 3, no. 1, p. 27, 2018.
- [110] D. Huertas-Hernando, F. Guinea, and A. Brataas, “Spin-orbit-mediated spin relaxation in graphene,” *Physical Review Letters*, vol. 103, no. 14, p. 146801, 2009.
- [111] A. H. Castro Neto and F. Guinea, “Impurity-induced spin-orbit coupling in graphene,” *Physical Review Letters*, vol. 103, no. 2, p. 026804, 2009.
- [112] D. Kochan, M. Gmitra, and J. Fabian, “Spin relaxation mechanism in graphene: Resonant scattering by magnetic impurities,” *Physical Review Letters*, vol. 112, no. 11, p. 116602, 2014.
- [113] C. Ertler, S. Konschuh, M. Gmitra, and J. Fabian, “Electron spin relaxation in graphene: The role of the substrate,” *Physical Review B*, vol. 80, no. 4, p. 041405, 2009.

- [114] H. Min, J. E. Hill, N. A. Sinitsyn, B. R. Sahu, L. Kleinman, and A. H. MacDonald, “Intrinsic and Rashba spin-orbit interactions in graphene sheets,” *Physical Review B*, vol. 74, no. 16, p. 165310, 2006.
- [115] A. H. Castro Neto and F. Guinea, “Impurity-induced spin-orbit coupling in graphene,” *Physical Review Letters*, vol. 103, no. 2, p. 026804, 2009.
- [116] A. Ferreira, T. G. Rappoport, M. A. Cazalilla, and A. H. Castro Neto, “Extrinsic spin Hall effect induced by resonant skew scattering in graphene,” *Physical Review Letters*, vol. 112, no. 6, p. 066601, 2014.
- [117] M. Gmitra, D. Kochan, and J. Fabian, “Spin-orbit coupling in hydrogenated graphene,” *Physical Review Letters*, vol. 110, no. 24, p. 246602, 2013.
- [118] S. Irmer, T. Frank, S. Putz, M. Gmitra, D. Kochan, and J. Fabian, “Spin-orbit coupling in fluorinated graphene,” *Physical Review B*, vol. 91, no. 11, p. 115141, 2015.
- [119] A. Pachoud, A. Ferreira, B. Özyilmaz, and A. H. Castro Neto, “Scattering theory of spin-orbit active adatoms on graphene,” *Physical Review B*, vol. 90, no. 3, p. 035444, 2014.
- [120] C. Weeks, J. Hu, J. Alicea, M. Franz, and R. Wu, “Engineering a robust quantum spin Hall state in graphene via adatom deposition,” *Physical Review X*, vol. 1, no. 2, p. 021001, 2011.
- [121] C. L. Kane and E. J. Mele, “ Z_2 topological order and the quantum spin Hall effect,” *Physical Review Letters*, vol. 95, no. 14, p. 146802, 2005.
- [122] N. A. Sinitsyn, J. E. Hill, H. Min, J. Sinova, and A. H. MacDonald, “Charge and spin Hall conductivity in metallic graphene,” *Physical Review Letters*, vol. 97, no. 10, p. 106804, 2006.
- [123] D. Ma, Z. Li, and Z. Yang, “Strong spin-orbit splitting in graphene with adsorbed Au atoms,” *Carbon*, vol. 50, no. 1, pp. 297-305, 2012.
- [124] C. W. Groth, M. Wimmer, A. R. Akhmerov, and X. Waintal, “Kwant: a software package for quantum transport,” *New Journal of Physics*, vol. 16, no. 6, p. 063065, 2014.
- [125] P.-H. Chang, F. Mahfouzi, N. Nagaosa, and B. K. Nikolić, “Spin-Seebeck effect on the surface of a topological insulator due to nonequilibrium spin-polarization parallel to the direction of thermally driven electronic transport,” *Physical Review B*, vol. 89, no. 19, p. 195418, 2014.
- [126] Í. Adagideli, J. H. Bardarson, and Ph. Jacquod, “Electrical probing of the spin conductance of mesoscopic cavities,” *Journal of Physics: Condensed Matter*, vol. 21, no. 15, p. 155503, 2009.
- [127] D. C. Ralph and M. D. Stiles, “Spin transfer torques,” *Journal of Magnetism and Magnetic Materials*, vol. 320, no. 7, pp. 1190-1216, 2008.

- [128] K. Sato and H. Katayama-Yoshida, “First principles materials design for semiconductor spintronics,” *Semiconductor Science and Technology*, vol. 17, no. 4, pp. 367-376, 2002.
- [129] S. Datta and B. Das, “Electronic analog of the electro-optic modulator,” *Applied Physics Letters*, vol. 56, no. 7, pp. 665-667, 1990.
- [130] D. D. Awschalom, D. Loss, and N. Samarth, “Semiconductor spintronics and quantum computation,” *Springer Science & Business Media*, 2013.
- [131] Y. K. Kato, R. C. Myers, A. C. Gossard, and D. D. Awschalom, “Observation of the spin Hall effect in semiconductors,” *Science*, vol. 306, no. 5703, pp. 1910-1913, 2004.
- [132] J. Schliemann, “Colloquium: Persistent spin textures in semiconductor nanostructures,” *Reviews of Modern Physics*, vol. 89, no. 1, p. 011001, 2017.
- [133] V. M. Edelstein, “Spin polarization of conduction electrons induced by electric current in two-dimensional asymmetric electron systems,” *Solid State Communications*, vol. 73, no. 3, pp. 233-235, 1990.
- [134] J.-i. Inoue, G. E. W. Bauer, and L. W. Molenkamp, “Diffuse transport and spin accumulation in a Rashba two-dimensional electron gas,” *Physical Review B*, vol. 67, no. 3, p. 033104, 2003.
- [135] A. Yu. Silov, P. A. Blajnov, J. H. Wolter, R. Hey, K. H. Ploog, and N. S. Averkiev, “Current-induced spin polarization at a single heterojunction,” *Applied Physics Letters*, vol. 85, no. 24, pp. 5929-5931, 2004.
- [136] S. D. Ganichev, S. N. Danilov, P. Schneider, V. V. Bel’Kov, L. E. Golub, W. Wegscheider, D. Weiss, and W. Prettl, “Electric current-induced spin orientation in quantum well structures,” *Journal of Magnetism and Magnetic Materials*, vol. 300, no. 1, pp. 127-131, 2006.
- [137] M. I. D’yakonov and V. I. Perel’, “Possibility of orienting electron spins with current,” *Soviet Journal of Experimental and Theoretical Physics Letters*, vol. 13, p. 467, 1971.
- [138] M. I. Dyakonov and V. I. Perel, “Current-induced spin orientation of electrons in semiconductors,” *Physics Letters A*, vol. 35, no. 6, pp. 459-460, 1971.
- [139] J. E. Hirsch, “Spin Hall effect,” *Physical Review Letters*, vol. 83, no. 9, pp. 1834-1837, 1999.
- [140] M. Governale, F. Taddei, and R. Fazio, “Pumping spin with electrical fields,” *Physical Review B*, vol. 68, no. 15, p. 155324, 2003.
- [141] A. G. Mal’shukov, C. S. Tang, C. S. Chu, and K. A. Chao, “Spin-current generation and detection in the presence of an ac gate,” *Physical Review B*, vol. 68, no. 23, p. 233307, 2003.

- [142] S. Murakami, N. Nagosa, and S.-C. Zhang, “SU(2) non-Abelian holonomy and dissipationless spin current in semiconductors,” *Physical Review B*, vol. 69, no. 23, p. 235206, 2004.
- [143] M. Scheid, M. Kohda, Y. Kunihashi, K. Richter, and J. Nitta, “All-electrical detection of the relative strength of Rashba and Dresselhaus spin-orbit interaction in quantum wires,” *Physical Review Letters*, vol. 101, no. 26, p. 266401, 2008.
- [144] A. G. Aronov and Yu. B. Lyanda-Geller, “Nuclear electric resonance and orientation of carrier spins by an electric field,” *Soviet Journal of Experimental and Theoretical Physics Letters.*, vol. 50, p. 431, 1989.
- [145] E. Saitoh, M. Ueda, H. Miyajima, and G. Tatara, “Conversion of spin current into charge current at room temperature: Inverse spin-Hall effect,” *Applied Physics Letters*, vol. 88, no. 18, p. 182509, 2006.
- [146] T. Kimura, Y. Otani, T. Sato, S. Takahashi, and S. Maekawa, “Room-temperature reversible spin Hall effect,” *Physical Review Letters*, vol. 98, no. 15, p. 156601, 2007.
- [147] K. Uchida, S. Takahashi, K. Harii, J. Ieda, W. Koshibae, K. Ando, S. Maekawa, and E. Saitoh, “Observation of the spin Seebeck effect,” *Nature*, vol. 455, no. 7214, pp. 778-781, 2008.
- [148] S. O. Valenzuela and M. Tinkham, “Direct electronic measurement of the spin Hall effect,” *Nature*, vol. 442, no. 7099, pp. 176-179, 2006.
- [149] T. Seki, Y. Hasegawa, S. Mitani, S. Takahashi, H. Imamura, S. Maekawa, J. Nitta, and K. Takanashi, “Giant spin Hall effect in perpendicularly spin-polarized FePt/Au devices,” *Nature Materials*, vol. 7, no. 2, pp. 125-129, 2008.
- [150] S. D. Ganichev, E. L. Ivchenko, V. V. Bel’kov, S. A. Tarasenko, M. Sollinger, D. Weiss, W. Wegscheider, and W. Prettl, “Spin-galvanic effect,” *Nature*, vol. 417, no. 6885, pp. 153-156, 2002.
- [151] J. C. R. Sánchez, L. Vila, G. Desfonds, S. Gambarelli, J. P. Attané, J. M. De Teresa, C. Magén, and A. Fert, “Spin-to-charge conversion using Rashba coupling at the interface between non-magnetic materials,” *Nature Communications*, vol. 4, no. 1, p. 2944, 2013.
- [152] Í. Adagideli, M. Scheid, M. Wimmer, G. E. W. Bauer, and K. Richter, “Extracting current-induced spins: spin boundary conditions at narrow Hall contacts,” *New Journal of Physics*, vol. 9, no. 10, p. 382, 2007.
- [153] I. Žutić, J. Fabian, and S. Das Sarma, “Spin-polarized transport in inhomogeneous magnetic semiconductors: Theory of magnetic/nonmagnetic $p - n$ junctions,” *Physical Review Letters*, vol. 88, no. 6, p. 066603, 2002.
- [154] K. Shen, G. Vignale, and R. Raimondi, “Microscopic theory of the inverse Edelstein effect,” *Physical Review Letters*, vol. 112, no. 9, p. 096601, 2014.

- [155] H. Zhang, C.-X. Liu, X.-L. Qi, X. Dai, Z. Fang, and S.-C. Zhang, "Topological insulators in Bi_2Se_3 , Bi_2Te_3 and Sb_2Te_3 with a single Dirac cone on the surface," *Nature Physics*, vol. 5, no. 6, pp. 438-442, 2009.
- [156] F. Zhang, C. L. Kane, and E. J. Mele, "Surface states of topological insulators." *Physical Review B*, vol. 86, no. 8, p. 081303(R), 2012.
- [157] P. G. Silvestrov, P. W. Brouwer, and E. G. Mishchenko, "Spin and charge structure of the surface states in topological insulators," *Physical Review B*, vol. 86, no. 7, p. 075302, 2012.
- [158] L. Brey and H. A. Fertig, "Electronic states of wires and slabs of topological insulators: Quantum Hall effects and edge transport," *Physical Review B*, vol. 89, no. 8, p. 085305, 2014.
- [159] Y. L. Chen, J. G. Analytis, J.-H. Chu, Z. K. Liu, S.-K. Mo, X.L. Qi, H. J. Zhang, D. H. Lu, X. Dai, Z. Fang, S. C. Zhang, I. R. Fisher, Z. Hussain, and Z.-X. Shen, "Experimental realization of a three-dimensional topological insulator, Bi_2Te_3 ," *Science*, vol. 325, no. 5937, pp. 178-181, 2009.
- [160] Y. Xia, D. Qian, D. Hsieh, L. Wray, A. Pal, H. Lin, A. Bansil, D. Grauer, Y. S. Hor, R. J. Cava, and M. Z. Hasan, "Observation of a large-gap topological-insulator class with a single Dirac cone on the surface," *Nature Physics*, vol. 5, no. 6, pp. 398-402, 2009.
- [161] Z. Alpichshev, J. G. Analytis, J.-H. Chu, I. R. Fisher, Y. L. Chen, Z. X. Shen, A. Fang, and A. Kapitulnik, "STM imaging of electronic waves on the surface of Bi_2Te_3 : Topologically protected surface states and hexagonal warping effects," *Physical Review Letters*, vol. 104, no. 1, p. 016401, 2010.
- [162] T. Zhang, P. Cheng, X. Chen, J.-F. Jia, X. Ma, K. He, L. Wang, H. Zhang, X. Dai, Z. Fang, X. Xie, and Q.-K. Xue, "Experimental demonstration of topological surface states protected by time-reversal symmetry," *Physical Review Letters*, vol. 103, no. 26, p. 266803, 2009.
- [163] P. Cheng, C. Song, T. Zhang, Y. Zhang, Y. Wang, J.-F. Jia, J. Wang, Y. Wang, B.-F. Zhu, X. Chen, X. Ma, K. He, L. Wang, X. Dai, Z. Fang, X. Xie, X.-L. Qi, C.-X. Liu, S.-C. Zhang, and Q.-K. Xue, "Landau quantization of topological surface states in Bi_2Se_3 ," *Physical Review Letters*, vol. 105, no. 7, p. 076801, 2010.
- [164] T. Hanaguri, K. Igarashi, M. Kawamura, H. Takagi, and T. Sasagawa, "Momentum-resolved Landau-level spectroscopy of Dirac surface state in Bi_2Se_3 ," *Physical Review B*, vol. 82, no. 8, p. 081305, 2010.
- [165] Z. Alpichshev, J. G. Analytis, J.-H. Chu, I. R. Fisher, and A. Kapitulnik, "STM imaging of a bound state along a step on the surface of the topological insulator Bi_2Te_3 ," *Physical Review B*, vol. 84, no. 4, p. 041104, 2011.
- [166] D. Hsieh, Y. Xia, L. Wray, D. Qian, A. Pal, J. H. Dil, J. Osterwalder, F. Meier, G. Bihlmayer, C. L. Kane, Y. S. Hor, R. J. Cava, and M. Z. Hasan,

- “Observation of unconventional quantum spin textures in topological insulators,” *Science*, vol. 323, no. 5916, pp. 919-922, 2009.
- [167] E. L. Ivchenko, Yu. B. Lyanda-Geller, and G. E. Pikus, “Current of thermalized spin-oriented photocarriers,” *Soviet Physics - Journal of Experimental and Theoretical Physics*, vol. 71, pp. 550-557, 1990.
- [168] S. D. Ganichev, M. Trushin, and J. Schliemann, in *Spintronics Handbook: Spin transport and magnetism*, edited by E. Y. Tsymbal and I. Žutić, *CRC Press Taylor & Francis Group*, vol. 2, p. 487, Chap. “Spin Polarization by Current,” 2012.
- [169] C. Gorini, A. Maleki Sheikhabadi, K. Shen, I. V. Tokatly, G. Vignale, and R. Raimondi, “Theory of current-induced spin polarization in an electron gas,” *Physical Review B*, vol. 95, no. 20, p. 205424, 2017.
- [170] Y. Ando and M. Shiraishi, “Spin to charge interconversion phenomena in the interface and surface states,” *Journal of the Physical Society of Japan*, vol. 86, no. 1, p. 011001, 2017.
- [171] C.-X. Liu, X.-L. Qi, H. Zhang, X. Dai, Z. Fang, and S.-C. Zhang, “Model Hamiltonian for topological insulators,” *Physical Review B*, vol. 82, no. 4, p. 045122, 2010.
- [172] J. H. Bardarson, P. W. Brouwer, and J. E. Moore, “Aharonov-Bohm oscillations in disordered topological insulator nanowires,” *Physical Review Letters*, vol. 105, no. 15, p. 156803, 2010.
- [173] J. Ziegler, R. Kozlovsky, C. Gorini, M.-H. Liu, S. Weishäupl, H. Maier, R. Fischer, D. A. Kozlov, Z. D. Kvon, N. Mikhailov, S. A. Dvoretzky, K. Richter, and D. Weiss, “Probing spin helical surface states in topological HgTe nanowires,” *Physical Review B*, vol. 97, no. 3, p. 035157, 2018.
- [174] A. A. Burkov and D. G. Hawthorn, “Spin and charge transport on the surface of a topological insulator,” *Physical Review Letters*, vol. 105, no. 6, p. 066802, 2010.
- [175] P. Schwab, R. Raimondi, and C. Gorini, “Spin-charge locking and tunneling into a helical metal,” *EPL (Europhysics Letters)*, vol. 93, no. 6, p. 67004, 2011.
- [176] E. G. Mishchenko, A. V. Shytov, and B. I. Halperin, “Spin current and polarization in impure two-dimensional electron systems with spin-orbit coupling,” *Physical Review Letters*, vol. 93, no. 22, p. 226602, 2004.
- [177] M. I. Dyakonov and V. I. Perel, “Spin relaxation of conduction electrons in noncentrosymmetric semiconductors,” *Soviet Physics Solid State, Ussr*, vol. 13, no. 12, pp. 3023-3026, 1972.
- [178] J. S. Lee, A. Richardella, D. R. Hickey, K. A. Mkhoyan, and N. Samarth, “Mapping the chemical potential dependence of current-induced spin polarization in a topological insulator,” *Physical Review B*, vol. 92, no. 15, p. 155312, 2015.

- [179] A. M. Bozkurt, B. Pekerten, and İ. Adagideli, “Work extraction and Landauer’s principle in a quantum spin Hall device,” *Physical Review B*, vol. 97, no. 24, p. 245414, 2018.
- [180] W. A. Coish and J. Baugh, “Nuclear spins in nanostructures,” *Physica Status Solidi (b)*, vol. 246, no. 10, pp. 2203-2215, 2009.
- [181] J. Schliemann, A. Khaetskii, and D. Loss, “Electron spin dynamics in quantum dots and related nanostructures due to hyperfine interaction with nuclei,” *Journal of Physics: Condensed Matter*, vol. 15, no. 50, pp. R1809-R1833, 2003.
- [182] M. I. Dyakonov and V. I. Perel, “Theory of optical spin orientation of electrons and nuclei in semiconductors,” in *Optical orientation, Netherlands: North-Holland*, 1984.
- [183] V. K. Kalevic, K. V. Kavokin, and I. A. Merkulov, “Dynamic nuclear polarization and nuclear fields,” in *Spin Physics in Semiconductors*, pp. 309-346, *Springer Berlin Heidelberg*, 2008.
- [184] B. Urbaszek, X. Marie, T. Amand, O. Krebs, P. Voisin, P. Maletinsky, A. Högele, and A. Imamoglu, “Nuclear spin physics in quantum dots: An optical investigation,” *Reviews of Modern Physics*, vol. 85, no. 1, pp. 79-133, 2013.
- [185] I. A. Merkulov, A. I. Efros, and M. Rosen, “Electron spin relaxation by nuclei in semiconductor quantum dots,” *Physical Review B*, vol. 65, no. 20, p. 205309, 2002.
- [186] G. Burkard, D. Loss, and D. P. DiVincenzo, “Coupled quantum dots as quantum gates,” *Physical Review B*, vol. 59, no. 3, pp. 2070-2078, 1999.
- [187] A. V. Khaetskii, D. Loss, and L. Glazman, “Electron spin decoherence in quantum dots due to interaction with nuclei,” *Physical Review Letters*, vol. 88, no. 18, p. 186802, 2002.
- [188] F. H. L. Koppens, K. C. Nowack, and L. M. K. Vandersypen, “Spin echo of a single electron spin in a quantum dot,” *Physical Review Letters*, vol. 100, no. 23, p. 236802, 2008.
- [189] J. Fischer, W. A. Coish, D. V. Bulaev, and D. Loss, “Spin decoherence of a heavy hole coupled to nuclear spins in a quantum dot,” *Physical Review B*, vol. 78, no. 15, p. 155329, 2008.
- [190] J. Fischer and D. Loss, “Hybridization and spin decoherence in heavy-hole quantum dots,” *Physical Review Letters*, vol. 105, no. 26, p. 266603, 2010.
- [191] C. Testelin, F. Bernardot, B. Eble, and M. Chamorro, “Hole-spin dephasing time associated with hyperfine interaction in quantum dots,” *Physical Review B*, vol. 79, no. 19, p. 195440, 2009.
- [192] E. A. Chekhovich, M. M. Glazov, A. B. Krysa, M. Hopkinson, P. Senellart, A. Lemaître, M. S. Skolnick, and A. I. Tartakovskii, “Element-sensitive measure-

- ment of the hole-nuclear spin interaction in quantum dots,” *Nature Physics*, vol. 9, no. 2, pp. 74-78, 2013.
- [193] K. Ono and S. Tarucha, “Nuclear-spin-induced oscillatory current in spin-blockaded quantum dots,” *Physical Review Letters*, vol. 92, no. 25, p. 256803, 2004.
- [194] K. Ono, D. G. Austing, Y. Tokura, and S. Tarucha, “Current rectification by Pauli exclusion in a weakly coupled double quantum dot system,” *Science*, vol. 297, no. 5585, pp. 1313-1317, 2002.
- [195] A. Pfund, I. Shorubalko, K. Ensslin, and R. Leturcq, “Suppression of spin relaxation in an InAs nanowire double quantum dot,” *Physical Review Letters*, vol. 99, no. 3, p. 036801, 2007.
- [196] M. S. Rudner and L. S. Levitov, “Self-polarization and dynamical cooling of nuclear spins in double quantum dots,” *Physical Review Letters*, vol. 99, no. 3, p. 036602, 2007.
- [197] F. H. L. Koppens, J. A. Folk, J. M. Elzerman, R. Hanson, L. H. Willems van Beveren, I. T. Vink, H. P. Tranitz, W. Wegscheider, L. P. Kouwenhoven, and L. M. K. Vandersypen, “Control and detection of singlet-triplet mixing in a random nuclear field,” *Science*, vol. 309, no. 5739, pp. 1346-1350, 2005.
- [198] A. Berg, M. Dobers, R. R. Gerhardtts, and K. v. Klitzing, “Magnetoquantum oscillations of the nuclear-spin-lattice relaxation near a two-dimensional electron gas,” *Physical Review Letters*, vol. 64, no. 21, pp. 2563-2566, 1990.
- [199] W. Desrat, D. K. Maude, M. Potemski, J. C. Portal, Z. R. Wasilewski, and G. Hill, “Resistively detected nuclear magnetic resonance in the quantum Hall regime: possible evidence for a Skyrme crystal,” *Physical Review Letters*, vol. 88, no. 25, p. 256807, 2002.
- [200] I. Tifrea and M. E. Flatté, “Electric field tunability of nuclear and electronic spin dynamics due to the hyperfine interaction in semiconductor nanostructures,” *Physical Review Letters*, vol. 90, no. 23, p. 237601, 2003.
- [201] B. Braunecker, P. Simon, and D. Loss, “Nuclear magnetism and electronic order in ^{13}C nanotubes,” *Physical Review Letters*, vol. 102, no. 11, p. 116403, 2009.
- [202] B. Braunecker, P. Simon, and D. Loss, “Nuclear magnetism and electron order in interacting one-dimensional conductors,” *Physical Review B*, vol. 80, no. 16, p. 165119, 2009.
- [203] P. Simon and D. Loss, “Nuclear spin ferromagnetic phase transition in an interacting two dimensional electron gas,” *Physical Review Letters*, vol. 98, no. 15, p. 156401, 2007.
- [204] P. Simon, B. Braunecker, and D. Loss, “Magnetic ordering of nuclear spins in an interacting two-dimensional electron gas,” *Physical Review B*, vol. 77, no. 4, p. 045108, 2008.

- [205] D. C. Dixon, K. R. Wald, P. L. McEuen, and M. R. Melloch, “Dynamic nuclear polarization at the edge of a two-dimensional electron gas,” *Physical Review B*, vol. 56, no. 8, p. 4743, 1997.
- [206] T. Machida, S. Ishizuka, T. Yamazaki, S. Komiyama, K. Muraki, and Y. Hirayama, “Spin polarization of fractional quantum Hall edge channels studied by dynamic nuclear polarization,” *Physical Review B*, vol. 65, no. 23, p. 233304, 2002.
- [207] E. V. Deviatov, A. Wirtz, A. Lorke, M. Yu. Melnikov, V. T. Dolgoplov, D. Reuter, and A. D. Wieck, “Two relaxation mechanisms observed in transport between spin-split edge states at high imbalance,” *Physical Review B*, vol. 69, no. 11, p. 115330, 2004.
- [208] A. Del Maestro, T. Hyart, and B. Rosenow, “Backscattering between helical edge states via dynamic nuclear polarization,” *Physical Review B*, vol. 87, no. 16, p. 165440, 2013.
- [209] A. M. Lunde and G. Platero, “Hyperfine interactions in two-dimensional HgTe topological insulators,” *Physical Review B*, vol. 88, no. 11, p. 115411, 2013.
- [210] A. M. Stoneham, “Theory of defects in solids: electronic structure of defects in insulators and semiconductors,” *Oxford University Press*, 2001.
- [211] J. Fischer, M. Trif, W. A. Coish, and D. Loss, “Spin interactions, relaxation and decoherence in quantum dots,” *Solid State Communications*, vol. 149, no. 35-36, pp. 1443-1450, 2009.
- [212] A. Abragam, “The principles of nuclear magnetism,” no. 32, *Oxford University Press*, 1961.
- [213] J. Fabian, A. Matos-Abiague, C. Ertler, P. Stano, and I. Žutić, “Semiconductor spintronics,” *Acta Physica Slovaca. Reviews and Tutorials*, vol. 57, no. 4-5, pp. 565-907, 2007.
- [214] M. Gueron, “Density of the conduction electrons at the nuclei in Indium Antimonide,” *Physical Review*, vol. 135, no. 1A, pp. A200-A205, 1964.
- [215] A. Pertsova and C. M. Canali, “Probing the wavefunction of the surface states in Bi₂Se₃ topological insulator: a realistic tight-binding approach,” *New Journal of Physics*, vol. 16, no. 6, p. 063022, 2014.
- [216] S. Mukhopadhyay, S. Krämer, H. Mayaffre, H. F. Legg, M. Orlita, C. Berthier, M. Horvatić, G. Martinez, M. Potemski, B. A. Piot, A. Materna, G. Strzelecka, and A. Hruban, “Hyperfine coupling and spin polarization in the bulk of the topological insulator Bi₂Se₃,” *Physical Review B*, vol. 91, no. 8, p. 081105, 2015.
- [217] N. J. Ghimire, Y. Luo, M. Neupane, D. J. Williams, E. D. Bauer, and F. Ronning, “Magnetotransport of single crystalline NbAs,” *Journal of Physics: Condensed Matter*, vol. 27, no. 15, p. 152201, 2015.

- [218] C. Shekhar, A. K. Nayak, Y. Sun, M. Schmidt, M. Nicklas, I. Leermakers, U. Zeitler, Y. Skourski, J. Wosnitza, Z. Liu, Y. Chen, W. Schnelle, H. Borrmann, Y. Grin, C. Felser, and B. Yan, “Extremely large magnetoresistance and ultrahigh mobility in the topological Weyl semimetal candidate NbP,” *Nature Physics*, vol. 11, no. 8, pp. 645-649, 2015.
- [219] X. Huang, L. Zhao, Y. Long, P. Wang, D. Chen, Z. Yang, H. Liang, M. Xue, H. Weng, Z. Fang, X. Dai, and G. Chen, “Observation of the chiral-anomaly-induced negative magnetoresistance in 3D Weyl semimetal TaAs,” *Physical Review X*, vol. 5, no. 3, p. 031023, 2015.
- [220] C. Zhang, S.-Y. Xu, I. Belopolski, Z. Yuan, Z. Lin, B. Tong, N. Alidoust, C.-C. Lee, S.-M. Huang, H. Lin, M. Neupane, D. S. Sanchez, H. Zheng, G. Bian, J. Wang, C. Zhang, T. Neupert, M. Z. Hasan, and S. Jia, “Observation of the Adler-Bell-Jackiw chiral anomaly in a Weyl semimetal,” *arXiv preprint arXiv:1503.02630*, 2015.
- [221] A. Fert, “Nobel lecture: Origin, development, and future of spintronics,” *Reviews of Modern Physics*, vol. 80, no. 4, pp. 1517-1530, 2008.
- [222] M. N. Ali, J. Xiong, S. Flynn, J. Tao, Q. D. Gibson, L. M. Schoop, T. Liang, N. Haldolaarachchige, M. Hirschberger, N. P. Ong, and R. J. Cava, “Large, non-saturating magnetoresistance in WTe₂,” *Nature*, vol. 514, no. 7521, pp. 205-208, 2014.
- [223] T. Liang, Q. Gibson, M. N. Ali, M. Liu, R. J. Cava, and N. P. Ong, “Ultrahigh mobility and giant magnetoresistance in the Dirac semimetal Cd₃As₂,” *Nature materials*, vol. 14, no. 3, pp. 280-284, 2015.
- [224] C.-L. Zhang, Z. Yuan, Q.-D. Jiang, B. Tong, C. Zhang, X. C. Xie, and S. Jia, “Electron scattering in tantalum monoarsenide,” *Physical Review B*, vol. 95, no. 8, p. 085202, 2017.
- [225] M. M. Vazifeh and M. Franz, “Electromagnetic response of Weyl semimetals,” *Physical Review Letters*, vol. 111, no. 2, p. 027201, 2013.
- [226] T. Morimoto and A. Furusaki, “Weyl and Dirac semimetals with \mathbb{Z}_2 topological charge,” *Physical Review B*, vol. 89, no. 23, p. 235127, 2014.
- [227] P. Baireuther, J. A. Hutasoit, J. Tworzydło, and C. W. J. Beenakker, “Scattering theory of the chiral magnetic effect in a Weyl semimetal: interplay of bulk Weyl cones and surface Fermi arcs,” *New Journal of Physics*, vol. 18, no. 4, p. 045009, 2016.
- [228] S.-Y. Xu, Y. Xia, L. A. Wray, S. Jia, F. Meier, J. H. Dil, J. Osterwalder, B. Slomski, A. Bansil, H. Lin, R. J. Cava, and M. Z. Hasan, “Topological phase transition and texture inversion in a tunable topological insulator,” *Science*, vol. 332, no. 6029, pp. 560-564, 2011.
- [229] M. Brahlek, N. Bansal, N. Koirala, S.-Y. Xu, M. Neupane, C. Liu, M. Z. Hasan, and S. Oh, “Topological-metal to band-insulator transition in (Bi_{1-x}In_x)₂Se₃ thin films,” *Physical Review Letters*, vol. 109, no. 18, p. 186403, 2012.

- [230] G. Zhang, H. Qin, J. Teng, J. Guo, Q. Guo, X. Dai, Z. Fang, and K. Wu, “Quintuple-layer epitaxy of thin films of topological insulator Bi_2Se_3 ,” *Applied Physics Letters*, vol. 95, no. 5, p. 053114, 2009.
- [231] H. Peng, K. Lai, D. Kong, S. Meister, Y. Chen, X.-L. Qi, S.-C. Zhang, Z.-X. Shen, and Y. Cui, “Aharonov–Bohm interference in topological insulator nanoribbons,” *Nature Materials*, vol. 9, no. 3, pp. 225-229, 2010.
- [232] Y. Zhang, K. He, C.-Z. Chang, C.-L. Song, L.-L. Wang, X. Chen, J.-F. Jia, Z. Fang, X. Dai, W.-Y. Shan, S.-Q. Shen, Q. Niu, X.-L. Qi, S.-C. Zhang, X.-C. Ma, and Q.-K. Xue, “Crossover of the three-dimensional topological insulator Bi_2Se_3 to the two-dimensional limit,” *Nature Physics*, vol. 6, no. 8, pp. 584-588, 2010.
- [233] G. B. Halász and L. Balents, “Time-reversal invariant realization of the Weyl semimetal phase,” *Physical Review B*, vol. 85, no. 3, p. 035103, 2012.
- [234] S. Ganeshan and S. Das Sarma, “Constructing a Weyl semimetal by stacking one-dimensional topological phases,” *Physical Review B*, vol. 91, no. 12, p. 125438, 2015.
- [235] L. Balents, “Weyl electrons kiss,” *Physics*, vol. 4, p. 36, 2011.
- [236] A. A. Burkov, M. D. Hook, and L. Balents, “Topological nodal semimetals,” *Physical Review B*, vol. 84, no. 23, p. 235126, 2011.
- [237] C. Reig, S. Cardoso, and S. C. Mukhopadhyay, “Giant magnetoresistance (GMR) sensors,” *Springer*, vol. 1, 2013.
- [238] W.-Y. Shan, H.-Z. Lu, and S.-Q. Shen, “Effective continuous model for surface states and thin films of three-dimensional topological insulators,” *New Journal of Physics*, vol. 12, no. 4, p. 043048, 2010.
- [239] D. Culcer, E. H. Hwang, T. D. Stanescu, and S. Das Sarma, “Two-dimensional surface charge transport in topological insulators,” *Physical Review B*, vol. 82, no. 15, p. 155457, 2010.
- [240] H. Lüth, “Solid surfaces, interfaces and thin films,” vol. 4. *Springer*, 2001.
- [241] R. Winkler, “Spin-orbit coupling effects in two-dimensional electron and hole systems,” *Springer*, 2003.

APPENDIX A: Edelstein Effect in Two-dimensional Quantum Wires

We consider a uniform quantum wire with Rashba spin-orbit interaction to investigate the Edelstein effect (or current-induced spin accumulation) in 2DEGs. The components of \vec{s} in 2DEGs with Rashba spin-orbit interaction are proportional to the applied electric field. Consider the electric field in \hat{x} direction, the current is in the same direction; therefore, the spin polarization is perpendicular to the current direction. The Hamiltonian of the system is

$$H = \frac{p_x^2 + p_y^2}{2m} + H_R + U_d, \quad (\text{A.1})$$

where $H_R = (\sigma_x p_y - \sigma_y p_x)$ represent the Rashba Hamiltonian, and the disorder potential U_d is introduced by static impurities in the scattering region with a length of L . In our numerical implementation, we use random on-site potential in the range of $[-U_d/2, U_d/2]$ in the scattering region. Also, $U_0 = \mu_L - \mu_R$ is applied between the left and right semi-infinite leads connected to the system to generate current in the \hat{x} direction. In order to have linear response approximation, U_0 is chosen small. We perform numerical simulation to calculate the different components of $\langle s_i \rangle$ averaged over 100 disorder configurations. Our results are in agreement with spin components

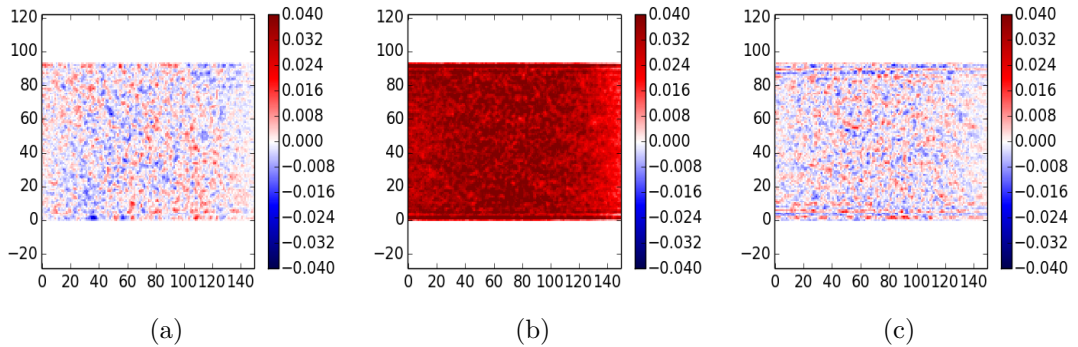


Figure A.1 The spin accumulation components (a) $\langle S_x \rangle$, (b) $\langle S_y \rangle$, and (c) $\langle S_z \rangle$ ($eV^{-1}a^{-2}$) averaged over 100 disorder configurations for a quantum wire. Parameters used are $\alpha = 0.2$, $W = 94a$, $L = 150a$, $U_d = 2$, and $E_F = 0.5$. $a = 1$ is the considered lattice constant.

calculated in Refs. [133] and [134] using Kubo formalism. As we see in Fig. A.1, spin accumulation components in \hat{x} and \hat{z} directions ($\langle S_x \rangle$ and $\langle S_z \rangle$) averaged over 100 disorder configurations vanish in the center of the scattering region and show substantial values at boundaries and interfaces of leads. But $\langle S_y \rangle$ averaged over 100 disorder configurations is approximately constant, especially in the center of the

disorder scattering region.

A.1 Extraction of Current-induced Spins

Spintronics devices like spin transistors have drawn a lot of attention in recent years. One of the essential features for operating these devices is spin-polarized current or local spin accumulation. In the previous section, we found that it depends on the current flow, i.e., by turning off the current, no spin is accumulated in the scattering region. So one way for having polarized spins, which does not decay and is not influenced by spin-relaxation, is adding a side pocket with no or negligible spin-orbit interaction to a 2D wire. Candidate spin extraction setup is a 2D quantum wire with spin-orbit interaction and a side pocket attached to its top with negligible spin-orbit interaction, see Fig. A.2. Spins are accumulated in the quantum wire region, as already explained in the previous section. Now, spins are extracted with the same polarization direction to the attached side pocket. By decreasing the width of contact between the scattering region and side pocket, the polarization magnitude of extracted spins increases [152], see Fig. A.3.

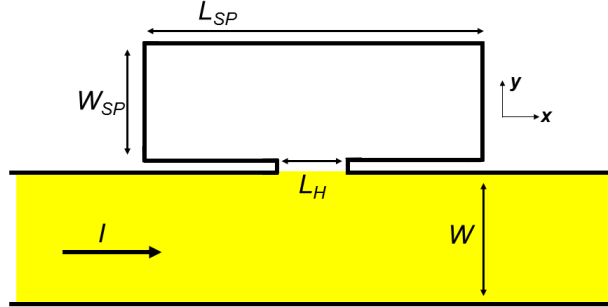


Figure A.2 A 2D quantum wire with Rashba spin-orbit interaction (yellow) with an attached normal side pocket.

A.2 Voltage Probe

So far, we have calculated the spin density which is proportional to spin accumulation. In this section, we find the relation between spin density (spin polarization) and spin accumulation numerically and analytically. Hence, we consider a three-terminal junction which is shown in Fig. A.4 where the third terminal is a voltage probe and spin probe, i.e., the voltage at this terminal is adjusted such that the total

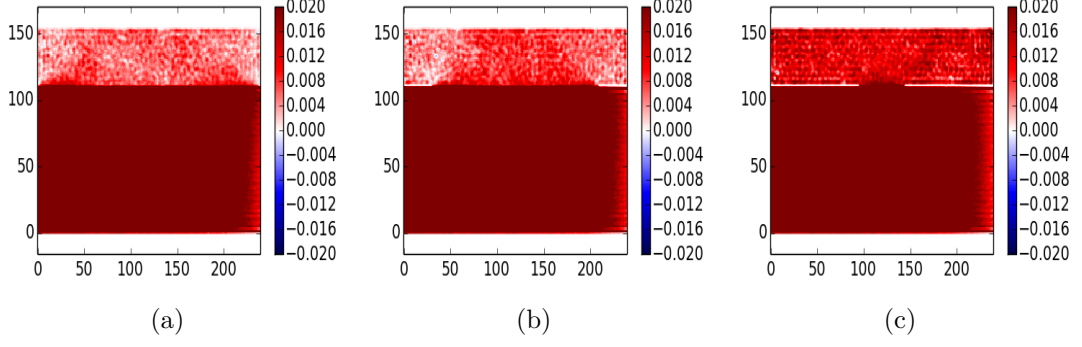


Figure A.3 Spin accumulation $\langle S_y \rangle$ ($eV^{-1}a^{-2}$) averaged over 1000 disorder configurations shown in Fig. A.2 with different length of contact between the scattering region and the side-pocket, (a) $L_H = 240a$, (b) $L_H = 180a$, and (c) $L_H = 50a$. Parameters used are a quantum wire with width $W = 112a$ and $L = 240a$ where an abrupt drop of the spin-orbit interaction strength is considered from $\alpha = 0.25$ for $y < 112a$, to zero for $y \geq 112a$, at the interface of the Rashba quantum wire and the normal side pocket; $L_{SP} = L$, $W_{SP} = 44a$, $U_d = 2$, and $E_F = 0.4eV$, see Fig. A.2. $a = 1$ is the considered lattice constant.

charge current and spin current flowing into terminal 3 is zero, $I_3^q = 0$ and $I_3^s = 0$. According to the Landauer-Büttiker theory, we can write net charge-spin current I_i^α flowing into terminal i as follows,

$$I_i^\alpha = \frac{e}{h} \sum_{\beta} (2N_i \delta_{\alpha\beta} - T_{ii}^{\alpha\beta}) \mu_i^\beta - \frac{e}{h} \sum_{j \neq i, \beta} T_{ij}^{\alpha\beta} \mu_j^\beta. \quad (\text{A.2})$$

Here, $\mu_i^0 = eV_i$ where V_i is the voltage applied to terminal i . μ_i^β for $\beta = x, y, z$ are components of the spin accumulation vector $\mu_i^{\vec{s}}$, spin potential along the corresponding axis, i.e. $\mu_i^\beta = \mu_i^{\vec{s}} = (\mu_i^x, \mu_i^y, \mu_i^z)$ (as an example $\mu_i^z = \mu_i^\uparrow - \mu_i^\downarrow$). $I_i^0 = I$ and $I_i^\beta = I_i^{\vec{s}}$ are charge current and the components of spin current in terminal i , respectively. Moreover, $T_{ij}^{\alpha\beta}$ is the spin-dependent transmission probabilities introduced by Adagideli et al. [126]:

$$T_{ij}^{\alpha\beta} = \sum_{m \in i, n \in j} \text{Tr}[t_{mn}^\dagger \sigma_\alpha t_{mn} \sigma_\beta], \quad (\text{A.3})$$

where σ_α , $\alpha = x, y, z$ are Pauli matrices and σ_0 is the identity matrix. The trace is taken over the spin degree of freedom and t_{mn} is a 2×2 matrix of spin-dependent transmission amplitudes from channel n in lead j to channel m in lead i .

Consider the case of $\mu_1^\beta = \mu_1^0$, $\mu_2^\beta = \mu_2^0$, and μ_3^β is non zero, see Fig. A.4. To have terminal 3 as a voltage probe and spin probe, the net charge current and spin current flowing into lead 3 must be zero, $I_3^\beta = 0$. Hence, by setting Eq. (A.2) = 0 for terminal 3, we can find μ_3^0 and $\mu_3^{\vec{s}}$ in terms of $\mu_1^0 \equiv \mu_1$ and $\mu_2^0 \equiv \mu_2$ via calculating spin-

dependent and energy-independent transmission probabilities (Eq. (A.3)). Fig. A.5

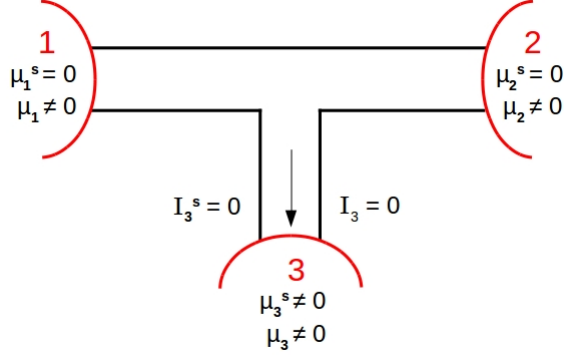


Figure A.4 A three-terminal junction where terminal three is a voltage probe and spin probe.

illustrates that the spin density calculated in 2D quantum wires is approximately spin accumulation over bias voltage between two reservoirs (leads). We find the corresponding analytical relation in the rest of this section.

The equilibrium electron density n_0 in semiconductors is given by

$$n_0 = \int_{-\text{inf}}^{\text{inf}} dE D(E) f_{\text{FD}}(E), \quad (\text{A.4})$$

where $D(E)$ is the density of states and $f_{\text{FD}}(E)$ is the Fermi-Dirac distribution function. The equilibrium density n_0 can be written in simpler form in the degenerate limit of 2DEG which $f_{\text{FD}}(E) = \theta(\mu - E)$:

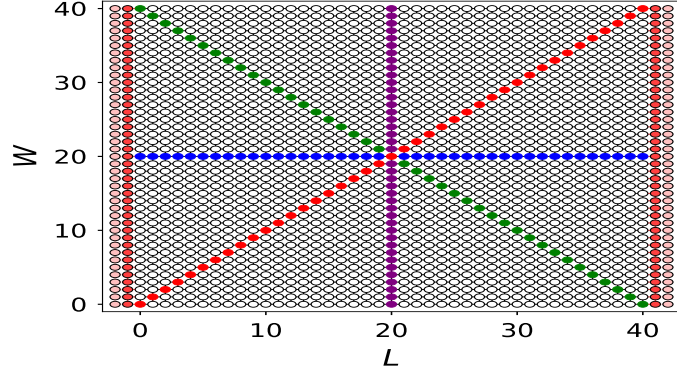
$$n_0 = D_{2\text{D}}(E)\mu, \quad (\text{A.5})$$

where $D_{2\text{D}}(E) = \frac{m^*}{\pi\hbar^2}$ denotes the 2D density of states and μ is the chemical potential. Moreover, the equilibrium densities for spin-up, n_+ , and spin-down electrons, n_- , can be written as $n_+ = n_- = \frac{n_0}{2}$ in nonmagnetic materials.

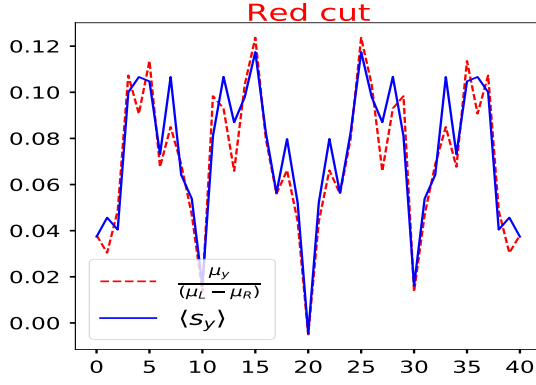
For small applied voltages and in diffusive systems, local quasichemical potential $\mu(\vec{r})$ is defined. This yields for 2DEGs

$$\mu(\vec{r}) = \frac{\pi\hbar^2}{m^*n(\vec{r})}, \quad (\text{A.6})$$

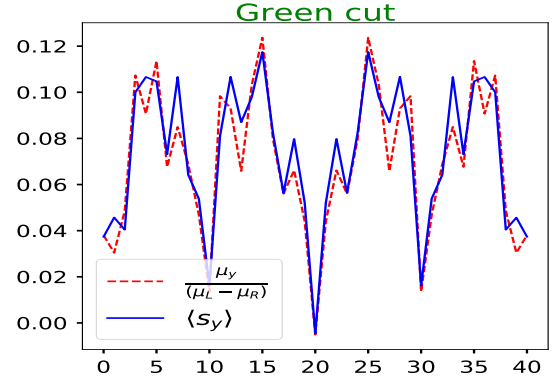
where $n(\vec{r})$ is the local electron density. However, the densities of spin-up and spin-down electrons are not necessarily equal anymore, $n_+(\vec{r}) \neq n_-(\vec{r})$, and the difference between the quasichemical potential of spin-up $\mu_+(\vec{r}) = (\frac{2\pi\hbar^2}{m^*})n_+(\vec{r})$ and spin-down electrons $\mu_-(\vec{r}) = (\frac{2\pi\hbar^2}{m^*})n_-(\vec{r})$ is called spin accumulation $\mu_s(\vec{r}) = \mu_+(\vec{r}) - \mu_-(\vec{r})$.



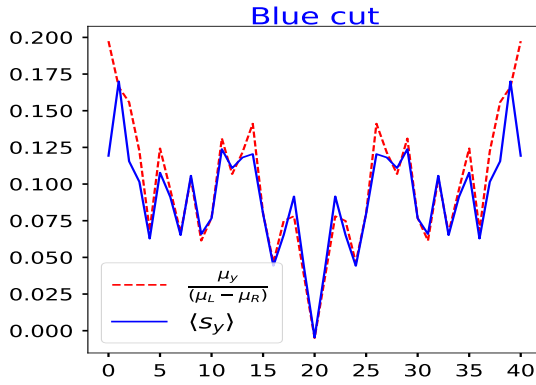
(a)



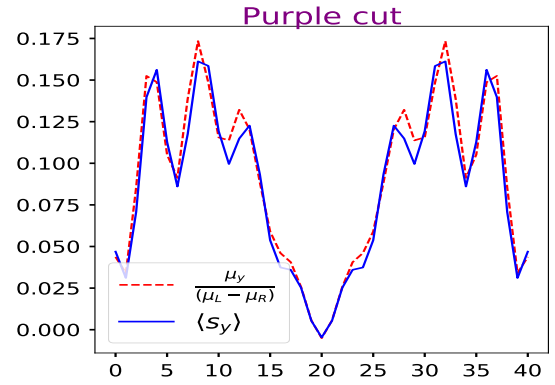
(b)



(c)



(d)



(e)

Figure A.5 (a) Scattering region of a three-terminal junction, where the third terminal is a scanning tunneling microscopy tip that hovers over the system. Spin density and spin accumulation over Voltage for specified sites corresponding to (b) Red cut, (c) Green cut, (d) Blue cut, and (e) Purple cut shown in panel (a).

Therefore, the spin accumulation is proportional to the spin density,

$$\vec{\mu}_s = \frac{2\pi\hbar^2}{m^s} \vec{s}. \quad (\text{A.7})$$

APPENDIX B: Effective Surface Hamiltonians and Spin Operators

Surface states in 3D topological insulators decay exponentially into the bulk and have energies in the bulk bandgap. We first consider a semi-infinite 3D topological insulator system situated in $z \geq 0$ ($z \leq 0$) with a surface normal $-\hat{\mathbf{z}}$ ($\hat{\mathbf{z}}$) pointing away from the bulk. By considering a vanishing BC at the surface, eigenfunctions corresponding to these states can be written as

$$\phi \sim u(k_x, k_y, \lambda_{1,2}) e^{i(k_x x + k_y y)} (e^{\pm \lambda_1 z} - e^{\pm \lambda_2 z}), \quad (\text{B.1})$$

where the \pm sign in the $\hat{\mathbf{z}}$ direction corresponds to a system with a surface normal in the $\mp \hat{\mathbf{z}}$ direction at $z = 0$. Here $\text{Re}(\lambda_{1,2}) > 0$ and $u(k_x, k_y, \lambda_{1,2})$ is a spinor that is an eigenstate of the 3D topological insulator Hamiltonian described in Eq. (4.20), corresponding to $k_x = k_y = 0$ and $k_z = -i\lambda_{1,2}$:

$$u^{\pm \hat{\mathbf{z}}} = \frac{1}{\sqrt{2}} \begin{bmatrix} \sqrt{1+\xi} \\ \mp i\sqrt{1-\xi} \\ 0 \\ 0 \end{bmatrix}, \quad v^{\pm \hat{\mathbf{z}}} = \frac{1}{\sqrt{2}} \begin{bmatrix} 0 \\ 0 \\ \sqrt{1+\xi} \\ \pm i\sqrt{1-\xi} \end{bmatrix} \quad (\text{B.2})$$

with energy dispersion to the lowest order of k given by

$$E^\pm = C + \xi M_0 \pm A_2 \sqrt{1 - \xi^2} k_\perp, \quad (\text{B.3})$$

where $k_\perp^2 = k_x^2 + k_y^2$. Hence, the effective surface Hamiltonian as given in the text is obtained through projecting the 3D topological insulator Hamiltonian in basis states given in Eq. (B.1) and using the spinor eigenstates stated in Eq. (B.2). To lowest order in k_x and k_y , this results in

$$H^{\pm \hat{\mathbf{z}}} = C + \xi M_0 \pm A_2 \sqrt{1 - \xi^2} \begin{pmatrix} 0 & ik_x + k_y \\ -ik_x + k_y & 0 \end{pmatrix}, \quad (\text{B.4})$$

which is introduced as Eq. (4.1) in the paper. The real spin operators for the $\hat{\mathbf{z}}$ surface are formed by projecting the spin operators in the basis of bulk states, Eq. (4.21), onto the two surface states

$$s_x = \sigma_x, \quad s_y = \sigma_y, \quad s_z = \sigma_z, \quad (\text{B.5})$$

which is stated as Eq. (4.2). The effective surface Hamiltonians and real spin operators corresponding to other surfaces can be calculated similarly.

APPENDIX C: Mean Free Time Estimation

We proceed with a Fermi's "golden rule" estimation of the mean free path. The surface modes are four-spinors with k -dependent components [238] due to (pseudo)spin-momentum coupling. Such k dependence can lead to substantial differences between lifetime and transport time [239]. In the case of uncorrelated disorder, however, the difference is only an $O(1)$ factor [175] and thus irrelevant for our estimations. We thus work exclusively with band-bottom $k = 0$ spinors. We consider a topological insulator slab extended in $\hat{\mathbf{x}}$ and $\hat{\mathbf{y}}$ directions, having a length L and a width W along the $\hat{\mathbf{x}}$ direction and $\hat{\mathbf{y}}$ direction, respectively, and a thickness H along the $\hat{\mathbf{z}}$ direction. We further assume white-noise disorder of the form $\langle V(\mathbf{r})V(\mathbf{r}') \rangle = \gamma \delta(\mathbf{r} - \mathbf{r}')$. Therefore, using spinors stated in Eq. (B.2) leads to

$$\langle |V_{kk'}|^2 \rangle = \frac{\gamma}{LW} \frac{\alpha}{\beta^2}, \quad (\text{C.1})$$

where $\alpha = \int_0^H dz f^2(z)$, $\beta = \int_0^H dz f(z)$ with $f(z) = (e^{-\lambda_1^* z} - e^{-\lambda_2^* z})(e^{-\lambda_1 z} - e^{-\lambda_2 z})$. We use Fermi's "golden rule" to derive the inverse mean free time and find

$$\frac{1}{\tau} = \sum_{k'} \frac{1}{\tau(k \rightarrow k')} = \frac{2\pi}{\hbar} \sum_{k'} \langle |V_{kk'}|^2 \rangle \delta(E_k - E_{k'}) \quad (\text{C.2})$$

for surface states of a disordered 3D topological insulator with semi-infinite boundary condition in the $\hat{\mathbf{z}}$ direction, i.e., $H \rightarrow \infty$. Based on Eq. (B.3), we have

$$\delta(E_k^+ - E_{k'}^+) = \frac{1}{A_2 \sqrt{1 - \xi^2}} \delta\left(k'_\perp - \frac{E^+ - C - \xi M_0}{A_2 \sqrt{1 - \xi^2}}\right). \quad (\text{C.3})$$

Hence, the resulting total ensemble-averaged mean free time of surface states on the $\hat{\mathbf{z}}$ surface reads

$$\frac{1}{\tau} = \frac{2\gamma}{\hbar} \frac{E^+ - C - \xi M_0}{A_2^2 (1 - \xi^2)} \frac{\alpha}{\beta^2}. \quad (\text{C.4})$$

Here, since λ 's are complex conjugate partners in our system, $\lambda_1 = \lambda_2^* = \tilde{a} + i\tilde{b}$, we find $\alpha = \frac{3\tilde{b}^4}{8\tilde{a}^5 + 10\tilde{a}^3\tilde{b}^2 + 2\tilde{a}\tilde{b}^4}$ and $\beta = \frac{\tilde{b}^2}{\tilde{a}^3 + \tilde{a}\tilde{b}^2}$.

Similarly, for an energy dispersion, to the lowest order of k , for $\hat{\mathbf{y}}$ plane surface states,

$$E^\pm = C + \eta M_0 \pm \sqrt{1 - \eta^2} \sqrt{A_2^2 k_x^2 + A_1^2 k_z^2}, \quad (\text{C.5})$$

we obtain the total ensemble-averaged inverse mean free time

$$\frac{1}{\tau} \simeq \frac{2\gamma}{\hbar} \frac{E^+ - C - \eta M_0}{A_2^2(1 - \eta^2)} \frac{\alpha'}{\beta'^2}, \quad (\text{C.6})$$

where we approximate the Fermi velocity, $v_F = v_{F,x}(\hat{\mathbf{y}})$, at this surface based on Eq. (C.5) since $A_2 > A_1$. Note that $\alpha(\beta)$ and $\alpha'(\beta')$ are different values since the depths of the surface states into the bulk in different surfaces are not the same according to the parameters of the Hamiltonian.

According to our mean free time and Fermi velocities derivations, Eqs. (4.31) and (4.32) yield

$$\left(\frac{\langle S_z \rangle}{d\langle n \rangle/dx} \right)_{-\hat{\mathbf{y}}} = \left(\frac{\eta(A_2\sqrt{1-\eta^2})^3 \beta'^2}{E^+ - C - \eta M_0 4\alpha'\gamma} \right)_{-\hat{\mathbf{y}}}, \quad (\text{C.7})$$

$$\left(\frac{\langle S_y \rangle}{d\langle n \rangle/dx} \right)_{+\hat{\mathbf{z}}} = \left(\frac{(A_2\sqrt{1-\xi^2})^3 \beta^2}{E^+ - C - \xi M_0 4\alpha\gamma} \right)_{+\hat{\mathbf{z}}}, \quad (\text{C.8})$$

where $\gamma = U_0^2 a^3$ in the discretized system.

APPENDIX D: $\eta = 0$ case

Here we provide figures for the case $D_2 = 0$ leading to $\eta = 0$. It is clearly seen that while there is negligible spin accumulation on the side of a 3D topological insulator [Fig. D.1(a)] spin extraction is non-negligible in the side pocket and spin polarization can be switched via a gate potential [see Figs. D.1(b) and D.1(c)].

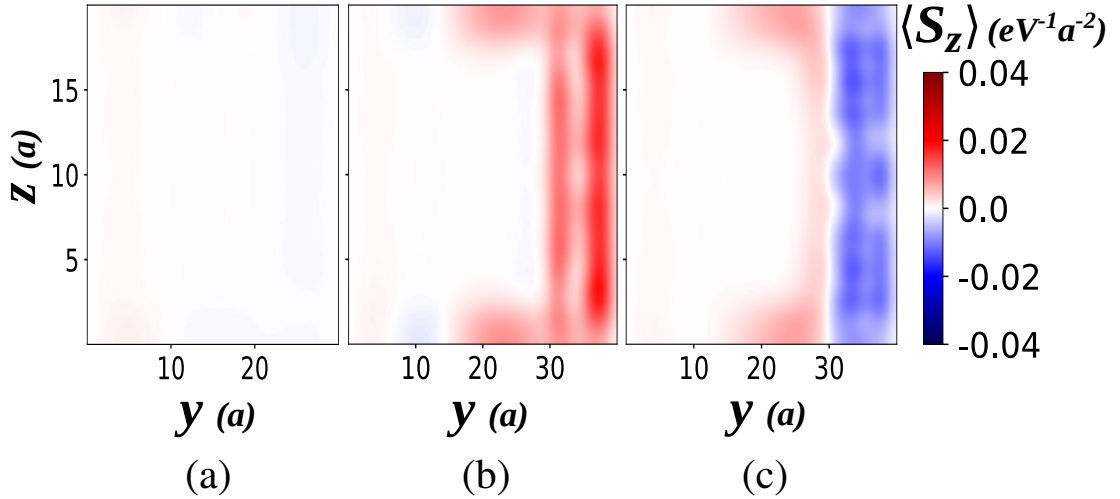


Figure D.1 Current-induced spin polarization into a side pocket at the side surface when $\eta = 0$. Spatial profile of the averaged spin polarization $\langle S_z(y, z) \rangle$ (averaged over 1000 disorder configurations) along cross sections in the \hat{x} direction. (a) $\langle S_z(y, z) \rangle$ corresponds to the system shown in Fig. 4.2(a). (b), (c) $\langle S_z(y, z) \rangle$ corresponds to the system shown in Fig. 4.5(a). In panels (b) and (c) the side pockets, $W_{SP} = 10a$, are doped to hole bands ($V_{\text{gate}} = -0.7\text{eV}$) and electron bands ($V_{\text{gate}} = 0.7\text{eV}$), respectively. Common parameters are $L = 30a$, $W = 30a$, $H = 20a$, $U_0 = 0.5\text{eV}$, and $E_F = 0.15\text{eV}$, which is in the bulk gap. We set $D_2 = 0$ in all parts of the system.

APPENDIX E: Spin-charge Coupled Dynamics for Topological Insulator $\hat{\mathbf{z}}$ Surface

The quasiclassical (Eilenberger) equation for a helical metal with a single Dirac cone in the diffusive regime ($\omega\tau \ll 1$ and $q\ell \ll 1$) with $\ell = v_F\tau$ the electronic mean free path (v_F is the Fermi velocity and τ is the momentum scattering time) reads [175]

$$\partial_t g + \frac{v_F}{2} \{\hat{\mathbf{z}} \times \boldsymbol{\sigma} \cdot \nabla, g\} + iv_F k_F [\hat{\mathbf{k}} \times \hat{\mathbf{z}} \cdot \boldsymbol{\sigma}, g] = -\frac{1}{\tau} g + \frac{1}{\tau} \langle g \rangle + \frac{1}{2\tau} \{\hat{\mathbf{k}} \times \hat{\mathbf{z}} \cdot \boldsymbol{\sigma}, \langle g \rangle\}, \quad (\text{E.1})$$

where $\langle \dots \rangle = \int d\phi / 2\pi \dots$ is the angle average in the momentum space. The quasiclassical Green's function $g = g(r, t, \epsilon, \phi)$ is a 2×2 matrix in the spin space, and it is a slowly varying function of space and time coordinates (r, t) with the energy ϵ , and the momentum angle $\phi = \arctan(k_y/k_x)$. This can be solved with the ansatz

$$g = g_0(\sigma_0 + \hat{\mathbf{k}} \times \hat{\mathbf{z}} \cdot \boldsymbol{\sigma}), \quad (\text{E.2})$$

where $g_0 = g_0(\mathbf{r}, t, \epsilon, \phi)$ is a scalar function. In the diffusive regime, the Green's function can be expanded in the spherical harmonics as follows

$$g = g_s + \mathbf{g}_p \cdot \hat{\mathbf{k}} \quad (\text{E.3})$$

with g_s the s -wave (isotropic) component, \mathbf{g}_p the p component (like a p -orbital). Here, we neglect the higher orders since we assume that each additional spherical harmonic is smaller than the previous term. To get the leading order form of the diffusion equation - where no gradient of the spins appear - only s - and p -waves need to be considered. Thus we enforce the following condition,

$$\langle \hat{k}_i \hat{k}_j g_0 \rangle \approx \frac{\delta_{ij}}{2} \langle g_0 \rangle. \quad (\text{E.4})$$

To have the spin space-gradient terms, we should consider d -wave order, which is beyond our assumption, Eq. (E.4). We obtain these terms later in this section.

Eq. (E.1) can be rewritten in the matrix form,

$$(1 + \tau \partial_t) g = -a M g - L g + N \langle g \rangle, \quad (\text{E.5})$$

where $a = 2v_F k_F \tau$ and $g = (\tilde{g}, g_z) = (g_0, g_x, g_y, g_z)$ is a four-vector the components of which are obtained by taking the trace $g_0 = \text{Tr}[g]$ and $g_i = (1/2)\text{Tr}[\sigma_i g]$ for $i = x, y, z$.

M, L, N are 4×4 matrices defined as follows,

$$M = \begin{pmatrix} 0 & K \\ -K^t & 0 \end{pmatrix} = \begin{pmatrix} 0 & 0 & 0 & 0 \\ 0 & 0 & 0 & \hat{k}_x \\ 0 & 0 & 0 & \hat{k}_y \\ 0 & -\hat{k}_x & -\hat{k}_y & 0 \end{pmatrix}, \quad K = \begin{pmatrix} 0 \\ \hat{k}_x \\ \hat{k}_y \end{pmatrix},$$

$$L = \begin{pmatrix} \hat{L} & 0 \\ 0 & 0 \end{pmatrix} = \begin{pmatrix} 0 & \ell\partial_y & -\ell\partial_x & 0 \\ \ell\partial_y & 0 & 0 & 0 \\ -\ell\partial_x & 0 & 0 & 0 \\ 0 & 0 & 0 & 0 \end{pmatrix},$$

$$N = \begin{pmatrix} \hat{N} & 0 \\ 0 & 1 \end{pmatrix} = \begin{pmatrix} 1 & \hat{k}_y & -\hat{k}_x & 0 \\ \hat{k}_y & 1 & 0 & 0 \\ -\hat{k}_x & 0 & 1 & 0 \\ 0 & 0 & 0 & 1 \end{pmatrix}.$$

Moreover, the normalization $K^t K = 1$ gives rise to

$$M^2 = - \begin{pmatrix} K K^t & 0 \\ 0 & K^t K \end{pmatrix} = - \begin{pmatrix} 0 & 0 & 0 & 0 \\ 0 & \hat{k}_x^2 & \hat{k}_x \hat{k}_y & 0 \\ 0 & \hat{k}_y \hat{k}_x & \hat{k}_y^2 & 0 \\ 0 & 0 & 0 & 1 \end{pmatrix},$$

and

$$M^3 = -M, \quad (\hat{k}_x^2 + \hat{k}_y^2 = 1).$$

The angle average of Eq. (E.1) reads

$$(1 + \tau\partial_t) \langle g \rangle = -a \langle Mg \rangle - L \langle g \rangle + \langle g \rangle, \quad (\langle N \rangle = 1). \quad (\text{E.6})$$

To get the equation of motion of $\langle Mg \rangle$ term, we multiply Eq. (E.5) by M and then take the angle average ($\langle MN \rangle = 0$)

$$(1 + \tau\partial_t) \langle Mg \rangle = -a \langle M^2 g \rangle - \langle MLg \rangle. \quad (\text{E.7})$$

We repeat the same procedure for the $\langle M^2 g \rangle$ term (recall $M^3 = -M$)

$$(1 + \tau\partial_t) \langle M^2 g \rangle = a \langle Mg \rangle - \langle M^2 Lg \rangle + \langle M^2 \rangle \langle g \rangle. \quad (\text{E.8})$$

The explicit form of Eq. (E.6) yields

$$\tau \partial_t \langle \tilde{g} \rangle = -a \langle K g_z \rangle - \tilde{L} \langle \tilde{g} \rangle, \quad (\text{E.9})$$

$$\tau \partial_t \langle g_z \rangle = a \langle K^t \tilde{g} \rangle. \quad (\text{E.10})$$

Similarly, Eq. (E.7) leads to

$$(1 + \tau \partial_t) \langle K g_z \rangle = -a \langle \tilde{M}^2 \tilde{g} \rangle, \quad (\text{E.11})$$

$$-(1 + \tau \partial_t) \langle k^t \tilde{g} \rangle = a \langle g_z \rangle - \ell (\partial_x \langle \hat{k}_y g_0 \rangle - \partial_y \langle \hat{k}_x g_0 \rangle). \quad (\text{E.12})$$

Finally Eq. (E.8) can be written as

$$(1 + \tau \partial_t) \langle \tilde{M}^2 \tilde{g} \rangle = a \langle K g_z \rangle - \langle \tilde{M}^2 \tilde{L} \tilde{g} \rangle + \langle \tilde{M}^2 \rangle \langle \tilde{g} \rangle, \quad (\text{E.13})$$

$$-(1 + \tau \partial_t) \langle g_z \rangle = -a \langle K^t \tilde{g} \rangle - \langle g_z \rangle. \quad (\text{E.14})$$

After some algebra calculations and considering $a \gg 1$ in a diffusive regime, we find

$$\tau \partial_t \langle g_0 \rangle = \ell (\partial_x \langle g_y \rangle - \partial_y \langle g_x \rangle), \quad (\text{E.15})$$

$$\tau \partial_t \langle g_x \rangle = \ell (\partial_y \langle \hat{k}_x^2 g_0 \rangle - \partial_x \langle \hat{k}_x \hat{k}_y g_0 \rangle) - \langle \hat{k}_x^2 \rangle \langle g_x \rangle - \langle \hat{k}_x \hat{k}_y \rangle \langle g_y \rangle - \ell \partial_y \langle g_0 \rangle, \quad (\text{E.16})$$

$$\tau \partial_t \langle g_y \rangle = \ell (\partial_x \langle \hat{k}_y \hat{k}_x g_0 \rangle - \partial_y \langle \hat{k}_y^2 g_0 \rangle) - \langle \hat{k}_y \hat{k}_x \rangle \langle g_x \rangle - \langle \hat{k}_y^2 \rangle \langle g_y \rangle + \ell \partial_x \langle g_0 \rangle, \quad (\text{E.17})$$

$$\langle g_z \rangle = \frac{1}{2k_F} (\partial_x \langle \hat{k}_y g_0 \rangle - \partial_y \langle \hat{k}_x g_0 \rangle). \quad (\text{E.18})$$

Using the condition stated earlier, $\langle \hat{k}_i \hat{k}_j g_0 \rangle \simeq \frac{1}{2} \delta_{ij} \langle g_0 \rangle$, we have

$$\partial_t \langle g_0 \rangle = v_F (\partial_x \langle g_y \rangle - \partial_y \langle g_x \rangle), \quad (\text{E.19})$$

$$\partial_t \langle g_x \rangle = -\frac{v_F}{2} \partial_y \langle g_0 \rangle - \frac{1}{2\tau} \langle g_x \rangle, \quad (\text{E.20})$$

$$\partial_t \langle g_y \rangle = \frac{v_F}{2} \partial_x \langle g_0 \rangle - \frac{1}{2\tau} \langle g_y \rangle. \quad (\text{E.21})$$

Therefore, spin-charge coupled dynamics including the first-order of the space and the time derivatives with the aid of charge density definition, $n = -\frac{N_0}{2} \int d\epsilon \langle g_0 \rangle$, and spin density definition, $\mathbf{s} = -\frac{N_0}{4} \int d\epsilon \langle \mathbf{g} \rangle$, for $\hat{\mathbf{z}}$ surface of a 3D topological insulator are

$$\partial_t n - 2v_F(\partial_x s_y - \partial_y s_x) = 0, \quad (\text{E.22})$$

$$\partial_t s_x + \frac{v_F}{4} \partial_y n + \frac{1}{2\tau} s_x = 0, \quad (\text{E.23})$$

$$\partial_t s_y - \frac{v_F}{4} \partial_x n + \frac{1}{2\tau} s_y = 0. \quad (\text{E.24})$$

Our findings are consistent with Schwab et al. results [175]. For finding higher order terms, we start from Eq. (E.5), $(1 + \tau \partial_t)g = -aMg - Lg + N \langle g \rangle$ and ignore $\tau \partial_t$ since $\tau \partial_t \ll 1$. Therefore, we have

$$g_0 = \ell(\partial_x g_y - \partial_y g_x) + \langle g_0 \rangle + \hat{k}_y \langle g_x \rangle - \hat{k}_x \langle g_y \rangle, \quad (\text{E.25})$$

$$g_x = -a\hat{k}_x g_z - \ell \partial_y g_0 + \hat{k}_y \langle g_0 \rangle + \langle g_x \rangle, \quad (\text{E.26})$$

$$g_y = -a\hat{k}_y g_z + \ell \partial_x g_0 - \hat{k}_x \langle g_0 \rangle + \langle g_y \rangle, \quad (\text{E.27})$$

$$g_z = a(\hat{k}_x g_x + \hat{k}_y g_y) + \langle g_z \rangle. \quad (\text{E.28})$$

Similarly, we find from Eq. (E.5) by ignoring the time and the space derivatives,

$$g = (1 + aM)^{-1} N \langle g \rangle, \quad (\text{E.29})$$

where

$$(1 + aM)^{-1} = \frac{1}{1 + a^2} \begin{pmatrix} 1 & 0 & 0 & 0 \\ 0 & 1 + a^2 \hat{k}_y^2 & -a^2 \hat{k}_x \hat{k}_y & -a \hat{k}_x \\ 0 & -a^2 \hat{k}_x \hat{k}_y & 1 + a^2 \hat{k}_x^2 & -a \hat{k}_y \\ 0 & a \hat{k}_x & a \hat{k}_y & 1 \end{pmatrix}, \quad (\text{E.30})$$

and

$$(1 + aM)^{-1}N = \frac{1}{1 + a^2} \begin{pmatrix} 1 & \hat{k}_y & -\hat{k}_x & 0 \\ (1 + a^2)\hat{k}_y & 1 + a^2\hat{k}_y^2 & -a^2\hat{k}_x\hat{k}_y & -a\hat{k}_x \\ -(1 + a^2)\hat{k}_x & -a^2\hat{k}_x\hat{k}_y & 1 + a^2\hat{k}_x^2 & -a\hat{k}_y \\ 0 & a\hat{k}_x & a\hat{k}_y & 1 \end{pmatrix}. \quad (\text{E.31})$$

Therefore, we find the following relations (recall $a \gg 1$)

$$g_x = \hat{k}_y \langle g_0 \rangle + \hat{k}_y^2 \langle g_x \rangle - \hat{k}_x \hat{k}_y \langle g_y \rangle, \quad (\text{E.32})$$

$$g_y = -\hat{k}_x \langle g_0 \rangle - \hat{k}_x \hat{k}_y \langle g_x \rangle + \hat{k}_x^2 \langle g_y \rangle. \quad (\text{E.33})$$

Then we multiply Eqs. (E.25) - (E.28) as well as Eqs. (E.32) - (E.33) by \hat{k}_x^2 , \hat{k}_y^2 , and $\hat{k}_x \hat{k}_y$ and take the angle average. After some lengthy algebra calculations, we find

$$\tau \partial_t \langle g_x \rangle = -\frac{1}{2} \langle g_x \rangle - \frac{\ell}{2} \partial_y \langle g_0 \rangle + \frac{\ell^2}{4} \partial_x \partial_y \langle g_y \rangle + \frac{\ell^2}{8} (\partial_x^2 + 3\partial_y^2) \langle g_x \rangle, \quad (\text{E.34})$$

$$\tau \partial_t \langle g_y \rangle = -\frac{1}{2} \langle g_y \rangle + \frac{\ell}{2} \partial_x \langle g_0 \rangle + \frac{\ell^2}{4} \partial_x \partial_y \langle g_x \rangle + \frac{\ell^2}{8} (\partial_y^2 + 3\partial_x^2) \langle g_y \rangle. \quad (\text{E.35})$$

By using definitions of charge and spin densities $n = -\frac{N_0}{2} \int d\epsilon \langle g_0 \rangle$ and $\mathbf{s} = -\frac{N_0}{4} \int d\epsilon \langle \mathbf{g} \rangle$, we obtain

$$\partial_t s_x = -\frac{1}{2\tau} s_x - \frac{v_F}{4} \partial_y n + \frac{D}{2} \partial_x \partial_y s_y + \frac{D}{4} (\partial_x^2 + 3\partial_y^2) s_x, \quad (\text{E.36})$$

$$\partial_t s_y = -\frac{1}{2\tau} s_y + \frac{v_F}{4} \partial_x n + \frac{D}{2} \partial_x \partial_y s_x + \frac{D}{4} (\partial_y^2 + 3\partial_x^2) s_y, \quad (\text{E.37})$$

where $D = \frac{v_F^2 \tau}{2}$.

APPENDIX F: Crystal Structure and Atomic Orbitals

In this section, we will review the crystal structure and the basis states around the Fermi level at the Γ point of Bi_2Se_3 [155, 171]. The \hat{z} axis is the growth direction, and the structure can be considered a repeating unit, quintuple layer, in which five atomic layers are stacked in different orders. To find the physical band structure of

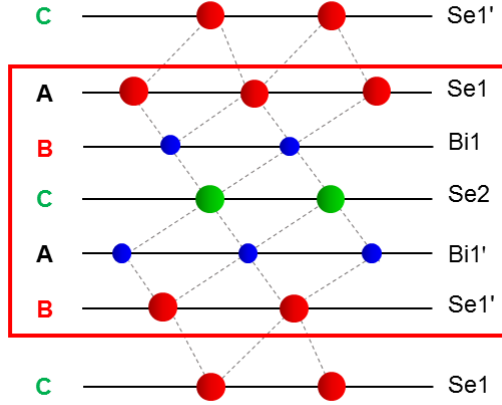


Figure F.1 The quintuple layer structure of the Bi_2Se_3 . The red rectangle denotes the stacking order of Se and Bi atomic layers along the \hat{z} direction where the Se2 atoms are considered inversion centers. Adopted from [155] with permission from the Springer Nature.

Bi_2Se_3 , we start from the atomic orbitals of Bi and Se atoms. Since the electronic configuration of Bi and Se are $6s^26p^3$ and $4s^24p^4$, respectively, the states close to the Fermi energy are dominantly made up of p orbitals. The coupling between layers within a quintuple (covalent-ionic) is stronger than the bonding between quintuple layers (van der Waals). Hence, we focus on chemical bonding in a quintuple layer to find states near the Fermi level. As it is shown in Fig. F.1, Se2 atoms can be considered inversion centers and Bi atoms are sandwiched between Se layers, so the strongest coupling is between Bi and Se layers which causes level repulsion and leads to pushing up Bi energy levels and pushing down Se energy levels and forming the new hybridized states $\{|B\rangle, |B'\rangle\}$ and $\{|S\rangle, |S'\rangle, \text{and } |S0\rangle\}$, respectively, see Fig. F.2, phase I. Because of the inversion symmetry in the system, hybridized states split into bonding and antibonding states with definite parity. The antibonding states have higher energy than bonding ones, which are illustrated in phase II of Fig. F.2 and have the form of

$$|P1^\pm, \alpha\rangle = \frac{1}{\sqrt{2}}(|B_\alpha\rangle \mp |B'_\alpha\rangle), \quad |P2^\pm, \alpha\rangle = \frac{1}{\sqrt{2}}(|S_\alpha\rangle \mp |S'_\alpha\rangle), \quad (\text{F.1})$$

where $\alpha = p_x, p_y, p_z$, and the upper index denotes the parity. We mainly focus on states close to the Fermi level, $P1_{x,y,z}^+$ and $P2_{x,y,z}^-$.

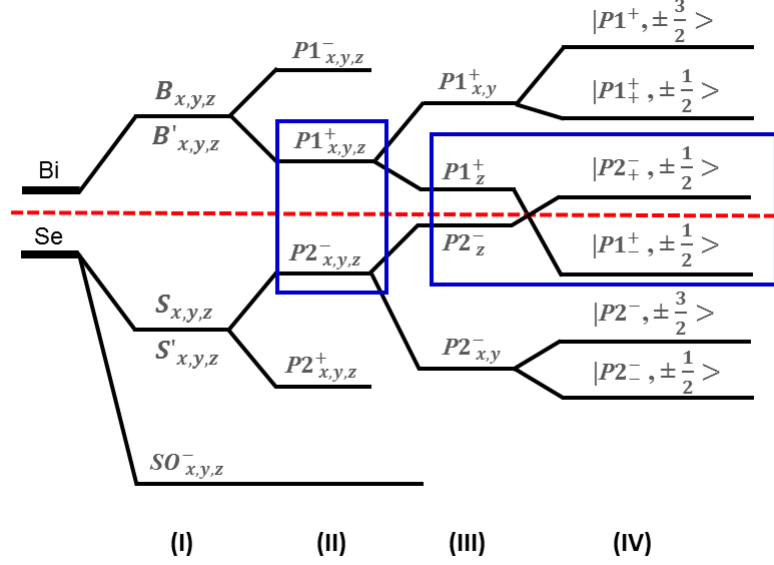


Figure F.2 Schematic of the band structure of Bi_2Se_3 . Originating from the atomic orbitals of Bi and Se, and the following four stages: (I) the hybridization of Bi and Se orbitals, (II) the chemical bonding, (III) the crystal field splitting, and (IV) the effect of the spin-orbit coupling. Adopted form [171] with permission from the American Physical Society.

Furthermore, the atomic orbitals have full rotation symmetry, but this symmetry can be broken by the crystal field. Since the crystal has a layered structure, the growth direction is in the \hat{z} direction, which is different from the \hat{x} or \hat{y} direction in the atomic plane, there is an energy splitting between p_z and $p_{x,y}$ orbitals for both $P1^+$ and $P2^-$ states. Hence, the conduction band mainly consists of $P1_z^+$ (corresponding to the hybridized states $|B\rangle$ and $|B'\rangle$) and the valence band mainly includes $P2_z^-$ (corresponding to the hybridized states $|S\rangle$ and $|S'\rangle$), see Fig. F.2, phase III. Finally, we consider the effect of the spin-orbit coupling on the atomic orbitals, which lifts the two-fold degeneracy of the aforementioned states. We go one step back and work with states $|\Lambda_\alpha, m_s\rangle$ with $\Lambda = P1^+, P2^-$, $\alpha = p_x, p_y, p_z$, and $m_s = \pm 1/2$ the spin quantum number in the \hat{z} direction. We transform the basis (p_x, p_y) to a basis (p_\pm) with definite orbital angular momentum in the \hat{z} direction, $m_l = 0, \pm 1$. By looking at spherical harmonic tables we have $p_+ \equiv p_1 = -\frac{1}{\sqrt{2}}(p_x + ip_y)$, $p_- \equiv p_{-1} = \frac{1}{\sqrt{2}}(p_x - ip_y)$, and $p_0 = p_z$. Accordingly, we write states $|\Lambda, m_l, m_s\rangle$ in terms of the previous basis:

$$\begin{aligned}
 |\Lambda, p_+, m_s\rangle &\equiv |\Lambda, 1, m_s\rangle = -\frac{1}{\sqrt{2}}(|\Lambda_{p_x}, m_s\rangle + i|\Lambda_{p_y}, m_s\rangle), \\
 |\Lambda, p_z, m_s\rangle &\equiv |\Lambda, 0, m_s\rangle = |\Lambda_{p_z}, m_s\rangle, \\
 |\Lambda, p_-, m_s\rangle &\equiv |\Lambda, -1, m_s\rangle = \frac{1}{\sqrt{2}}(|\Lambda_{p_x}, m_s\rangle - i|\Lambda_{p_y}, m_s\rangle).
 \end{aligned} \tag{F.2}$$

Spin-orbit coupling operator can be written in terms of the raising and lowering operators of orbital and spin angular momentum, $L_{\pm} = L_x \pm iL_y$ and $S_{\pm} = S_x \pm iS_y$:

$$\mathbf{S} \cdot \mathbf{L} = \frac{1}{2}(S_+L_- + S_-L_+) + S_zL_z. \quad (\text{F.3})$$

We apply this operator on the states written in the new basis. Hence, we see that the total angular momentum, $m_j = m_L + m_s$ is conserved because the spin-orbit coupling is rotationally invariant, and $|\Lambda, m_l, m_s\rangle$ states are also eigenstates of spin-orbit coupling term in the Hamiltonian. Within this basis, there are nonzero matrix elements of spin-orbit Hamiltonian [171], such as

$$\langle \Lambda, 1, -\frac{1}{2} | H_{SO} | \Lambda, 0, \frac{1}{2} \rangle = \frac{\lambda_{\Lambda}}{\sqrt{2}}, \quad (\text{F.4})$$

where the value λ_{Λ} is a linear combination of the spin-orbit coupling strength for Bi and Se and depends on Bi and Se orbitals mixture in each state. The sign of λ_{Λ} is always positive since the potential is attractive for atoms. $H_{\Lambda,SO}$ is block diagonal because spin-orbit term couples states with the same total angular momentum and each block corresponds to a different angular momentum projection m_j in the basis $|\Lambda, 1, \frac{1}{2}\rangle$, $|\Lambda, 1, -\frac{1}{2}\rangle$, $|\Lambda, 0, \frac{1}{2}\rangle$, $|\Lambda, -1, \frac{1}{2}\rangle$, $|\Lambda, 0, -\frac{1}{2}\rangle$, and $|\Lambda, -1, -\frac{1}{2}\rangle$. Therefore, after taking into account spin-orbit coupling, the eigenstates are given by

$$|\Lambda, \pm 3/2\rangle = |\Lambda, \pm 1, \pm 1/2\rangle \quad (\text{F.5})$$

$$|\Lambda_+, \pm 1/2\rangle = u_+^{\Lambda} |\Lambda, \pm 1, \mp 1/2\rangle + v_+^{\Lambda} |\Lambda, 0, \pm 1/2\rangle \quad (\text{F.6})$$

$$|\Lambda_-, \pm 1/2\rangle = u_-^{\Lambda} |\Lambda, \pm 1, \mp 1/2\rangle + v_-^{\Lambda} |\Lambda, 0, \pm 1/2\rangle \quad (\text{F.7})$$

with eigenenergies as follows: $E_{\frac{3}{2}}^{\Lambda}$, $E_{\frac{1}{2}}^{\Lambda+}$, and $E_{\frac{1}{2}}^{\Lambda-}$. Here, $u_{\pm}^{\Lambda} = \frac{\Delta E_{\Lambda} \pm \sqrt{(\Delta E_{\Lambda})^2 + \lambda_{\Lambda}^2/2}}{\sqrt{N_{\pm}}}$, $v_{\pm}^{\Lambda} = \frac{\lambda_{\Lambda}}{\sqrt{2N_{\pm}}}$ with $N_{\pm} = \lambda_{\Lambda}^2 + 2\Delta E_{\Lambda}^2 \pm 2\Delta E_{\Lambda} \sqrt{\Delta E_{\Lambda}^2 + \lambda_{\Lambda}^2/2}$ and $\Delta E_{\Lambda} = (E_{\Lambda,x} - E_{\Lambda,z} - \lambda_{\Lambda}/2)/2$. Therefore,

$$E_{\frac{3}{2}}^{\Lambda} = E_x^{\Lambda} + \frac{\lambda_{\Lambda}}{2}, \quad E_{\frac{1}{2}}^{\Lambda\pm} = \frac{E_{\Lambda,x} + E_{\Lambda,z} - \lambda_{\Lambda}/2}{2} \pm \sqrt{(\Delta E_{\Lambda})^2 + \lambda_{\Lambda}^2/2}. \quad (\text{F.8})$$

Finally, the states $|P1_{-}^{\pm}, \pm \frac{1}{2}\rangle$ and $|P2_{+}^{\pm}, \pm \frac{1}{2}\rangle$ are close to the Fermi energy and they are inverted due to the spin-orbit interaction; i.e., $|P1_{-}^{\pm}, \pm \frac{1}{2}\rangle$ is pushed down while $|P2_{+}^{\pm}, \pm \frac{1}{2}\rangle$ is pushed up in energy. These states are related to hybridized states stated in Eq. (F.1) and located below and above the Fermi energy, respectively. In the low energy limit, Bi_2Se_3 is in the topological phase because of the band inversion. For simplicity, we write $|\text{Bi}_p, \pm \frac{1}{2}\rangle \equiv |P1_{-}^{\pm}, \pm \frac{1}{2}\rangle$, $|\text{Se}_p, \pm \frac{1}{2}\rangle \equiv |P2_{+}^{\pm}, \pm \frac{1}{2}\rangle$, $u_1 \equiv u_{-}^{P1^{+}}$, $u_2 \equiv u_{+}^{P2^{-}}$, $v_1 \equiv v_{-}^{P1^{+}}$, and $v_2 \equiv v_{+}^{P2^{-}}$.

APPENDIX G: Further Details about Hyperfine Interactions Calculations

In this section, we briefly explain the applied method and approximations, which are similar to Lunde and Platero's approach and assumptions [209], to find the hyperfine interaction matrix elements.

G.1 Linear Combination of Atomic Orbitals Method for Bi_2Se_3 Family Materials

Valence and conduction bands for semiconductors, schematically shown in [213] stem from antibonding s -orbitals and bonding p -orbitals, respectively. Gueron estimates InSb conduction bands through using the LCAO method and considers a minus sign between atomic orbitals of In and Sb since the wavefunction should have s -symmetry [214]. The lattice periodic functions for GaAs conduction band (electron band with s -symmetry) and valence band (heavy hole band with p -symmetry) are also calculated through utilizing the LCAO method [189]. In the Bi_2Se_3 family materials, we have a quintuple layer including five atomic layers of two different atoms. Hence, there are five atoms in one unit cell, e.g., in Bi_2Se_3 there are two equivalent Se atoms (Se1 and Se1'), two equivalent Bi atoms (Bi1 and Bi1'), and one Se atom (Se2), which is not similar to the other Se atoms, see Fig. F.1. Therefore, the lattice periodic functions of Bi_2Se_3 via applying the LCAO method are as follows,

$$w_{\text{Bi}_p, \pm \frac{1}{2}}(\mathbf{r}) = N_{\text{Bi}_p, \pm \frac{1}{2}} \left[\alpha_{\text{Bi}_p}^{\text{Se1}} \Psi_{\text{Bi}_p, \pm \frac{1}{2}}^{\text{Se1}}(\mathbf{r} - \mathbf{d}) - \alpha_{\text{Bi}_p}^{\text{Bi1}} \Psi_{\text{Bi}_p, \pm \frac{1}{2}}^{\text{Bi1}}\left(\mathbf{r} - \frac{\mathbf{d}}{2}\right) \right. \\ \left. + \alpha_{\text{Bi}_p}^{\text{Se2}} \Psi_{\text{Bi}_p, \pm \frac{1}{2}}^{\text{Se2}}(\mathbf{r}) - \alpha_{\text{Bi}_p}^{\text{Bi1}'} \Psi_{\text{Bi}_p, \pm \frac{1}{2}}^{\text{Bi1}'}\left(\mathbf{r} + \frac{\mathbf{d}}{2}\right) + \alpha_{\text{Bi}_p}^{\text{Se1}'} \Psi_{\text{Bi}_p, \pm \frac{1}{2}}^{\text{Se1}'}(\mathbf{r} + \mathbf{d}) \right], \quad (\text{G.1})$$

$$w_{\text{Se}_p, \pm \frac{1}{2}}(\mathbf{r}) = N_{\text{Se}_p, \pm \frac{1}{2}} \left[\alpha_{\text{Se}_p}^{\text{Se1}} \Psi_{\text{Se}_p, \pm \frac{1}{2}}^{\text{Se1}}(\mathbf{r} - \mathbf{d}) + \alpha_{\text{Se}_p}^{\text{Bi1}} \Psi_{\text{Se}_p, \pm \frac{1}{2}}^{\text{Bi1}}\left(\mathbf{r} - \frac{\mathbf{d}}{2}\right) \right. \\ \left. + \alpha_{\text{Se}_p}^{\text{Se2}} \Psi_{\text{Se}_p, \pm \frac{1}{2}}^{\text{Se2}}(\mathbf{r}) - \alpha_{\text{Se}_p}^{\text{Bi1}'} \Psi_{\text{Se}_p, \pm \frac{1}{2}}^{\text{Bi1}'}\left(\mathbf{r} + \frac{\mathbf{d}}{2}\right) - \alpha_{\text{Se}_p}^{\text{Se1}'} \Psi_{\text{Se}_p, \pm \frac{1}{2}}^{\text{Se1}'}(\mathbf{r} + \mathbf{d}) \right], \quad (\text{G.2})$$

where $\Psi_{\text{Bi(Se)}_p, \pm \frac{1}{2}}^i$ for $i = \text{Se1}, \text{Bi1}, \text{Se2}, \text{Bi1}'$, and $\text{Se1}'$ is atomic-like wavefunctions centered on the i th atom. The symmetry of the atomic wavefunctions follows the symmetry of their corresponding bands. The atoms are connected by the vector \mathbf{d} , and the constants $N_{\text{Bi(Se)}_p, \pm \frac{1}{2}}$ is determined by the normalization of the lattice periodic function. The amount of electron sharing regarding each atom in the unit

cell is described by α 's, which satisfy $\sum_i |\alpha_i|^2 = 1$ for $i \in \{\text{Se1}, \text{Bi1}, \text{Se2}, \text{Bi1}', \text{Se1}'\}$ and the spatial distribution of the wavefunctions for conduction and valence bands can be found for each atom in the unit cell [215]. The relative signs between the atomic wavefunctions originate from the bonding and antibonding properties of the bands and the parity, which corresponds to the symmetric and antisymmetric linear combination of bonding or antibonding orbitals with respect to inversion center (Se2 atom) [240]. Here the band regarding Se_p with odd parity is considered as an antisymmetric LCAO including bonding superposition of Se and Bi orbitals on both sides of the inversion center (Se2), where the sign of each side wavefunction is opposite to the other one. Also, Bi_p with even parity with respect to Se2 is considered as a symmetric superposition of antibonding orbitals on both sides of the inversion center. Unlike materials such as HgTe [209], the signs used in Eqs. (G.1) and (G.2) based on properties of bands are important in the rest of our calculations regarding the matrix elements of hyperfine interactions. The LCAO method can be also used for s orbitals contributions to the lattice periodic functions.

G.2 Hyperfine Interaction Calculations via Linear Combination of Atomic Orbitals Method

We can change the integration of interaction matrix elements, Eq. (G.4), over the whole system volume into a summation of integrals over each unit cell volume,

$$\langle \varphi_{\mathbf{k},v,\tau} | H_{\text{HF},i} | \varphi_{\mathbf{k}',v',\tau'} \rangle \simeq \frac{v_a}{V} \sum_n \sum_{\mathcal{R}_n} e^{i(\mathbf{k}'-\mathbf{k})\cdot\mathcal{R}_n} \int_{v_a} d\boldsymbol{\rho} w_{v,\tau\frac{1}{2}}^*(\boldsymbol{\rho}) h_{i,n} w_{v',\tau'\frac{1}{2}}(\boldsymbol{\rho}), \quad (\text{G.3})$$

where $\boldsymbol{\rho}$ is the vector within the m th unit cell, so every point in space can be written in the form of $\mathbf{r} = \mathcal{R}_n + \boldsymbol{\rho}$. We have utilized the fact that the lattice periodicity of the lattice periodic functions do not change considerably on the atomic scale, i.e., $w_{v,\tau\frac{1}{2}}(\mathcal{R}_n + \boldsymbol{\rho}) \simeq w_{v,\tau\frac{1}{2}}(\boldsymbol{\rho})$ for all \mathcal{R}_n . Moreover, the integral over $\boldsymbol{\rho}$ is over the n th unit cell, whereas $h_{i,n}$ is the hyperfine interaction operator for the n th nuclei with nonzero spin that is located at \mathcal{R}_n . Furthermore, we can write the interaction matrix elements without the unit cell position dependence since hyperfine interactions are local in space,

$$\langle \varphi_{\mathbf{k},v,\tau} | H_{\text{HF},i} | \varphi_{\mathbf{k}',v',\tau'} \rangle = \frac{v_a}{V} \sum_n e^{i(\mathbf{k}'-\mathbf{k})\cdot\mathcal{R}_n} \int_{v_a} d\boldsymbol{\rho} w_{v,\tau\frac{1}{2}}^*(\boldsymbol{\rho}) h_{i,n} w_{v',\tau'\frac{1}{2}}(\boldsymbol{\rho}). \quad (\text{G.4})$$

Here, we interchange the sum over the nonzero spin-carrying lattice with the integral over the unit cell volume because random lattice points have nonzero nuclear spins.

Now, we can calculate integral over the unit cell part for finding matrix elements,

$\langle \varphi_{\mathbf{k},v,\tau} | H_{\text{HF},i} | \varphi_{\mathbf{k}',v',\tau'} \rangle$ through utilizing LCAO approach. For instance, the unit cell integral for a nonzero spin on the n th Bi1 nucleus located on $\boldsymbol{\rho} = \mathbf{d}/2$ with a contribution of p -orbital in $|\text{Bi}_p, \pm \frac{1}{2}\rangle$ state is

$$\int_{v_a} d\boldsymbol{\rho} w_{\text{Bi}_p, \tau \frac{1}{2}}^*(\boldsymbol{\rho}) h_{i,n} w_{\text{Bi}_p, \tau' \frac{1}{2}}(\boldsymbol{\rho}) \simeq N_{\text{Bi}_p, \tau \frac{1}{2}}^* N_{\text{Bi}_p, \tau' \frac{1}{2}} |\alpha_{\text{Bi}_p}^{\text{Bi1}}|^2 \quad (\text{G.5})$$

$$\times \int_{v_a} d\boldsymbol{\rho} \left[\Psi_{\text{Bi}_p, \tau \frac{1}{2}}^{\text{Bi1}} \left(\boldsymbol{\rho} - \frac{\mathbf{d}}{2} \right) \right]^* h_{i,n} \Psi_{\text{Bi}_p, \tau' \frac{1}{2}}^{\text{Bi1}} \left(\boldsymbol{\rho} - \frac{\mathbf{d}}{2} \right).$$

Therefore, we have obtained the way to find the matrix elements $\langle \varphi_{\mathbf{k},E,\tau} | H_{\text{HF},i} | \varphi_{\mathbf{k}',E,\tau'} \rangle$ for all three kinds of hyperfine interactions. Similarly, the other forms of matrix elements $\langle \varphi_{\mathbf{k},E,\tau} | H_{\text{HF},i} | \varphi_{\mathbf{k}',H,\tau'} \rangle$ and $\langle \varphi_{\mathbf{k},H,\tau} | H_{\text{HF},i} | \varphi_{\mathbf{k}',H,\tau'} \rangle$ can be calculated. Moreover, integrals including nonlocal contributions are negligible as it is found that nonlocal contributions are smaller at least two orders of magnitude compared to local contributions for GaAs [189].

We evaluate the integral of lattice periodic functions over the unit cell using the LCAO approach. We use Eqs. (G.1) and (G.2), and separate the angular and radial parts of the atomic wavefunctions $\Psi_{\text{Bi}(\text{Se})_p, \pm \frac{1}{2}}(\mathbf{r}) = R^{j_n}(r) \mathbb{Y}_{\text{Bi}(\text{Se})_p, \pm \frac{1}{2}}(\theta, \phi)$. This approximation is valid because the interactions are important only within the unit cell. Hence, the integral for Bi1 atom can be written as

$$\int_{v_a} d\boldsymbol{\rho} \left[\Psi_{\text{Bi}(\text{Se})_p, \tau \frac{1}{2}}^{\text{Bi1}} \left(\boldsymbol{\rho} - \frac{\mathbf{d}}{2} \right) \right]^* h_{i,n} \Psi_{\text{Bi}(\text{Se})_p, \tau' \frac{1}{2}}^{\text{Bi1}} \left(\boldsymbol{\rho} - \frac{\mathbf{d}}{2} \right) \quad (\text{G.6})$$

$$\approx \int_0^{r_{\text{max}}} dr r^2 \int_0^{2\pi} d\phi \int_0^\pi d\theta \sin(\theta) \left[\Psi_{\text{Bi}(\text{Se})_p, \tau \frac{1}{2}}^{\text{Bi1}}(\mathbf{r}) \right]^* h_{i,n} \Psi_{\text{Bi}(\text{Se})_p, \tau' \frac{1}{2}}^{\text{Bi1}}(\mathbf{r}).$$

The radial part of the integral yields effective interaction strength, which we call $A_{p,j_n}^{\text{Atomic}}$ for a given isotope. The expression for the p -like atomic coupling strength deducting from radial and including coefficients in $h_{2(3),n}$ is

$$A_{p,j_n}^{\text{Atomic}} \equiv \hbar^2 \gamma_2 \left\langle \frac{1}{r^3} \right\rangle_r^{j_n}, \quad (\text{G.7})$$

where γ_2 is defined in the Appendix H, the term $\left\langle \frac{1}{r^3} \right\rangle_r^{j_n}$ only depends on the type of the atom, j_n , that is determined by the following integral,

$$\left\langle \frac{1}{r^3} \right\rangle_r^{j_n} \equiv \int_0^{r_{\text{max}}} dr \frac{|R^{j_n}(r)|^2}{r}. \quad (\text{G.8})$$

Here, this integral is evaluated numerically for $r_{\text{max}} \geq a_0$, with a_0 the Bohr radius. The angular part of the wavefunction is not included in Eq. (G.8). The reason is that with this definition of p -like hyperfine coupling strength, both dipole-dipole

like coupling ($H_{\text{HF},2}$) and electron orbital momentum-nuclear spin coupling ($H_{\text{HF},3}$) have the same effective coupling strength on the atomic level since the radial part of both interactions are identical, and they only differ in their the angular parts. Moreover, the atomic wavefunctions can be presented as a product of an angular part and radial part. The angular part of Bi-based topological insulator states $\mathbb{Y}_{\text{Bi}(\text{Se})_p, \pm\frac{1}{2}}(\theta, \phi)$ can be written in the form of spherical harmonics $Y_l^m(\theta, \phi)$ and the spin-1/2 ($|\uparrow\rangle$ and $|\downarrow\rangle$) based on Eqs. (5.8)-(5.11),

$$\mathbb{Y}_{\text{Bi}_p, \frac{1}{2}}(\theta, \phi) = u_1 Y_1^1 |\downarrow\rangle + v_1 Y_1^0 |\uparrow\rangle, \quad (\text{G.9})$$

$$\mathbb{Y}_{\text{Se}_p, \frac{1}{2}}(\theta, \phi) = u_2 Y_1^1 |\downarrow\rangle + v_2 Y_1^0 |\uparrow\rangle, \quad (\text{G.10})$$

$$\mathbb{Y}_{\text{Bi}_p, -\frac{1}{2}}(\theta, \phi) = u_1 Y_1^{-1} |\uparrow\rangle + v_1 Y_1^0 |\downarrow\rangle, \quad (\text{G.11})$$

$$\mathbb{Y}_{\text{Se}_p, -\frac{1}{2}}(\theta, \phi) = u_2 Y_1^{-1} |\uparrow\rangle + v_2 Y_1^0 |\downarrow\rangle. \quad (\text{G.12})$$

These states are eigenstates of $J_z = L_z + S_z$ (with eigenvalue $\hbar m_j$), $\mathbf{J}^2 = (\mathbf{L} + \mathbf{S})^2$ (with $j = 3/2$), \mathbf{L}^2 (with $l = 1$ due to the p -like states), and \mathbf{S}^2 (with $s = 1/2$). We note that we follow the signs (phase) convention for $|3/2, \pm 1/2\rangle$ states to write the angular part of states mentioned above in terms of spherical harmonics [241].

Furthermore, we can also rewrite $h_{2,n}$ as a product of radial and angular parts,

$$\begin{aligned} h_{2,n} = & \frac{\mu_0}{4\pi} \gamma_e \gamma_{jn} \frac{1}{r^3} \left\{ \left(\frac{3z^2 - r^2}{2r^2} \right) \left[2S_z I_{z,n} - \frac{1}{2}(S_+ I_{-,n} + S_- I_{+,n}) \right] \right. \\ & + \frac{3}{2} \left(\frac{x^2 - y^2}{r^2} \right) \frac{1}{2}(S_+ I_{+,n} + S_- I_{-,n}) + \frac{3xy}{r^2} (S_x I_{y,n} + S_y I_{x,n}) \\ & \left. + \frac{3xz}{r^2} (S_x I_{z,n} + S_z I_{x,n}) + \frac{3yz}{r^2} (S_y I_{z,n} + S_z I_{y,n}) \right\}, \end{aligned} \quad (\text{G.13})$$

which is the same as Eq. (C3) in Lunde and Platero's paper [209]. Moreover, $A_{P,jn}^{\text{Atomic}}$ includes the radial part of states written in Eq. (G.8) and the other parameters, not the angular part. So, the terms in the curly bracket of Eq. (G.13) corresponds to the remained angular part.

To find the $\mathcal{H}_{\text{HF},3}$ interaction related to the p -like states in Bi-based topological insulator band model, the integrals in the spherical approximation again can be separated into the radial part (see Eq. (G.8)) and angular part (see Eq. (G.6)). To find this hyperfine interaction, we use Eqs. (G.9)-(G.12) and terms defined in (H.9)-(H.12) as well as rewriting $\mathbf{L}_n \cdot \mathbf{I}_n = L_{z,n} I_{z,n} + \frac{1}{2}(L_{+,n} I_{-,n} + L_{-,n} I_{+,n})$.

To calculate the matrix element of contact hyperfine interaction, we start with

$$\begin{aligned} \langle \varphi_{\mathbf{k},\text{Bi}(\text{Se})_s,\tau\frac{1}{2}} | H_{\text{HF},i} | \varphi_{\mathbf{k}',\text{Bi}(\text{Se})_s,\tau'\frac{1}{2}} \rangle &= \frac{v_a}{V} \sum_n \sum_{\mathcal{R}_n} e^{i(\mathbf{k}'-\mathbf{k})\cdot\mathcal{R}_n} \\ &\times \int_{v_{uc}} d\boldsymbol{\rho} \left[u_{\text{Bi}(\text{Se})_s,\tau\frac{1}{2}}(\boldsymbol{\rho}) \right]^* h_{i,n} u_{\text{Bi}(\text{Se})_s,\tau'\frac{1}{2}}(\boldsymbol{\rho}), \end{aligned} \quad (\text{G.14})$$

where only s -orbital contributions to the lattice periodic functions are considered. The $u_{\text{Bi}(\text{Se})_s,\pm\frac{1}{2}}(\mathbf{r})$ can be written as a multiplication of the orbital part and the spin part, $u_{\text{Bi}(\text{Se})_s,+(-)\frac{1}{2}}(\mathbf{r}) = u_{\text{Bi}(\text{Se})_s}(\mathbf{r}) |\uparrow (\downarrow)\rangle$. $\mathbf{S}\cdot\mathbf{I}_n = \frac{1}{2}(S_+I_{-,n} + S_-I_{+,n}) + S_zI_{z,n}$, therefore,

$$\begin{aligned} \langle \varphi_{\mathbf{k},\text{Bi}(\text{Se})_s,\tau\frac{1}{2}} | H_{\text{HF},i} | \varphi_{\mathbf{k}',\text{Bi}(\text{Se})_s,\tau'\frac{1}{2}} \rangle &= \sum_n \sum_{\mathcal{R}_n} \frac{e^{i(\mathbf{k}'-\mathbf{k})\cdot\mathcal{R}_n}}{V} \\ &\times A_{s,j_n} \frac{1}{\hbar} \left[\tau \frac{1}{2} I_{z,n} \delta_{\tau,\tau'} + \frac{1}{2} I_{\tau',n} \delta_{\tau,-\tau'} \right], \end{aligned} \quad (\text{G.15})$$

where $I_{\pm,n} \equiv I_{x,n} \pm iI_{y,n}$ are the ladder operators of nuclear spin. A_{s,j_n} is the contact hyperfine interaction coupling,

$$\begin{aligned} A_{s,j_n} &\equiv v_a (u_{\text{Bi}(\text{Se})_s}(\mathcal{R}_n))^* u_{\text{Bi}(\text{Se})_s}(\mathcal{R}_n) A_{s,j_n}^{\text{Atomic}} \\ &\simeq N_{\text{Bi}(\text{Se})_s}^* N_{\text{Bi}(\text{Se})_s} (\alpha_{\text{Bi}(\text{Se})_s}^{j_n})^* \alpha_{\text{Bi}(\text{Se})_s}^{j_n} (\Psi_{\text{Bi}(\text{Se})_s}^{j_n}(0))^* \Psi_{\text{Bi}(\text{Se})_s}^{j_n}(0), \end{aligned} \quad (\text{G.16})$$

where $A_{s,j_n}^{\text{Atomic}} \equiv \gamma_1$ for the nuclear spin at site n of isotope j , see Eq. (H.1) for definition of γ_1 .

APPENDIX H: Details on Hyperfine Interaction Coefficients

The prefactors in Eqs. (5.5)- (5.7) are defined as follows,

$$\gamma_1 = \frac{\mu_0}{4\pi} \frac{8\pi}{3} \gamma_e \gamma_{j_n}, \quad (\text{H.1})$$

$$\gamma_2 = \frac{\mu_0}{4\pi} \gamma_e \gamma_{j_n}. \quad (\text{H.2})$$

Here μ_0 is the vacuum permeability, $\gamma_e = g_e \mu_B / \hbar$ and $\gamma_{j_n} = g_{j_n} \mu_N / \hbar$ are the gyro-magnetic ratios of the electron and the n th nuclear spin of the isotope j , respectively, where g_{j_n} ($g_e \simeq 2$) is the nuclear (electron) g -factor, μ_N (μ_B) is the nuclear (Bohr) magneton.

Definitions of A_i terms and the p -like hyperfine couplings, A_{p,j_n} , used in Eq. (5.18), the $\tilde{H}_{\text{HF},2}$ interaction corresponding to the p -like states in the band model of Bi-based topological insulators, are as follows,

$$A_1 = u_1^2 + 2v_1^2 - 3\sqrt{2}(u_1 v_1), \quad (\text{H.3})$$

$$A_2 = u_1 u_2 + 2v_1 v_2 - \frac{3}{\sqrt{2}}(u_1 v_2 + u_2 v_1), \quad (\text{H.4})$$

$$A_3 = u_2^2 + 2v_2^2 - 3\sqrt{2}u_2 v_2, \quad (\text{H.5})$$

$$A_4 = -3u_1^2 - v_1^2 + \frac{3}{\sqrt{2}}u_1 v_1, \quad (\text{H.6})$$

$$A_5 = -3u_1 u_2 - v_1 v_2 + \frac{3}{2\sqrt{2}}(u_1 v_2 + u_2 v_1), \quad (\text{H.7})$$

$$A_6 = -3u_2^2 - v_2^2 + \frac{3}{\sqrt{2}}u_2 v_2, \quad (\text{H.8})$$

We consider that $u_{1(2)}$ and $v_{1(2)}$ are real numbers, see Appendix F.

The p -like hyperfine interaction couplings are defined as follows,

$$A_{p,j_n}^{++} \equiv v_a |N_{\text{Bi}_p}|^2 |\alpha_{\text{Bi}_p}^{j_n}|^2 A_{p,j_n}^{\text{Atomic}}, \quad (\text{H.9})$$

$$A_{p,j_n}^{--} \equiv v_a |N_{\text{Se}_p}|^2 |\alpha_{\text{Se}_p}^{j_n}|^2 A_{p,j_n}^{\text{Atomic}}, \quad (\text{H.10})$$

$$A_{p,j_n}^{+-} \equiv v_a N_{\text{Bi}_p}^* N_{\text{Se}_p} \text{sgn}(\alpha_{\text{Bi}_p}^{j_n}) \text{sgn}(\alpha_{\text{Se}_p}^{j_n}) (\alpha_{\text{Bi}_p}^{j_n})^* \alpha_{\text{Se}_p}^{j_n} A_{p,j_n}^{\text{Atomic}}, \quad (\text{H.11})$$

$$A_{p,j_n}^{-+} = (A_{p,j_n}^{+-})^*, \quad (\text{H.12})$$

where $N_{\text{Bi(Se)}_p}$ is the normalization constant for lattice periodic functions that are independent of the spin sign since the atomic wavefunctions for different spin signs are identical, see Eqs. (5.8)- (5.11). Here $\alpha_{\text{Bi(Se)}_p}^{j_n}$ describes the electron sharing of

the associated atom in the unit cell, and $\text{sgn}(\alpha_{\text{Bi}(\text{Se})_p}^{jn})$ corresponds to the signs of this term in the atomic wavefunctions, see Eqs. (G.1) and (G.2), stemming from the bonding and antibonding properties of the bands as well as the parity.

B_i terms corresponding to the Eq. (5.20) are defined as follows

$$\begin{aligned} B_1 &= u_1^2, & B_2 &= u_1 u_2, & B_3 &= u_2^2, & B_4 &= \sqrt{2} u_1 v_1, \\ B_5 &= \frac{1}{\sqrt{2}}(u_1 v_2 + u_2 v_1) & B_6 &= \sqrt{2} u_2 v_2. \end{aligned} \quad (\text{H.13})$$

The position dependent s -like hyperfine couplings, A_{s,j_n} , used in Eq. (5.24) are

$$A_{s,j_n}^{++} \equiv v_a |N_{\text{Bi}_s}|^2 |\alpha_{\text{Bi}_s}^{jn}|^2 |\Psi_{\text{Bi}_s}^{jn}(0)|^2 A_{s,j_n}^{\text{Atomic}}, \quad (\text{H.14})$$

$$A_{s,j_n}^{--} \equiv v_a |N_{\text{Se}_s}|^2 |\alpha_{\text{Se}_s}^{jn}|^2 |\Psi_{\text{Se}_s}^{jn}(0)|^2 A_{s,j_n}^{\text{Atomic}}, \quad (\text{H.15})$$

$$A_{s,j_n}^{+-} \equiv v_a N_{\text{Bi}_s}^* N_{\text{Se}_s} \text{sgn}(\alpha_{\text{Bi}_s}^{jn}) \text{sgn}(\alpha_{\text{Se}_s}^{jn}) (\alpha_{\text{Bi}_s}^{jn})^* \alpha_{\text{Se}_s}^{jn} (\Psi_{\text{Bi}_s}^{jn}(0))^* \Psi_{\text{Se}_s}^{jn}(\boldsymbol{\rho}) A_{s,j_n}^{\text{Atomic}}, \quad (\text{H.16})$$

$$A_{s,j_n}^{-+} = (A_{s,j_n}^{+-})^*. \quad (\text{H.17})$$

The position dependent hyperfine interaction for the Bi-based topological insulator slab are

$$A_{p(s),j_n}^{++}(\mathcal{X}_i) \equiv A_{p(s),j_n}^{++} |f_{\text{Bi}_{p(s)}}|^2, \quad (\text{H.18})$$

$$A_{p(s),j_n}^{--}(\mathcal{X}_i) \equiv A_{p(s),j_n}^{++} |f_{\text{Se}_{p(s)}}|^2, \quad (\text{H.19})$$

$$A_{p(s),j_n}^{+-}(\mathcal{X}_i) \equiv A_{p(s),j_n}^{+-} f_{\text{Bi}_{p(s)}}^* f_{\text{Se}_{p(s)}}, \quad (\text{H.20})$$

$$A_{p(s),j_n}^{-+}(\mathcal{X}_i) = (A_{p(s),j_n}^{+-}(\mathcal{X}_i))^*. \quad (\text{H.21})$$

The hyperfine interaction coupling regarding surface states are

$$\mathcal{A}_1^{++} = \frac{1}{2} A_{s,j_n}^{++} + \left(B_1 + \frac{A_1}{5} \right) A_{p,j_n}^{++}, \quad (\text{H.22})$$

$$\mathcal{A}_1^{+-} = \frac{1}{2} A_{s,j_n}^{+-} + \left(B_2 + \frac{A_2}{5} \right) A_{p,j_n}^{+-}, \quad (\text{H.23})$$

$$\mathcal{A}_1^{--} = \frac{1}{2} A_{s,j_n}^{--} + \left(B_3 + \frac{A_3}{5} \right) A_{p,j_n}^{--}, \quad (\text{H.24})$$

$$\mathcal{A}_2^{++} = \frac{1}{2} A_{s,j_n}^{++} + \left(B_4 + \frac{A_4}{5} \right) A_{p,j_n}^{++}, \quad (\text{H.25})$$

$$\mathcal{A}_2^{+-} = \frac{1}{2} A_{s,j_n}^{+-} + \left(B_5 + \frac{A_5}{5} \right) A_{p,j_n}^{+-}, \quad (\text{H.26})$$

$$\mathcal{A}_2^{--} = \frac{1}{2} A_{s,j_n}^{--} + \left(B_6 + \frac{A_6}{5} \right) A_{p,j_n}^{--}. \quad (\text{H.27})$$